Aalto University

OPEN ACCESS

This is an electronic reprint of the original article.
This reprint may differ from the original in pagination and typographic detail.

Appiah, Eugene Sefa; Dzikunu, Perseverance; Akinwamide, Samuel Olukayode; Fangnon, Eric A.K.; Mensah-Darkwa, Kwadwo; Andrews, Anthony; Agyemang, Frank Ofori; Nartey, Martinson Addo; Makgopa, Katlego; Bossuyt, Sven

# A review on progress and prospects of diatomaceous earth as a bio-template material for electrochemical energy storage : synthesis, characterization, and applications

*Published in:*
Ionics

*DOI:*
10.1007/s11581-024-05825-6

Published: 01/12/2024

*Document Version*
Publisher's PDF, also known as Version of record

*Published under the following license:*
CC BY

*Please cite the original version:*
Appiah, E. S., Dzikunu, P., Akinwamide, S. O., Fangnon, E. A. K., Mensah-Darkwa, K., Andrews, A., Agyemang, F. O., Nartey, M. A., Makgopa, K., & Bossuyt, S. (2024). A review on progress and prospects of diatomaceous earth as a bio-template material for electrochemical energy storage : synthesis, characterization, and applications. *Ionics*, *30*(12), 7809-7860. Article 100885. https://doi.org/10.1007/s11581-024-05825-6

This material is protected by copyright and other intellectual property rights, and duplication or sale of all or part of any of the repository collections is not permitted, except that material may be duplicated by you for your research use or educational purposes in electronic or print form. You must obtain permission for any other use. Electronic or print copies may not be offered, whether for sale or otherwise to anyone who is not an authorised user.

Ionics (2024) 30:7809–7860
https://doi.org/10.1007/s11581-024-05825-6

REVIEW

# A review on progress and prospects of diatomaceous earth as a bio-template material for electrochemical energy storage: synthesis, characterization, and applications

**Eugene Sefa Appiah**[1,2,6] · **Perseverance Dzikunu**[1,2] · **Samuel Olukayode Akinwamide**[2,3] · **Eric A. K. Fangnon**[2] · **Kwadwo Mensah-Darkwa**[1,4] · **Anthony Andrews**[1] · **Frank Ofori Agyemang**[1] · **Martinson Addo Nartey**[1] · **Katlego Makgopa**[5] · **Sven Bossuyt**[2]

Received: 10 July 2024 / Revised: 26 August 2024 / Accepted: 8 September 2024 / Published online: 22 October 2024
© The Author(s) 2024

## Abstract

This comprehensive review explores the remarkable progress and prospects of diatomaceous earth (DE) as a bio-template material for synthesizing electrode materials tailored explicitly for supercapacitor and battery applications. The unique structures within DE, including its mesoporous nature and high surface area, have positioned it as a pivotal material in energy storage. The mesoporous framework of DE, often defined by pores with diameters between 2 and 50 nm, provides a substantial surface area, a fundamental element for charge storage, and transfer in electrochemical energy conversion and storage. Its bio-templating capabilities have ushered in the creation of highly efficient electrode materials. Moreover, the role of DE in enhancing ion accessibility has made it an excellent choice for high-power applications. As we gaze toward the future, the prospects of DE as a bio-template material for supercapacitor and battery electrode material appear exceptionally promising. Customized material synthesis, scalability challenges, multidisciplinary collaborations, and sustainable initiatives are emerging as key areas of interest. The natural abundance and eco-friendly attributes of DE align with the growing emphasis on sustainability in energy solutions, and its contribution to electrode material synthesis for supercapacitors and batteries presents an exciting avenue to evolve energy storage technologies. Its intricate structures and bio-templating capabilities offer a compelling path for advancing sustainable, high-performance energy storage solutions, marking a significant step toward a greener and more efficient future.

**Keywords** Diatomaceous earth · Frustules · Bio-templated synthesis · Electrode materials · Electrochemical energy storage devices

## Introduction

Energy storage devices, such as supercapacitors and batteries, are promising for efficient energy storage, but their performance largely depends on the synthesized electrode materials [1–3]. Recently, there has been growing interest in materials with high and ordered porosity. These materials offer increased surface area for enhanced ion adsorption, improved electrolyte access, and better electrical conductivity. Additionally, they help address issues such as electrode degradation, thereby improving overall stability [4–6]. By tailoring the porosity, researchers can optimize ion diffusion and enable compatibility with various electrolytes. Ultimately, electrode materials with high and ordered nanoscale porosity play a critical role in boosting the energy storage performance of various applications [7–9].

In materials science, novel ideas often arise from studying and drawing inspiration from nature's remarkable designs [1, 10]. Structured patterns and surfaces are integral to many fields, including material science, chemistry, microelectronics, energy storage [11–14], optics [15–18], photonics [19, 20], catalysis [21–23], biosensing [21, 24–26], drug delivery [27–29], filtration [30, 31], bioencapsulation, and immunoisolation. A key innovation in this area is the use of bio-templated electrode materials, particularly those made from diatomaceous earth (DE). DE is composed of the fossilized remains of diatoms, single-celled algae that lived millions of years ago.

---

Extended author information available on the last page of the article

Diatoms display extraordinary precision and complexity in their amorphous silica exoskeletons, known as frustules [32, 33]. These frustules exhibit unique shapes and intricate features such as pores, ridges, spikes, and spines, highlighting their diverse and intricate nature [34]. The structure of DE bio-templated electrode materials consists of fundamental components such as diatom frustules and fossilized remains, including epitheca, hypotheca, valves, and girdle bands [32, 34–37]. The defining feature of DE is its high porosity, characterized by rows of interstriae and ribs, which create a porous network. DE was discovered by Peter Kasten, a German peasant, in the early nineteenth century and has since evolved from a simple natural substance to a material of immense scientific interest [38, 39]. DE forms through the gradual accumulation of silica-rich diatom cell walls on the ocean floor as diatoms complete their natural life cycle. This geological process has led to the widespread distribution of DE in marine and freshwater environments around the world [35]. DE's unique properties make it highly valuable and versatile [40]. It features high porosity, low thermal conductivity, small particle size, a large surface area, chemical inertness, and a lightweight nature. The primary component of DE is silicon dioxide ($SiO_2$, 86 wt%), with minor components such as aluminum oxide ($Al_2O_3$, 5.5 wt%), magnesium oxide (MgO, 0.78 wt%), calcium oxide (CaO, 2.1 wt%), iron oxide ($Fe_2O_3$, 2.5 wt%), potassium oxide ($K_2O$, 1.39 wt%), and sodium oxide ($Na_2O$, 0.22 wt%) [35, 39, 41]. Initially used in pottery, brickmaking, and agriculture, DE is now recognized for its high porosity, lightweight, and chemical stability, which make it suitable for advanced technological applications [36, 42].

One of the most promising applications of DE is in electrochemical energy storage systems such as supercapacitors and batteries. The unique structure of diatom frustules provides an excellent template for creating electrode materials. The high porosity of DE enables greater material deposition within the structure, increasing the loading of active materials, which is essential for improving electrode performance. This porous network also enhances ion movement, crucial for efficient energy storage[43–45]. The natural intricacy of DE's frustules simplifies the creation of nanomaterials with well-organized structures, resulting in superior performance in energy storage devices. DE bio-templated materials serve as natural scaffolds, facilitating the precise growth and arrangement of nanomaterials. Conductive materials can be incorporated into the DE structure to enhance electrical conductivity. When used as a soft template, the DE is often etched away, leaving the active material with the morphology of the diatomite template, which is vital for fast charge and discharge rates in supercapacitors and batteries. Additionally, using DE can reduce the complexity and cost of manufacturing processes typically required for advanced materials. This makes DE an attractive option for producing high-performance electrochemical energy storage device electrode materials more efficiently [35, 42, 46].

DE's sustainability and biocompatibility add to its appeal. DE is a naturally occurring material that aligns with eco-friendly and sustainable practices. DE is environmentally benign unlike many synthetic materials, making it ideal for green energy solutions [35]. Its biocompatibility also opens doors for its use in medical devices and environmental sensors, where interaction with living organisms is necessary. The history of diatomaceous earth, from its discovery and early uses to its modern applications, highlights its versatility. Once employed in agriculture and industry, DE has now become a valuable material in cutting-edge materials science [38, 42]. Its complex structure and high porosity make it an excellent foundation for advanced electrode materials in energy storage systems. By leveraging DE's natural properties, researchers explore its potential as a bio-template material for producing eco-friendly and easily fabricated electrodes for supercapacitors and batteries. This simplifies production processes and reduces the need for complex systems such as chemical vapor deposition [47] and physical vapor deposition, minimizing the use of hazardous materials and dangerous work environments. Several studies have explored DE as a bio-template material for synthesizing electrodes in electrochemical energy storage. These studies, shown in Fig. 1, indicate a steady increase in research interest over the years.

As materials science continues to manipulate structures at the nano [48] and micro levels [49] for specific functionalities, DE has emerged as an exceptional bio-template material. It provides a unique way to replicate and harness nature's intricate designs. DE serves as both a template and precursor for materials with finely tuned nanostructures, a characteristic that has garnered increasing attention in contemporary scientific and industrial contexts [35, 50–52]. In an era driven by the pursuit of sustainable technologies and materials [50, 53–55], DE's eco-friendly [40, 44] attributes make it an excellent candidate for innovation. Its use as a bio-template material for electrode synthesis holds significant promise for advancing both technological innovation and environmental stewardship. This research article explores the potential of DE as a bio-template material for electrode material synthesis, delving into the intricate processes, recent advancements, and unexplored frontiers in this emerging field [35]. By understanding its historical roots and the contemporary drive for sustainable innovation, we navigate the exciting landscape of diatomaceous earth's transformation from a natural marvel to a bio-templated material of significant scientific and technological importance.

## Synthesis routes of diatomaceous earth bio-templated electrode material for energy storage applications

Before implementing energy-storage systems [55–58], it is imperative to subject natural mineral compounds to pretreatment to enhance their electrochemical properties [59]. In mineral engineering, traditional methodologies encompass a range of processes, such as purification [37], particle control [60], and thermal treatment [35, 61], all aimed at enhancing the stability [62] and conductivities of minerals [39, 41, 50]. Addressing inherent impurities in mineral samples is crucial, as these impurities may compromise electrochemical properties [35]. Modern purification procedures encompass a range of techniques, incorporating physical methods such as magnetic, electric, gravitational, and flotation separations alongside chemical methodologies, with a predominant focus on wetting purification [63–65]. These approaches collectively attain high levels of purity, reaching up to 99.5%. However, relatively large particles in minerals necessitates specific particle-controlling processes tailored to different dimensional structures [66]. For instance, the 1D structure requires a releasing process to enhance dispersion, while the 2D structure involves grinding, stripping, and dissociation technologies to separate layer materials [37]. In the case of 3D bulk structures, ultra-grinding reduces particle size to below 10 μm [67]. These treatments primarily address the physical properties of minerals, ensuring uniformity and stability. Subsequent chemical processes focus on enhancing electron conductivity through high-temperature thermal treatments to remove crystal water and improve crystallinity [37, 50, 52]. This multi-step approach makes natural mineral compounds more suitable for energy storage systems (ESSs), with numerous compounds exhibiting improved electrochemical properties [40, 68]. In the context of ESSs, cell systems comprise electrodes, separators, and electrolytes [63, 69, 70]. Electrode materials demand rich redox potentials and electrochemical activity, necessitating specific minerals [12, 71]. Notably, Si-based and O/S-based materials show promise and phase transformation methods with conductive matrices enhance ion-storage capabilities [35, 44, 50, 52]. Studying silicate minerals includes examining separators and electrolytes, crucial for porosity, surface area, and surface charge determination. Silicate minerals with Si–O complex anions offer effective ion diffusion paths [44, 72]. Within these minerals, the Si–O, Al-O, and Mg-O bands act as active sites for capturing polysulfides in supercapacitors and Li–S or Li-ion systems [51, 73]. Transitioning to making bio-templated electrode materials from diatomaceous earth for energy storage, we use the natural features of this sedimentary rock [50, 74]. DE is inherently porous and comprised of fossilized diatom remains, serving as a unique template [35]. The synthesis involves extracting diatomaceous earth, isolating, and purifying diatom frustules, and modifying them through chemical treatments, functionalization, and doping or using it as template material to enhance the electrochemical attributes of the electrode material.

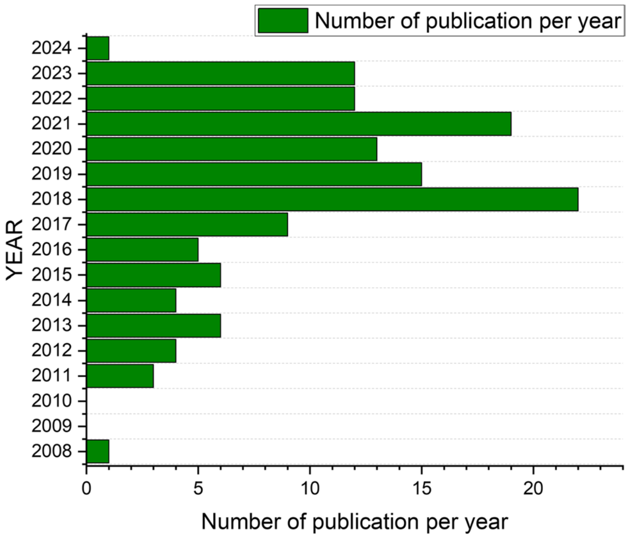

**Fig. 1** Visual representation of research articles published on the synthesis of electrode materials via the diatomaceous earth bio-templated approach for electrochemical energy storage from 2008 to 2024 (Sourced from the Scopus database; search date: January 2, 2024)

### Template-assisted synthesis

Different methods, including chemical, physio-chemical, and engineering-related techniques, can be used to create structured porous materials [16, 55, 75]. These synthesis routes are categorized into two broad classes: template-assisted and template-free. Template-assisted techniques involve using a template as a scaffold to guide the formation of the material's pore structure. The template directs the architecture and size of the pores, and examples of such techniques include electrodeposition, where a conductive template, such as a nanoporous membrane, is used as a scaffold, and the material is deposited electrochemically. This method is commonly employed to create metal and oxide materials with well-defined pore structures. Another example is chemical vapor deposition (CVD), which uses gaseous precursors to deposit thin layers of material onto a template. Although CVD is primarily a thin-film deposition method, it can be used with templates to create porous structures. Once the desired material is deposited, the template may be removed or retained, depending on the final product. Similarly, atomic layer deposition (ALD) is another highly precise technique that deposits material at the atomic level, enabling the production of highly ordered porous structures, such as nanoporous alumina or titanium oxide, when combined with templating scaffolds.

On the other hand, template removal techniques, a subset of template-assisted methods, involve synthesizing the porous material around a template that is later removed to create the pore network. These techniques can be further classified into soft templating and hard templating approaches. Flexible organic molecules like surfactants, block copolymers, or micelles are used as templates in soft templating. These molecules self-assemble into specific structures, and the material is synthesized around them. Afterwards, heat or chemical treatment removes the soft template, leaving behind mesoporous or microporous structures. For instance, surfactants are used as templates in sol–gel processes to create mesoporous silica. In hard templating, rigid solid materials such as silica nanoparticles, carbon spheres, or metal oxides are used as templates. After the material forms around the hard template, it is removed via etching or dissolution, resulting in a well-defined porous network. An example is the synthesis of mesoporous carbons, where silica is used as a hard template and subsequently etched away with hydrofluoric acid (HF) or sodium hydroxide (NaOH). Template-free methods, by contrast, rely on spontaneous self-assembly processes such as phase separation or micro-emulsion polymerization to form porous structures without the use of external templates. While simpler, template-free approaches offer less control, often resulting in unpredictable pore sizes and morphologies. For example, phase separation during solvent evaporation can lead to the formation of porous materials, but the pore architecture is typically less precise than that achieved with templated methods.

Templating techniques [68, 76] are particularly favored in synthesizing hierarchically porous materials, where multiple levels of porosity (e.g., micro, meso, and macropores) are required for specific applications such as catalysis, separations, and energy storage. Researchers can carefully tune the porosity at various scales to enhance functionality by using multiple templates or combining templating strategies. However, producing templated materials, particularly those with hierarchical porosity, often involves complex post-synthesis processes. The removal of templates can require significant resources, including chemicals for etching or dissolution and energy for processes like calcination, which are essential to ensure that no residual template material remains that could compromise the final structure's properties [77]. While template-free methods provide a simpler synthesis route, they often lack the precision control available with templated approaches. Because template-free synthesis relies on spontaneous formation and self-assembly, it is more challenging to predict the resulting pore sizes and shapes [33]. This section further explores the creation of porous materials with different structures, emphasizing soft templating [78], hard templating [79], and other template-related methods [1] as a sub-grouping of template-assisted synthesis based on the templating material, as illustrated in Fig. 2.

Soft templates are molecular systems with flexible structures and limited function within a specific space [78]. This part presents three main soft templating techniques: surfactant, breath figure, and emulsion templating [10]. This method utilizes multi-molecular aggregates, such as micelles and liquid crystals, as structure-directing agents assembled by surfactant molecules [80, 81]. Mixing various surfactants can create materials with two types of pores or three different porous structures [81]. The surfactant templating method offers manageable pore size and variable pore shape, making it useful for synthesizing several materials, including metals, silicon dioxides, and metal oxides [19, 79, 82]. This technique relies on emulsion properties to create materials with good porosity through the solidification or polymerization of the emulsion in a continuous phase. Despite its simplicity, a basic preparation method faces challenges like maintaining emulsion stability and dealing with the effects of template removal approach on material structure [77, 83, 84]. Different emulsion systems, including water-in-oil, oil-in-water, and supercritical $CO_2$ emulsion, can be tailored to prepare hierarchically ordered porous materials [1, 10]. This technique relies on the breath figure phenomenon, where water vapor condenses on cold surfaces to create hexagonally arranged water droplets. These droplets act as templates, and the process is straightforward, making them efficient for creating large two-dimensional porous structures [68, 85]. The breath figure templating method allows the synthesis of honeycomb-like controlled porous layers with variable pore dimensions using various organic and inorganic materials [86]. Hard templates have rigid structures that guide material growth by limiting space [10]. This section discusses three main hard templating technologies: colloidal crystal templating, polymer templating, and bio-templating [54, 87]. This method utilizes colloidal crystals with a 3D-ordered opal structure as templates, allowing for the preparation of hierarchically controlled permeable materials with well-ordered pores. The size of the pores can be adjusted by modifying the sizes of the microspheres in the templates [1, 77, 79, 88]. Hierarchically structured porous materials with long-range ordered structures find applications in optical signal processors [15, 18], electrochemical energy storage [33, 89], and more. The bio-templating approach employs natural biomass as template to obtain permeable materials with detailed structures. Natural biological structures, evolved over billions of years, provide an ideal stage for arranging complex hierarchically ordered porous materials [72, 88, 90, 91]. For instance, diatoms can be used as direct hard bio-templates for synthesizing meso/macroporous hierarchical porous silica [50, 74, 92]. Porous polymeric materials, such

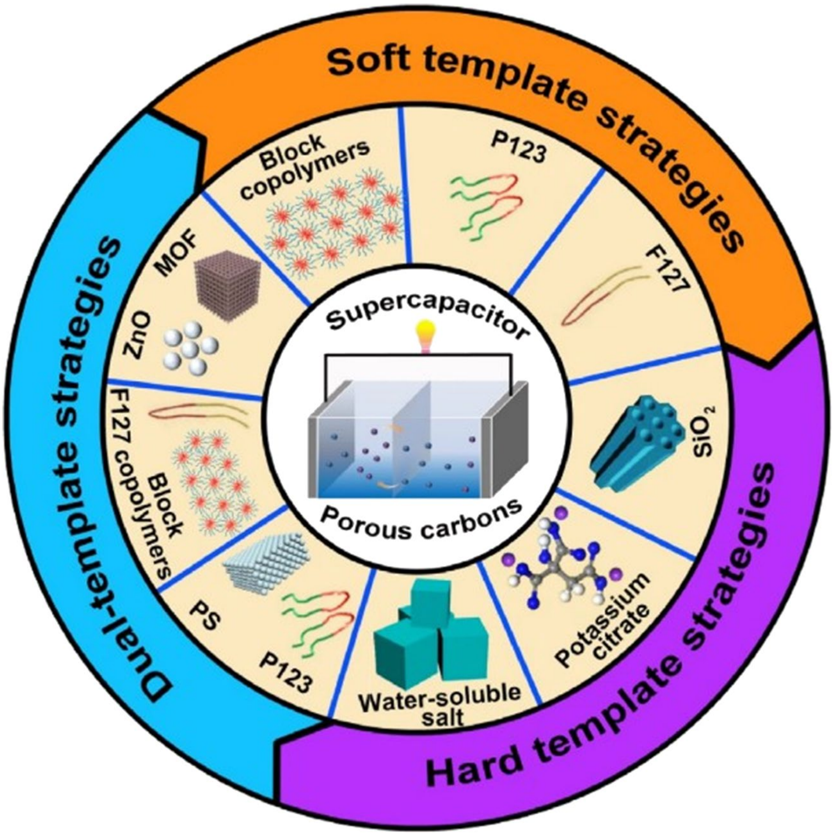

**Fig. 2** Diagram outlining the creation of porous carbons for high-performance supercapacitors. Source: [10]

as polymer foams, gels, and fibers, can be used as templates to make hierarchically ordered porous materials [67, 93–95]. These porous polymers offer advantages like various preparation methods, variable pore dimensions, and manageable surface adjustment [93]. The polymer templating method involves injecting precursor solutions into porous polymer gels [96, 97], forming composite materials that, upon removing the polymer template, result in porous silica with retained structural properties [66, 67, 72]. In conclusion, by tailoring these templating methods [1], specifically incorporating diatomite as a template material [50, 52, 74], it is possible to accomplish hierarchically ordered porous materials with required features for varied applications, including the storage of energy [72, 98], catalysis, sensors [41, 66], and biomedicine [24, 99].

Cai et al. [100] employed diatoms as direct hard bio-templates to synthesize meso/macroporous hierarchical silica. In the preparation procedure, infiltration and coating techniques were employed to replicate the entire hierarchy of biological materials fully. The subsequent hierarchically ordered porous materials, formed through a bio-templating method, typically exhibit numerous surface functional molecules and easily manageable pore features. These functional materials hold promising applications in the realm of energy.

Similarly, Gou et al. [101]. presented an innovative and simple approach to creating an intricate three-dimensional (3D) composite for supercapacitors. The composite, denoted as diatomite@$TiO_2$@$MnO_2$, is constructed by integrating hollow diatom silica features with interrelated layers of $TiO_2$ nanospheres and $MnO_2$ mesoporous nanosheets. The coating process comprises the hydrolysis and metathetic reaction of a $TiF_4$ precursor, succeeded by a reaction with $KMnO_4$. This procedure confirms the complete coating of the external and internal surfaces of the diatom hollow structure with $TiO_2$ and $MnO_2$ sheets, as depicted in Fig. 3. The study reveals that the combination of anatase $TiO_2$ coating on the 3-D diatomite@$TiO_2$@$MnO_2$ electrodes significantly enhances rate capability, resistance, and specific capacitance. This underlines the vital role of an extra conductive layer on the diatom surface.

Furthermore, owing to its distinctive 3D structure, the diatomite@$TiO_2$@$MnO_2$ electrode exhibits prolonged cyclic stability of 94.1% capacitance retention after completing 2000 cycles and high coulombic efficiency of 98.2–99.6% capacitance retention all through the 2000 cycles. These results showcase the improved supercapacitor behavior of diatomite@$TiO_2$@$MnO_2$ electrodes, prepared using cost-effective natural diatomite material and a simple, scalable process. The results affirm their obvious potential for energy conversion and storage applications.

Also, Karaman et al. [33] utilized the distinct porous architecture and high surface area of cultured diatom (CD) frustules as a template for electrodes. A hydrolysis and metathesis reaction of $FeCl_3$ enabled the uniform iron oxide (FeOx) coating onto the CD, resulting in CD-$FeO_x$. The CD's relatively large surface area contributed to double-layer capacitance, while the $FeO_x$ introduced pseudocapacitance. The research revealed that a 51% loading of $FeO_x$ on CD significantly improved performance, achieving 70.2 F/g, a substantial increase compared to CD only. The supercapacitors maintained functionality after 1000 cycles, retaining 90% of their original performance. Additionally, the CD-$FeO_x$ composite proved effective in producing flexible supercapacitor electrodes.

## Synthesis methods

In the pursuit of optimizing electrode performance using diatomaceous earth as a bio-template material, researchers utilize various synthesis methods, including the sol–gel method [19], chemical vapor deposition (CVD) [72, 102], electrodeposition [103], and hydrothermal synthesis [51] as presented in Fig. 4. The bio-templating process yields three-dimensional structures [28, 67] with nanoscale characteristics [80, 104, 105], resulting in electrodes with a substantial surface area [106, 107], enhanced conductivity [108, 109], and improved electrochemical reactivity crucial attributes for energy storage applications [1, 110]. This bio-inspired method follows sustainability principles for designing eco-friendly materials, showing great potential for advanced and environmentally friendly energy storage devices in the evolving energy storage field [82, 110, 111].

### Sol–gel method

The synthesis of aerogels [112] is primarily accomplished through the sol–gel method [100]. This involves polymerization reactions leading to the formation of gels [113], which are subsequently dried to produce highly porous and lightweight materials [16]. The sol–gel process occurs at low temperatures (typically below 100 °C) in a liquid state [19], resulting in solid products through polymerization reactions involving metal atoms in the raw materials. The synthesis of aerogels using this process comprises two stages: forming separate colloidal solid particles with nanometer dimensions, followed by joining colloidal particles in the solvent to form a gel [16]. The chemistry of the sol–gel process is influenced by parameters such as the metal alkoxide activity, water/alkoxide ratio, solution pH, temperature, nature of the solvent, and additives [65]. Catalysts are often added to control the rate and extent of hydrolysis and condensation reactions [80, 96]. Varying these parameters allows the creation of materials with diverse microstructures and surface chemistry [86, 114]. The precursors for sol–gel processing, serving as starting materials, must be soluble in the reaction media and reactive enough to participate in the gel-forming process [16, 115]. Common precursors include salts, oxides, hydroxides, complexes, alkoxides, acrylates, and amines [16, 116, 117]. Silicon alkoxides like tetraethyl orthosilicate (TEOS) and tetramethyl orthosilicate (TMOS), along with water-soluble precursors like $Na_2SiO_3$, are frequently used, offering flexibility in tailoring the material properties [52, 118]. The wet gel can be converted to aerogels through drying methods, including supercritical drying and various other techniques [100, 114]. Supercritical drying involves

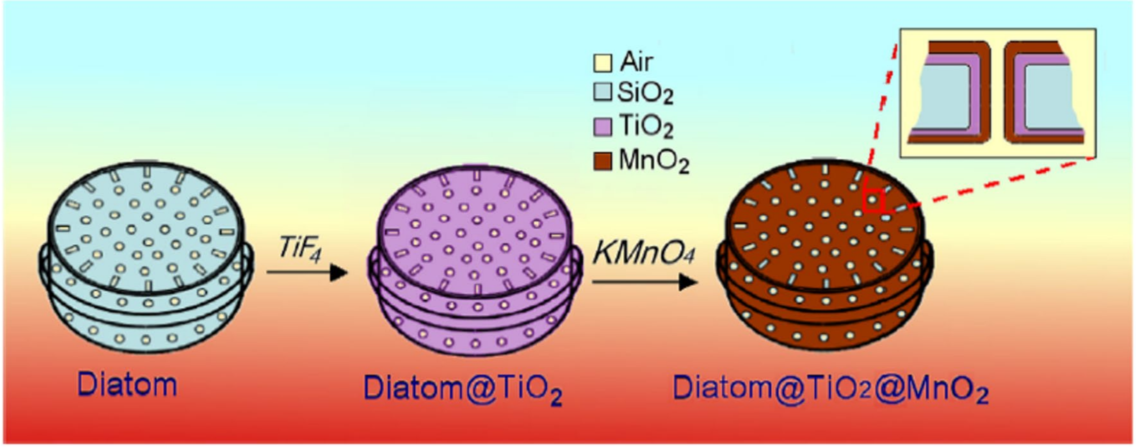

**Fig. 3** Illustration depicting the synthesis process of diatom@$TiO_2$ and diatom@$TiO_2$@$MnO_2$ 3-D composite supercapacitors, utilizing the morphology of diatoms. A cross-section displays the coating of both internal and external diatom surfaces with $TiO_2$ and $MnO_2$ nanocomposites. Source: [101]

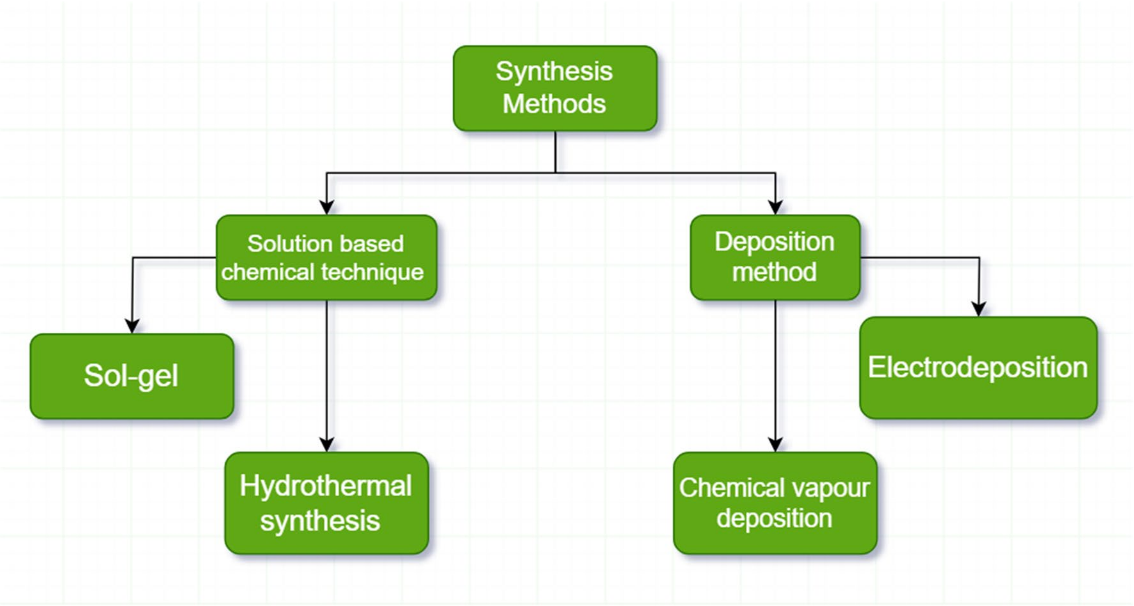

**Fig. 4** Flowchart illustrating different synthesis methods for synthesizing electrode materials using diatomite as a template or precursor for electrochemical energy storage applications

controlled heating in a closed space with controlled pressure to remove the solvent as gas, preserving the aerogel's porous structure [16]. Other drying methods include chemical additives, ambient pressure drying, and freeze-drying. Aerogels are classified into inorganic (e.g., silica, alumina), organic (e.g., resorcinol–formaldehyde), carbon, and hybrid aerogels [119]. Inorganic aerogels are often fragile due to their ceramic nature, while hybrid aerogels, synthesized by introducing organic-mineral compounds, exhibit lower fragility [120, 121]. The sol–gel method steps include achieving a homogeneous solution of precursors and alcohols, forming a sol through hydrolysis reactions, and converting the sol into a wet gel through condensation reactions [86]. The wet gel, a giant molecule with many pores, can be stimulated to form by using a suitable reagent [122]. The gel formation is controlled by condensation reactions, resulting in an oxide network containing metal oxide clusters [86]. The final step involves separating the solvent to obtain a dry gel, with the properties of the produced gels depending on the solvent and drying method used [117], as shown in Fig. 5.

Nassif et al. [19] described diatoms as a source of inspiration for advanced nanostructured biohybrids. Utilizing the sol–gel process, silica-based biohybrids are created, encapsulating biomolecules for applications in biosensors and bioreactors. These biohybrids, maintaining cell viability and metabolic activity, offer promising avenues in biotechnology and nanomedicine. The intricate shapes of diatom frustules enable the production of 3D hierarchically structured materials, such as sensors and photonic devices, while also serving as a model for bio-templated synthesis. Diatom nanotechnology represents a collaborative frontier between biologists and materials scientists, driving innovative research.

Lamastra et al. [116] conducted a low-temperature sol–gel synthesis to grow ZnO nanoparticles on the porous surface of diatomite (DE). The process started by mixing zinc acetate dihydrate with water/ethyl alcohol and triethanolamine. Subsequently, the microstructural features of the hybrid powders were explored using field emission scanning electron microscopy. Lamastra et al. [116] extensively examined the methodology for extracting absorption and scattering coefficients from hybrid powders. Their finding highlighted a focus on the 300–450-nm range of the scattering coefficient, demonstrating its utility in deriving insights into the size distribution of ZnO nanospheres. X-ray diffraction analysis (XRD) measurements confirmed the crystalline nature of ZnO nanoparticles even without calcination. SEM analysis with a field emission scanning electron microscope revealed a particle size range of 80 to 180 nm. ZnO nanoparticles showed a uniform distribution on frustules' surfaces and within pores. Additionally, most frustules had pores sized between 110 nm and 1.2 µm.

## Chemical vapor deposition (CVD)

Chemical vapor deposition (CVD) is a robust technology that makes high-quality thin films and coatings. It keeps improving when working with new materials [47]. CVD synthesis is advancing, creating accurate inorganic thin films for two-dimensional materials and depositing high-purity

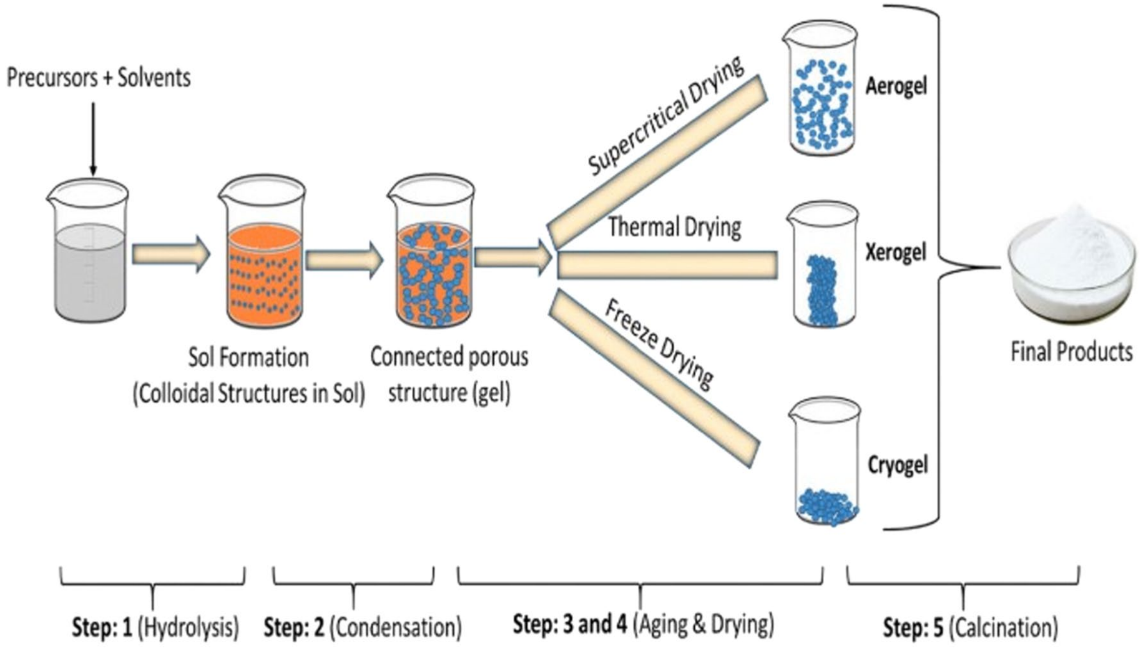

**Fig. 5** Outline of ZnO nanoparticle (NP) synthesis using sol–gel method. Source: [123]

polymer-based thin films on various substrates [124]. This primer provides a comprehensive insight into the CVD technique applied to synthesize hierarchically porous carbon materials [47]. It covers process control, material characterization, and considerations for reproducibility [125]. The text further explains the best ways to conduct experiments using materials such as graphene, 2D transition metal dichalcogenides (TMDs), and thin polymeric films. This includes preparing the substrate, growing at high temperatures, and handling post-growth processes [126]. The researcher also addresses recent advances and challenges in scaling the process [127]. Probing current limitations and improvements gives us ideas for future directions, such as designing reactors for efficiently growing thin films and nano-porous materials at low temperatures [47].

Wang et al. [125] synthesized carbon nanotubes (CNTs) for wastewater treatment by growing them on a Ni catalyst-diatomite surface using a chemical vapor deposition (CVD) technique. The study investigated how the carbon yield and microstructure of CNTs are affected by carefully adjusting synthesis conditions such as time and temperature. In addition to their wastewater treatment potential, the synthesized materials underwent two purification methods, namely, annealing and acid treatment, effectively augmenting their specific surface area. Remarkably, the diatomite-CNT composite adsorbents exhibited rapid equilibrium in adsorption experiments, with kinetics adhering to the pseudo-second-order model and the isotherm fitting well with the Langmuir model. Thermodynamic parameters indicated an exothermic and spontaneous adsorption process. In a broader context, beyond their application in wastewater treatment, the materials synthesized through this innovative approach hold promise for diverse uses, particularly in energy storage. The adaptability of these materials suggests potential applications in emerging fields, showcasing the multifaceted benefits of this synthesis methodology.

Nazhipkyzy et al. [128] investigated the synthesis of multi-walled carbon nanotubes (MWCNTs) on diatomite mineral impregnated with transition metal salts. They used a propane-butane mixture in a chemical vapor deposition reactor at atmospheric pressure. The study explored how catalyst concentration and synthesis temperature influenced the formation and morphology of MWCNTs. Diatomite, chosen for its rich elemental composition, including amorphous silica, quartz, and various metals, emerged as a promising material for catalytic chemical vapor deposition (C-CVD) synthesis of carbon nanotubes (CNTs). Catalysts like $CoCl_2 \cdot 6H_2O$ and $Ni\text{-}(NO_3)_2 \cdot 6H_2O$, at concentrations of 0.5, 1.0, and 1.5 M, played a crucial role in determining the characteristics of the synthesized MWCNTs on diatomite. Characterization of natural diatomite through XRD and SEM provided insights into its structural and morphological properties. Besides material science applications, the study highlighted the potential of diatomite-supported MWCNTs in energy storage, particularly in capacitive energy storage or other emerging technologies, showcasing the versatility and significance of this synthesis approach.

Also, Li et al. [129] conducted pioneering research on using transition metal-layered-double hydroxides in supercapacitors, a field of great scientific interest. The study overcame severe aggregation and low intrinsic conductivity using a two-step hydrothermal method and chemical vapor deposition. This process synthesized nickel–iron sulfide nanosheets ($NiFeS_x$) and CNTs on diatomite, utilizing the synergistic effects of multiple materials to boost electrochemical performance. Diatomite was chosen as a substrate for its ability to provide a favorable environment for the even dispersion of nanomaterials on its surface, thereby increasing active sites in contact with electrolytes. The $NiFeS_x$@CNTs@MnS@Diatomite electrode showed excellent electrochemical properties, with a high capacitance of 552 F/g at 1 A/g, 68.4% retention at 10 A/g, and 89.8% capacitance retention after 5000 cycles at 5 A/g. Combining it with graphene in an asymmetric supercapacitor resulted in a maximum energy density of 28.9 Wh/kg and a maximum power density of 9375 W/kg at 1.5 V. This study lays the groundwork for effective material preparation and design strategies for diatomite-based supercapacitors.

However, Li et al. [110] fabricated nitrogen-doped hierarchical graphene (NHG) materials through direct chemical vapor deposition (CVD) on natural diatomite templates. Biotemplating in this process helps make batches efficiently and precisely control doping concentration, improving material performance and extending lifespan. The research demonstrates that employing bio-templates in fabricating electrodes for lithium-sulfur batteries (Li–S) can significantly enhance their performance. This enhancement is achieved by leveraging the inherent structure and morphology of biological species. The use of bio-templates allows for the replication of biological features and offers control over the structure, functionality, and composition of Li–S electrodes, thereby contributing to the development of more sustainable LIBs. As highlighted in the review of [68], ongoing scientific efforts involve exploring additional biological materials to optimize LIB performance further.

## Electrodeposition

The facile synthesis of diverse morphological materials is achieved through a meticulous choice of deposition methods (non-toxic) and solution pH [103]. Electrodeposition [130] typically serves as the preferred technique for synthesizing various materials such as conducting polymers (CP), metal–organic frameworks (MTMO), and mesoporous asymmetric supercapacitor electrodes like polyaniline (PANI) [127]. The synthesis process involves co-electrodepositing nanoparticles from a precursor solution and their subsequent decomposition under specific thermal conditions [103].

## Hydrothermal synthesis

Hydrothermal synthesis stands out as a widely employed technique for crafting nanomaterials, relying on solution-based reactions [58]. This method facilitates nanomaterial formation across a broad temperature spectrum, ranging from room temperature to exceptionally high temperatures [131], as shown in Fig. 6. The control of material morphology during hydrothermal synthesis is achieved by employing either low-pressure or high-pressure conditions, contingent on the vapor pressure of the primary composition involved [132]. The versatility of this approach is evident in the successful synthesis of various nanomaterial types [51]. Hydrothermal synthesis boasts significant advantages over alternative methods [133]. Particularly noteworthy is its capability to generate nanomaterials that might not remain stable under elevated temperatures [58]. Moreover, the hydrothermal method enables the production of nanomaterials with high vapor pressures while minimizing material loss [134–136]. The composition of the synthesized nanomaterials can be precisely controlled through liquid-phase or multiphase chemical reactions within the hydrothermal synthesis process [137].

Using hydrothermal and calcination methods, a new material was created by combining a newly developed diatomite sieve with synthetically engineered sea-urchin-like iron trioxide. According to a recent study by Zhang et al. [139], the composite material $\alpha$-$Fe_2O_3$@D shows outstanding electromagnetic properties, especially suitable for energy storage. In accordance with the study's findings, the $\alpha$-$Fe_2O_3$@D composite boasts an impressive minimum reflection loss ($RL_{min}$) of − 54.2 dB at 11.52 GHz, achieving optimal performance with a slender absorber thickness of 3 mm. The composite further showcases a noteworthy frequency bandwidth, spanning 8.24 GHz (9.76–18 GHz), wherein the microwave RL value remains below − 20 dB. This exceptional performance underscores the potential of $\alpha$-$Fe_2O_3$@D as a lightweight and stable material, offering advantages in energy storage applications. The composite material, $\alpha$-$Fe_2O_3$@D, has a lower density than $\alpha$-$Fe_2O_3$, making it a promising option for energy storage due to its potential for increased efficiency and reduced system weight. The study highlights the combined effects of magnetic loss from $\alpha$-$Fe_2O_3$ and dielectric loss of De in electromagnetic wave absorption. The unique structure and crystal shape of this composite suggests its potential for advanced energy storage applications [139].

In this study by Wang et al. [51], the synthesis and characterization of diatomite-like potassium iron disulfide ($KFeS_2$) using a multistep sacrificial template method via hydrothermal synthesis are presented. This bifunctional material exhibits exceptional properties facilitating both electrical

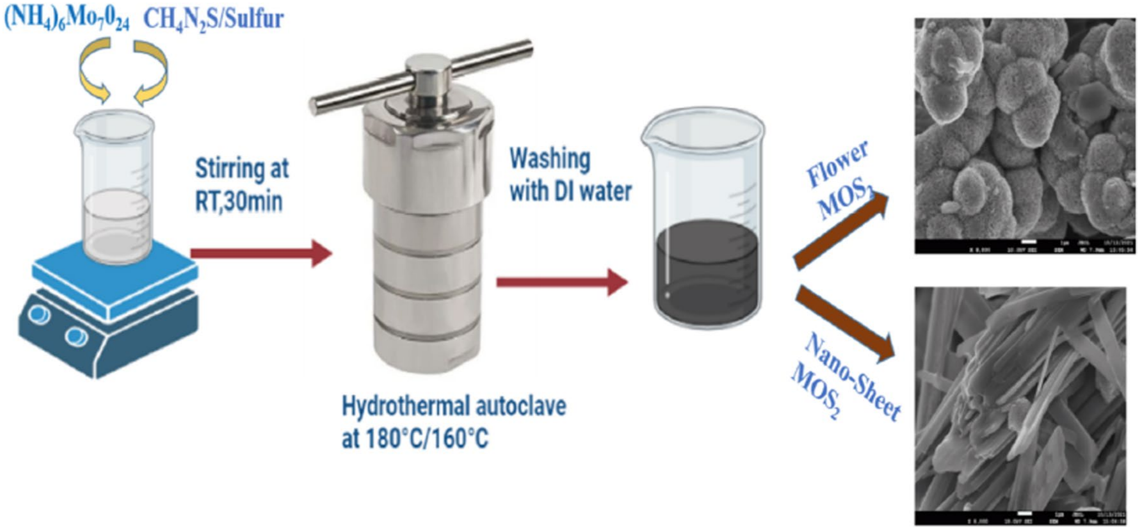

**Fig. 6** Diagram showing the hydrothermal synthesis process for creating $MoS_2$ nanoflowers and nanosheets. Source: [138]

energy storage and conversion. The porous and hollow structure of diatomite-like $KFeS_2$, with a high specific surface area, makes it effective for energy storage. It exhibits an impressive capacitance of 651 F/g at 1.0 A/g. Additionally, it shows excellent performance in the oxygen evolution reaction, with low overpotential and a small Tafel slope. These characteristics position diatomite-like $KFeS_2$ as a promising material for energy storage and conversion applications.

Comparatively, Xin et al., in two different studies, introduced a novel approach to fabricating hierarchically porous NiO-modified diatomite structures [45] and hierarchically porous $MnO_2$-modified diatomite structures [46] through a one-pot hydrothermal method. The structures of the electrode material produced by Xin et. al. [45] showcase a distinctive moss-like assembly composed of NiO nanofiber arrays, as shown in Fig. 7.

The electrochemical properties of these NiO-modified diatomite electrodes were thoroughly investigated using electrochemical impedance spectroscopy, galvanostatic charge/discharge tests and cyclic voltammetry. The resulting electrochemical properties detailed a remarkable performance of the unique NiO-modified diatomite structures by showing a specific capacitance value of 218.7 F/g. Notably, the electrodes display great cyclic stability, with 90.61% capacitance retention after 1000 cycles. This impressive capacitive behavior highlights the potential of these low-cost NiO-modified diatomite structures as promising electrode materials for supercapacitor development. The structure and morphology of the hierarchical structures of the $MnO_2$-modified diatomite electrodes are meticulously examined using X-ray diffraction spectroscopy (XRD) and focus ion beam scanning electron microscopy (FIB/SEM). The outcomes reveal the growth of vertically aligned Birnessite-type $MnO_2$ nanosheets on purified diatomite, forming an intricate hierarchical architecture, as shown in Fig. 8.

The electrochemical properties of $MnO_2$-modified diatomite electrodes were studied in a 1 M $Na_2SO_4$ electrolyte using various tests. Results show that the modified electrodes have excellent reversibility and high-rate capabilities. Specifically, $MnO_2$-modified diatomite exhibits a capacitance of 202.6 F/g, while $MnO_2$ nanostructures obtained by etching diatomite show a capacitance of 297.8 F/g. The electrodes maintain an impressive capacitance retention of 95.92% after 5000 cycles, highlighting their potential as cost-effective and promising materials for supercapacitors.

Furthermore, Li et al. [140] introduced a solution to the current environmental challenges associated with carbon nanotubes (CNTs), such as their susceptibility to agglomeration and the pollution resulting from chemical vapor deposition (CVD). Li and colleagues created hollow polyhedrons with nitrogen-doped carbon nanotubes and Co3O4 nanoparticles to mitigate these issues using hydrothermal, stirring, and pyrolysis methods, as depicted in Fig. 9. The evenly placed polyhedrons on diatomite's outer surface, with its natural porous structure, prevent CNT agglomeration. The composite material shows great performance in electrochemical tests, with a high specific capacity of 894.6 F/g at 2 A/g, impressive rate performance, and strong cycling properties. Furthermore, a constructed supercapacitor using $Co_3O_4$ NP@CNTs@Diatomite//GR achieved a high energy density of 36.8

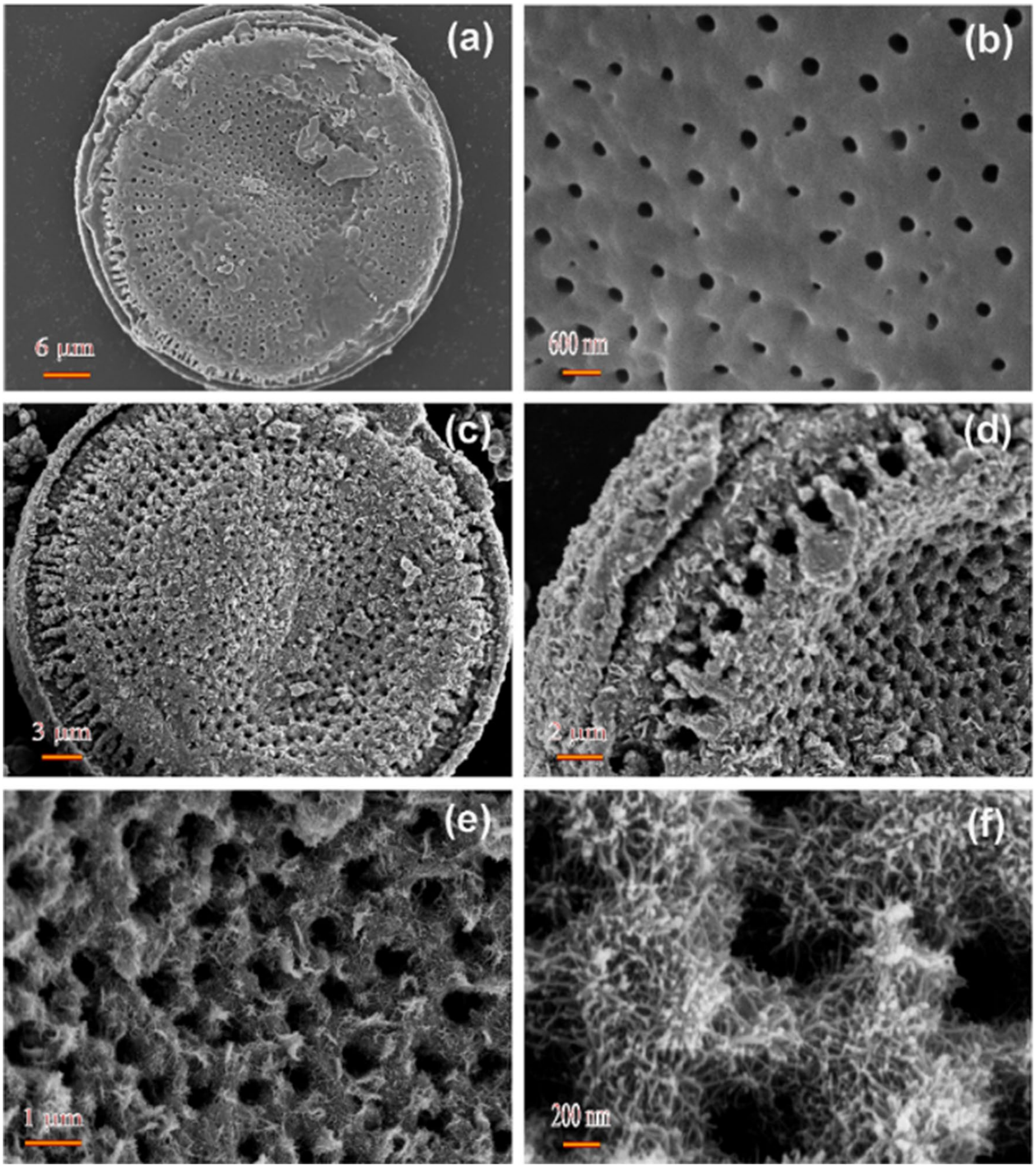

**Fig. 7** **a**, **b** Scanning electron microscope (SEM) pictures of purified diatomite, **c**, **d** composites of diatomite modified with NiO, and **e**, **f** pores located at the center of the diatomite shell. Source: [45]

Wh/kg and an impressive power density of 16,326.6 W/kg. This electrode design offers an eco-friendly method for decorating carbon nanotubes on a specific surface and introduces a new diatomite electrode material.

To explore the synthesis method of diatomite bio-templated electrode materials discussed earlier, Table 1 provides information on the diatomite usage, the employed synthesis technique, and the surface morphology of the diverse diatomite bio-templated synthesized electrode materials.

## Characterizations of diatomaceous earth bio-templated electrode material for energy storage applications

### Physiochemical characterization

#### Diffractometry

X-ray diffraction quickly analyzes crystalline substances by using them as diffraction gratings for X-rays. This

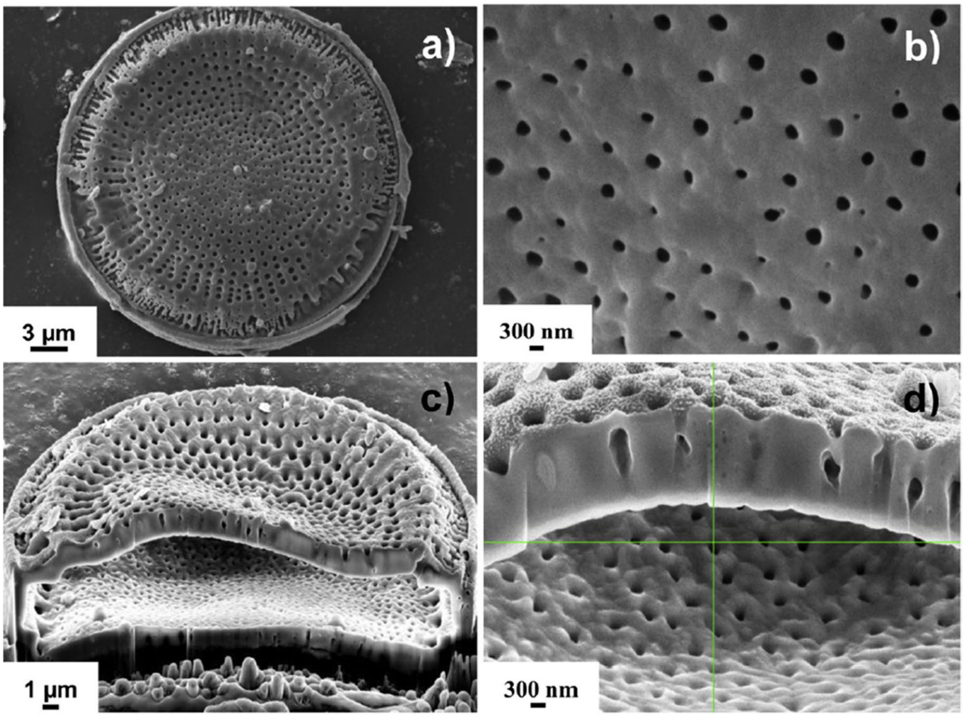

**Fig. 8** SEM pictures of purified diatomite: **a** individual diatomite; **b** surface pores distribution; **c**, **d** cross-sections of diatomite created using FIB milling. Source: [46]

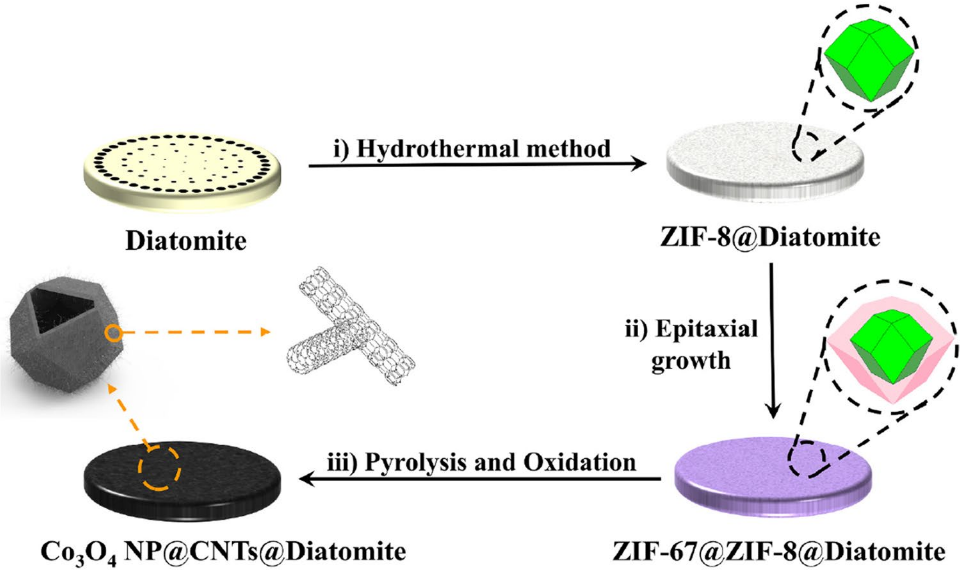

**Fig. 9** A schematic representation of the synthesis process for $Co_3O_4$ NP@CNTs@Diatomite. Source: [140]

technique is key for studying crystal structures and atomic spacing. It works by directing focused, monochromatic X-rays onto a crystal sample. When Bragg's Law is satisfied, constructive interference produces detectable diffracted X-rays. The sample is scanned through various $2\theta$ angles to study different diffraction directions, covering the lattice's orientations. Diffraction peaks are converted to d-spacings, allowing mineral identification by comparing them with standard reference patterns. All diffraction methods use X-rays generated in an X-ray tube, directed at the sample, and collect the diffracted rays. X-ray diffractometers have three main parts: an X-ray tube, a detector, and a sample holder. X-rays are produced by bombarding a target material in the tube with accelerated electrons. Filtering ensures monochromatic X-rays for diffraction. Copper

**Table 1** Overview of the synthesis techniques, diatomite usage, and the surface morphology or features of several diatomite bio-templated synthesized electrode materials

| Diatomite use | Synthesis technique | Electrode material synthesized | Surface morphology | Ref |
|---|---|---|---|---|
| Diatomite as a template material | Template and hydrothermal synthesis method | Diatomite-like potassium iron disulfide ($KFeS_2$) | Hollow, porous, and cake-like morphology | [51] |
| Cultured diatom as a template material | Template method | CD-$FeO_x$ | Porous architecture and high surface area | [33] |
| Hollow diatom silica structures as a template material | Template and hydrothermal synthesis method | Diatomite@$TiO_2$@$MnO_2$ | | [101] |
| Diatom as a direct hard bio-template material | Hard template method | Meso/macroporous hierarchical silica | Hierarchically structured porous materials | [100] |
| Uniform arrangement of polyhedrons on the external surface of diatomite | Hydrothermal synthesis | $Co_3O_4$ NP@CNTs@Diatomite//GR asymmetric electrode | Porous diatomite structure preventing CNT agglomeration | [140] |
| Diatomite as a template material | Hydrothermal synthesis | Hierarchically porous $MnO_2$-modified diatomite structures | Growth of vertically aligned birnessite-type $MnO_2$ nanosheets on purified diatomite, forming an intricate hierarchical architecture | |
| Diatomite as a template material | Hydrothermal synthesis | Hierarchically porous NiO-modified diatomite structures | Distinctive moss-like assembly composed of NiO nanofiber arrays | [45] |
| Diatomite as a template material | Hydrothermal synthesis | α-$Fe_2O_3$-decorated De (α-$Fe_2O_3$@D) | | [139] |
| Diatomite as a substrate material | Chemical vapor deposition (CVD) | Carbon nanotubes (CNTs) on a Ni catalyst-diatomite substrate | | [125] |
| Diatomite as a substrate material | Chemical vapor deposition (CVD) | Multiwalled carbon nanotubes (MWCNTs) | | [128] |
| Natural diatomite as a template material | | N-doped hierarchical graphene (NHG) | | [110] |
| Diatomite as a substrate material | Chemical vapor deposition and hydrothermal synthesis | Nickel–iron sulfide nanosheets (NiFeSx) and carbon nanotubes (CNTs) on diatomite | Uniform dispersion of nanomaterials on its surface, thereby expanding active sites | [129] |
| Diatoms as a source of inspiration for advanced nanostructured biohybrids | Sol–gel method | Silica-based biohybrids | Intricate shapes of diatom frustules enable the production of 3D hierarchically structured materials | [19] |
| Diatomite as a template and a substrate material | Sol–gel method | ZnO nanoparticles on the porous surface of diatomite (DE) | ZnO nanoparticles exhibited a uniform distribution on both the frustules' surface and within the pores | [116] |

is often used, producing Cu-Kα radiation with a wavelength of 1.5418 Å for single-crystal diffraction. The diffractometer records the intensity of reflected X-rays as the sample and detector rotate. Intensity peaks occur due to constructive interference when the X-rays' geometry satisfies the Bragg Equation. The goniometer maintains the sample angle and rotation during this process. Powder patterns are usually collected at 2$\theta$ angles from ~ 5 to 70° in the X-ray scan. The resulting data provides valuable information on crystal structures and material composition [141–143].

Zhang et al. [46] examined purified diatomite and $MnO_2$-modified diatomite. Purified diatomite displayed high crystallinity with distinct peaks corresponding to crystalline $SiO_2$. $MnO_2$-modified diatomite showed peaks consistent with the standard XRD pattern of birnessite-type manganese oxide crystal. The broadening of a diatomite peak at 36.1° indicated $MnO_2$ decoration, as shown in Fig. 10. Confirmation of the birnessite-type manganese oxide crystal was achieved by etching the diatomite in NaOH solution.

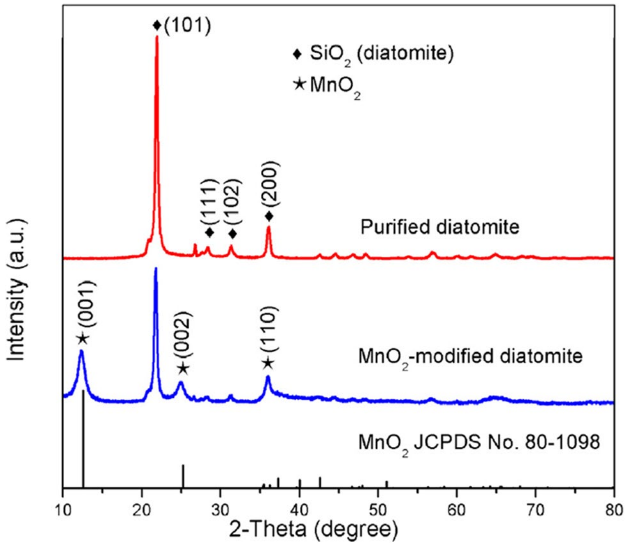

**Fig. 10** XRD patterns of clean diatomite and $MnO_2$-altered diatomite. Source: [46]

### Spectroscopy (FT-IR spectroscopy and Raman spectroscopy)

Spectroscopy is an experimental technique designed to obtain molecular insights into the studied system. The connection between observation and information relies on the theory of molecular interaction with electromagnetic or particle radiation. Typically, this interaction causes atoms and molecules to lose energy or gain. Describing the magnitude of these effects and understanding why they occur at specific wavelengths is a theoretical challenge best addressed within the framework of quantum mechanics. A fundamental aspect involves detailing the energy levels of molecules and interpreting the interaction between radiation and matter [144–146].

To explain the differences between purified diatomite and $MnO_2$-modified diatomite, Zhang et al. [46] used Fourier-transform infrared (FT-IR) spectroscopy to analyze both samples, as shown in Fig. 11. In Fig. 11a, key absorption bands for both samples are seen at 3445, 1634, 1092, 793, and 473 $cm^{-1}$. The 3445 $cm^{-1}$ band indicates the O–H stretching of water molecules and hydroxyl groups. The 1634 $cm^{-1}$ band likely comes from bending vibrations of O–H groups in adsorbed water. Peaks at 1092 $cm^{-1}$ and 793 $cm^{-1}$ confirm Si–O stretching vibrations in both samples, showing material preservation after modification. In purified diatomite, the 473 $cm^{-1}$ band may be from Si–O-Si bending, while in $MnO_2$-modified diatomite, new peaks suggest structural changes. Figure 11b highlights significant peaks in $MnO_2$-modified diatomite between 450 and 600 $cm^{-1}$, with 484 and 514 $cm^{-1}$ peaks indicating the primary absorption bands of birnessite related to Mn–O stretching in the structure.

However, Sun et al. [147], demonstrated the Raman spectra of EG and Si/GNs hybrid in Fig. 12. Following the characteristic peaks observed in graphene Raman spectra,

**Fig. 11** FT-IR spectra comparison between **a** acidified diatomite and $MnO_2$-modified diatomite and **b** a magnified view of the $MnO_2$-modified diatomite spectrum (the boxed region inset in **a**) in the 450–600 $cm^{-1}$ range. Source: [46]

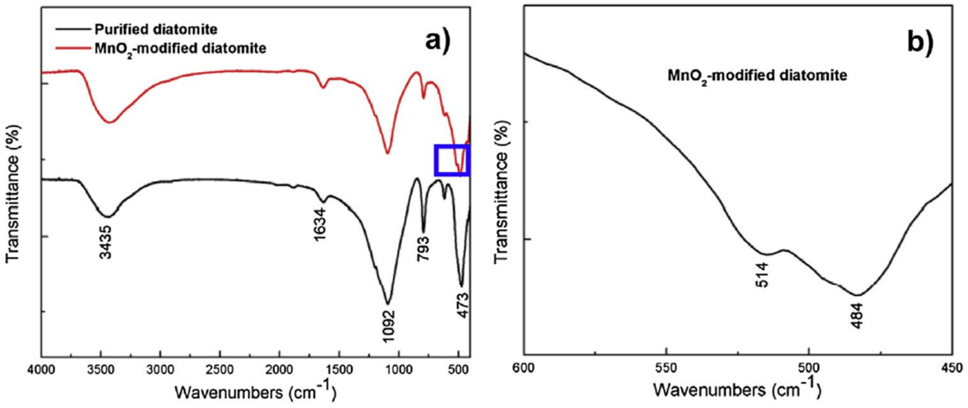

the D band signifies disordered carbon, edges, and defects, while the G band arises from ordered $SP_2$-bonded carbon. The EG initially displays a prominent G band alongside a broad D band, resulting in an ID/IG ratio of 0.48. However, following 10 h of P-milling, the intensity of the G band diminishes, accompanied by a rise in the D band, yielding an ID/IG ratio of 1.68, as observed in Fig. 12. These findings suggest a notable reduction in EG size along the c-direction and increased graphene defects during P-milling. Subsequently, efficient exfoliation of GNs from the porous and loosely structured EG during P-milling is inferred from the analysis. Furthermore, the layer content of GNs was evaluated through DSC tests conducted in an oxygen atmosphere, elucidating the extent of oxidation as a function of temperature. Consistent with prior findings, incorporating Si nanoparticles during P-milling resulted in the production of graphitic material with fewer GN layers, which exhibited heightened reactivity with oxygen. This heightened reactivity manifested as an exothermic peak at lower temperatures.

Also, Kim et al. [148] present the Raman spectra analysis of Si-$FeSi_2$/EG nanocomposite powders as shown in Fig. 13. The peaks detected at 1330 and 1580 $cm^{-1}$ are associated with the D and G bands, respectively. The D band (~ 1330 $cm^{-1}$) signifies disordered carbon at graphite edges with $A_{1g}$ symmetry and other defects, whereas the G band (~ 1580 $cm^{-1}$) originates from ordered carbon with $E_{2g}$ symmetry. The Raman intensity ratio, $R$ ($I_D/I_G$), calculated via Gaussian function fitting, is approximately 0.89, indicating comparable intensities of the D band and G band. This similarity could be attributed to a reduction in the size of the EG and structural distortion of $sp^2$ domains induced during mechanical milling.

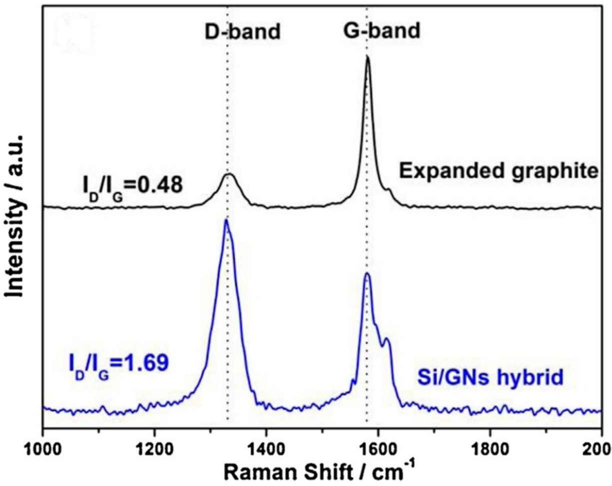

**Fig. 12** Raman spectra for EG and Si/GNs hybrid. Source: [147]

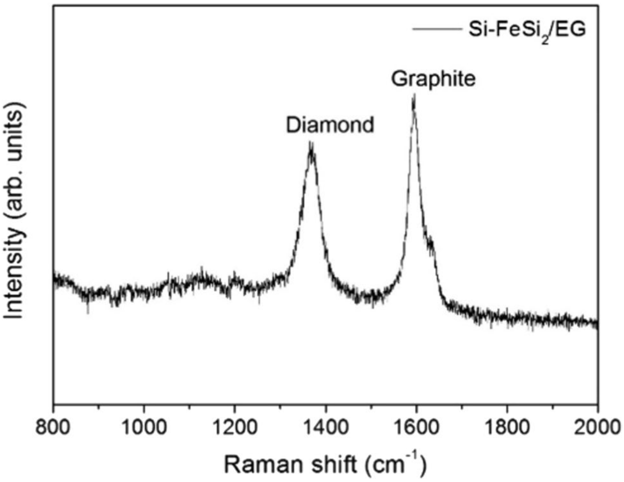

**Fig. 13** Raman spectra of the Si-$FeSi_2$ /EG nanocomposite milled for 6 h. Source: [148]

## Surface area and pore size analysis

BET analysis utilizes a fully automated analyzer to precisely assess specific surface area by measuring nitrogen multilayer adsorption relative to pressure. This technique evaluates both external and pore areas, providing essential information on the total specific surface area ($m^2/g$) and offering insights into the factors affecting the particle size and the surface porosity in various applications. Furthermore, BJH analysis is a technique primarily used to estimate pore area and specific pore volume through adsorption and desorption of nitrogen gas. This method characterizes pore size dispersal freely of exterior area, contributing to the particle size of the material [149–151].

In the investigation by Zhang et al. [46], surface properties of the $MnO_2$-modified diatomite were analyzed using the Brunnauer-Emmett-Teller (BET) method and nitrogen adsorption and desorption measurements. Figure 14 displays equivalent nitrogen adsorption–desorption isotherm and pore size distribution curves. The isotherm shown in Fig. 14a indicates typical characteristics of a mesoporous material with a hysteresis loop at high partial pressures, suggesting the presence of macropores on the diatomite surface. The Brunnauer-Emmett-Teller analysis revealed a great specific surface area value of 57.5 $m^2/g$ for the $MnO_2$-modified diatomite, significantly surpassing values reported in prior studies. The Barrette-Joynere-Halenda (BJH) pore diameter dispersal curve in Fig. 14b illustrates a broad pore size distribution, indicating a hierarchically porous structure in the composite. This hierarchical morphology, with well-advanced pore features, is useful for enhancing applications in electrochemical energy storage devices by facilitating rapid electrolyte transport through large pore channels and providing enormous active spots for chemical reactions within small pores.

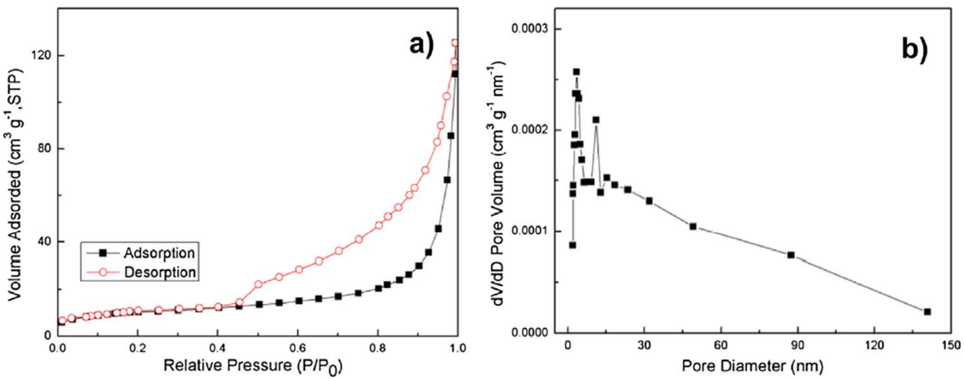

**Fig. 14** **a** $N_2$ adsorption–desorption curves; **b** pore size distribution of the $MnO_2$-modified diatomite composite. Source: [46]

## Microscopy (scanning *electron* microscopy (SEM), transmission *electron* microscopy (TEM), and *electron* backscattered diffraction (EBSD))

Surfaces represent distinct states of matter with compositions and geometries differing significantly from the bulk of a substance. Serving as the crucial link between a material and its surroundings, surfaces influence various processes due to physical characteristics like particle size, shape, and roughness. These properties impact absorption, agglomeration, compressibility, combustibility, packing, and segregation [152]. To understand these aspects, it is essential to characterize both the surface structure and material composition in detail. This study employs two methods, namely, SEM [153], transmission electron microscopy (TEM) [154], and electron backscattered diffraction (EBSD) [155]. SEM utilizes a focused electron beam to scan the surface, generating an enlarged image based on the sample's interaction with electrons. With SEM, images can be magnified up to 2 million times. In contrast, TEM captures the interior structure of a sample using a broad electron beam, revealing morphology, chemical composition, and crystal structure. Both methods provide valuable insights into the surface morphology of materials, contributing to a comprehensive understanding of their properties [156].

EBSD is a technique employed to analyze crystallographic orientations, misorientations, texture trends, and grain boundary types in engineering materials. In SEM, an electron beam impinges on a specimen, and an image is formed by detecting the intensity of electrons scattered from the specimen. The EBSD technique relies on detecting the overall intensity of scattered electrons and the distribution of scattering angles. Using a position-sensitive electron detector. With a crystalline specimen, Kikuchi lines are observed in the image formed on the detector, each line corresponding to a crystallographic plane. Pairs of Kikuchi lines, known as Kikuchi bands, form the electron backscattered pattern (EBSP). The width of Kikuchi bands is influenced by Bragg's law and the specimen-to-screen distance. The Kikuchi pattern is stored in a computer, compared to simulated patterns based on the specimen's structure and mineral database, determining crystal orientation. By scanning the electron beam across an area of the specimen, EBSD thus allows the creation of a map of the crystal structures and orientations in the microstructure of the specimen [155, 157–159].

In a work conducted by Zong et al. [160], diatomite is recognized for its composition of non-crystalline $SiO_2$ without cristobalite. Industrial usage of the diatomite necessitates its heating above 1200 °C to eliminate impurities, a process that transforms non-crystalline $SiO_2$ into cristobalite. Figure 15a, b presents both low- and high-magnification SEM images of diatomite, revealing particles with a diameter of approximately 50 μm and randomly distributed pores measuring around 100 nm. Additionally, low and highly magnified TEM images (Fig. 15c, d) corroborate the oval-shaped nature of the nanopores.

Also, Li et al. [42] investigated the impact of reaction environments on the morphology and microporosity of diatomite. Crystalline diatomite (c-diatomite) with a discus-like shape (see Fig. 16a–c) exhibited resistance to alkaline dissolution due to its rigid structure. A dilemma arose in choosing reaction parameters: the need for an extremely basic solution for silica source utilization conflicted with the slow growth of mesoporous silica (m-$SiO_2$) and the risk of breaking c-diatomite's structural integrity. A two-step hydrothermal process addressed this issue. Firstly, c-diatomite underwent a short hydrothermal treatment in a strong alkaline solution, partially transforming it to an amorphous state without compromising structural integrity. TEM images revealed a rougher surface with amorphous silica after this treatment as shown in Fig. 16d–f. In the second step, the pH was lowered to 10, facilitating the formation of m-$SiO_2$ while preserving c-diatomite's morphology and macro-porosity. The resulting product, termed c-diatomite/m-$SiO_2$, demonstrated m-$SiO_2$ distributed on c-diatomite backbones, attributed to the interaction between surfactant $CTA^+$ ions

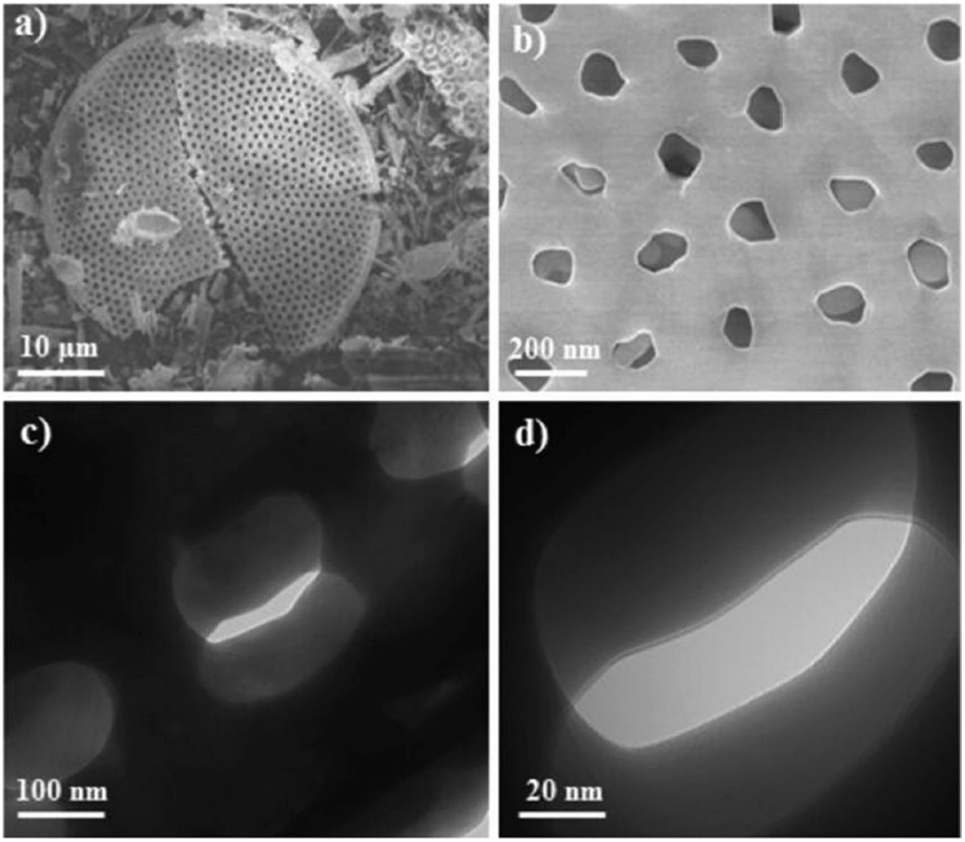

**Fig. 15** Low (**a**)- and large (**b**)-magnified SEM images and low (**c**)-, large (**d**)-magnified TEM images of the diatomite particles. Source: [160]

and amorphous silica or adsorbed siliceous species. The positively charged surfactant CTA$^+$ ions were adsorbed onto the negatively charged c-diatomite surfaces, promoting m$SiO_2$ formation restricted to the surface, as depicted in Fig. 16g–i.

However, Quinn et al. [161] demonstrated the potency of SEM in tandem with EBSD as a formidable tool for quantifying grain orientations and morphologies, particularly evident in NMC. In their study, they illustrated in Fig. 17A Aan EBSD inverse pole figure (IPF) map showcasing the crystallographic orientations of grains within the cross-section of a typical NMC particle, replete with smaller grains. Grains and particles were defined using the IQ map in Fig. 17B, while the SEM image in Fig. 17C served as partial validation of grain boundary locations. Each color in Fig. 17A represented a specific direction in the crystal, denoted by a Miller-Bravais index. Similar colors indicated akin orientations, with a specific color representing a vector oriented normal to the sample (pointing out of the page). For instance, an index of 0001 (red) suggested the *c*-axis of the grain pointing outward from the page. Nevertheless, it is important to note that the utilization of specific directions (0001, 1100, 0110, and 1210) assumed a sixfold symmetry, which might lead to variations in orientation due to the trigonal system of NMC. Consequently, analogous colors in Fig. 17A might sometimes signify different orientations. Despite its utility, the IPF map provided an incomplete depiction of the 3D orientation of a crystal, thus limiting the understanding of NMC orientation. To address this limitation, Quinn et al. [161] later introduced Bunge-Euler angles and vector-based descriptions. Moreover, the processed EBSD data typically included two measures of data quality: IQ and confidence index. A low confidence index (depicted as black in Fig. 17A) indicated ambiguity in discerning multiple orientations. The IQ map (Fig. 17B) served as a crucial metric for the quality of the Kikuchi diffraction pattern, with brighter IQ values correlating with sharper patterns. The SEM image (Fig. 17C) also provided finer morphological detail despite the challenge of clear grain identification due to low contrast. However, it is significant that Fig. 17A, while qualitatively coloring similar orientations, suffered from information loss by representing the orientation of a 3D body using only one crystal direction. In contrast, EBSD offered more comprehensive information by providing the 3D crystal orientation at each pixel, often reported as three angles specifying sequential rotations about different axes [161].

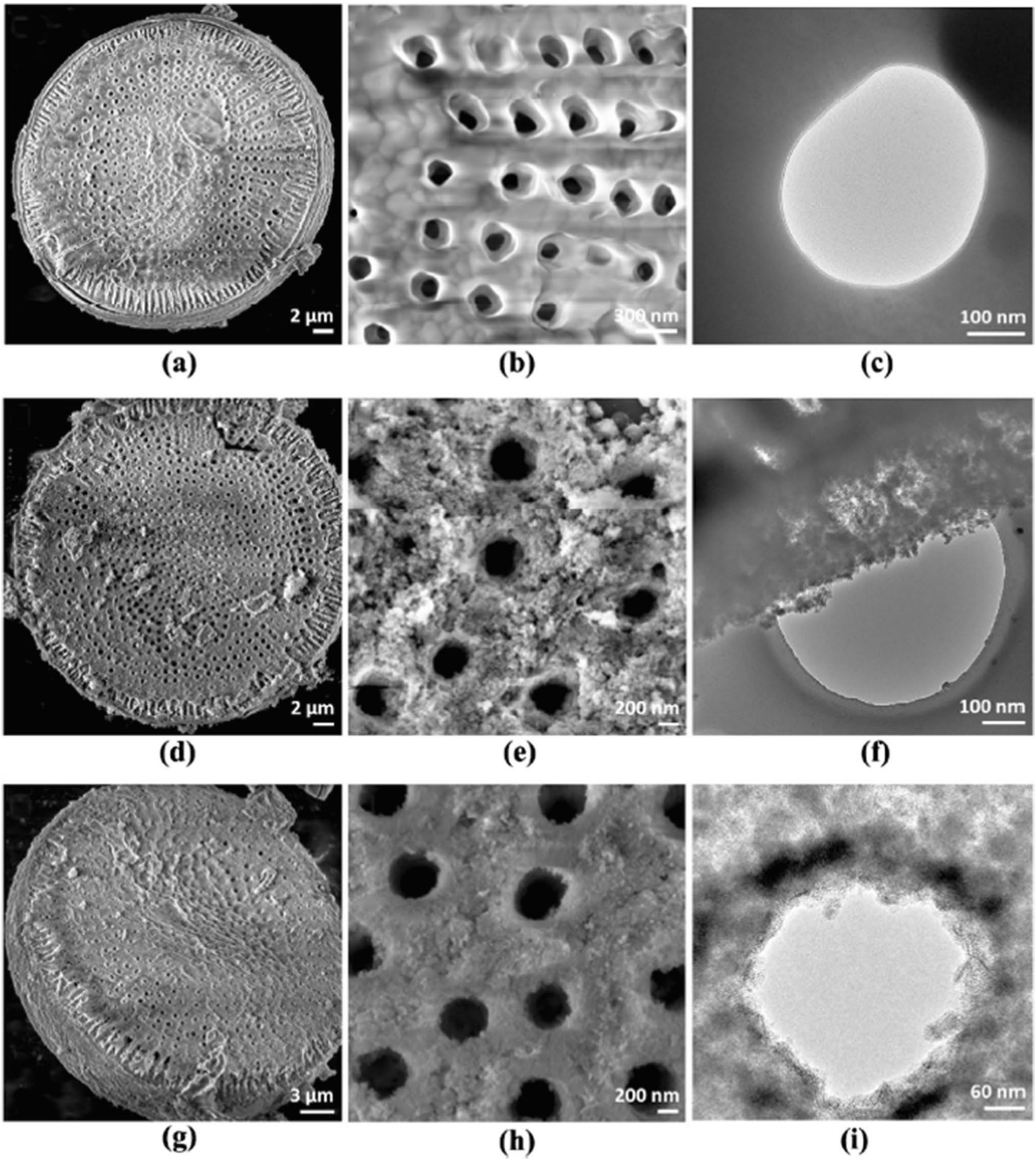

**Fig. 16** SEM and TEM images of **a**–**c** natural c-diatomite, **d**–**f** c-diatomite after initial pre-treatment, and **g**–**i** c-diatomite/mSiO$_2$ composite after secondary hydrothermal treatment. Source: [42]

## Electrochemical characterization

The current emphasis on advancing energy storage technologies [162] aims for high performance at low cost, driven by rising energy demand and the need for clean, renewable sources [70, 163]. The efficient use of electricity generated from renewable sources, such as wind [164] and solar energy [21, 165], depends on the creation of sustainable and economical energy storage systems to integrate erratic energy into the electrical grid [166]. Electrochemical energy storage

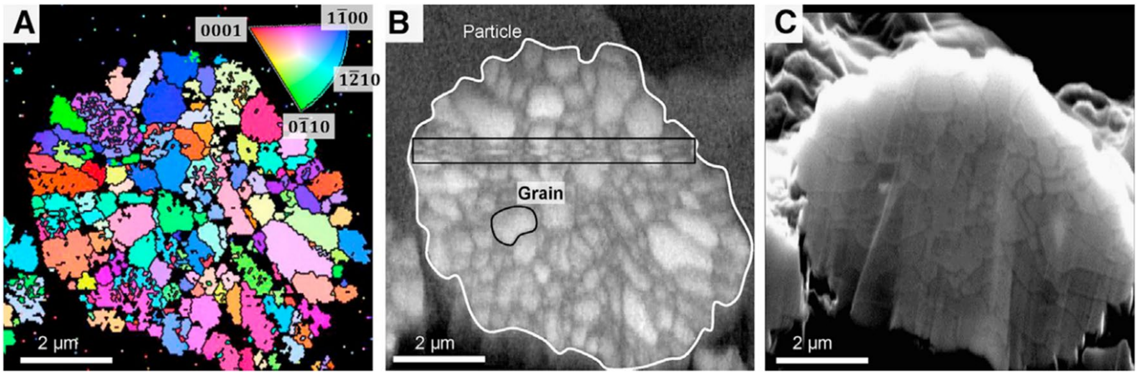

**Fig. 17** EBSD IPF map (**A**) and corresponding EBSD IQ map (**B**) used for particle and grain segmentation of polycrystalline NMC532, along with a SEM image (**C**). The boxed region in **B** is considered an artifact. Source: [161]

systems [167], particularly batteries [168], have shown capable solutions to address this demand. While supercapacitors, lithium-sulfur, and lithium-ion (Li-ion) batteries have been widely employed in portable electronic devices, their application has extended to the rapid growth of electric vehicle commercialization [22, 65]. In the pursuit of even more efficient and sustainable energy storage solutions, several battery technologies beyond supercapacitors and lithium-ion batteries, including lithium-sulfur (Li–S), magnesium (Mg) batteries, and sodium-ion (Na-ion), have attracted significant consideration from the scientific research community due to their sustainability, cost-effectiveness, and/or high capacity [70, 169]. However, these technologies face challenges that must be addressed in order to compete with the established Li-ion batteries [64]. Achieving the progress of high-performance battery systems necessitates the investigation of novel and capable materials coupled with a deep understanding of the storage mechanism. This understanding includes aspects such as the interaction of electrodes with electrolytes, redox reactions, and aging mechanisms of the science of each cell component [82, 170]. The comprehensive evaluation of new electrode materials involves characterizing their electronic structure, crystal structure, chemical composition, and morphology [171, 172]. Observing the development of these characteristics during the process of the electrochemical cell provides valuable insights. Recognizing the crucial role of advanced characterization techniques [173, 174] in the research and development of supercapacitors and batteries [127, 169], this chapter serves as an overview of some of the most central techniques generally utilized for assessing these energy storage systems. Researchers aim to enhance the understanding of material behaviors, ultimately contributing to the advancement of energy storage technologies [175]. Electrochemical measurements can be conducted using either a three-electrode or two-electrode configuration. In a two-electrode system, the fabricated electrode material is typically designated as the working electrode (WE) material, whereas the extra electrodes serves the dual purpose of a reference electrode (RE) and a counter electrode (CE) or an auxiliary electrode (AE) [162, 176]. To function effectively as a reference and auxiliary electrode, the auxiliary electrode (AE) should exhibit a little overpotential and maintain a steady potential throughout the electrochemical procedures. Examples of suitable materials for such roles in sodium cells and rechargeable lithium ions are sodium and lithium metals [177, 178]. Positive charged electrodes are commonly examined in two-electrode system, with the corresponding metal piece acting as the reference electrode (RE). This setup provides insights into the overall system behavior, offering a more accurate representation of the characteristics projected in a commercial cell [179]. Consequently, two-electrode cells find extensive use in cycle life evaluations, especially when explicit reactions at either electrode are not the principal focus [180]. A common two-electrode cell setup encompasses Swagelok cells and coin cells, which are favored for their ease of assembly and cost-effectiveness, particularly when a separate reference electrode is unnecessary [181]. As the outcome obtained in a two-electrode system is a result of combing the signals from both the working and the auxiliary electrodes, it is assumed that the electrochemical feedback at the auxiliary electrode is sufficiently minor, allowing the total electrochemical effect to represent the properties of the working electrode. However, situations may arise where the working electrode signal needs to be distinctly separated to analyze the mechanisms fully or where no appropriate material can function as both the auxiliary and reference electrode [182, 183]. In such cases, a three-electrode setup becomes essential. A reliable RE is crucial in a three-electrode configuration, providing a stable and accurate voltage [184, 185]. Examples of suitable materials for RE include silver/silver chloride [186], saturated calomel [187], and mercury/mercury oxide electrodes for aqueous electrolyte systems [188, 189], as well as silver/silver nitrate or ferrocene for non-aqueous systems [56, 106]. The three electrodes are typically immersed in a beaker cell [190], and various cell setups such as the Conflate cell [65, 182], T-shaped Swagelok cell [179, 191], and modified coin cell [192–194] are available, ensuring airtightness and minimizing electrolyte requirements [176, 182, 195]. It is important to note that careful consideration is necessary for impedance measurements [196] due to the significant influence of cell geometry on the results.

### Cyclic voltammetry curve analysis

Cyclic voltammetry [25, 178], a dynamic electrochemical measurement technique, involves tracking current with potential. This approach involves cyclically conducting successive potential scans between the working electrode and the reference electrode [197]. During these scans, the electrical current is measured at both the working and counter electrodes. The resulting data is graphed to represent current (in amperes) against applied potential (in volts), producing the cyclic voltammogram trace [198, 199]. Furthermore, the possible range might be limited by the stability range of the electrolyte. Cyclic voltammetry, widely discussed in the literature, offers valuable quantitative and qualitative information about capacitive behavior at the electrode/electrolyte junction. Importantly, it is effective in identifying dependent faradic reactions. A standard cyclic voltammogram curve is an investigative tool for evaluating capacitance [196, 200, 201]. A rectangular cyclic voltammogram (CV) is represented in an ideal supercapacitor response, as shown in Fig. 18a. However, practical applications may result in a slightly slanted rectangular shape attributed to redox reactions indicative of pseudocapacitive behavior (Fig. 18a). The presence of two redox peaks, mostly indicating faradaic behavior, is illustrated in Fig. 18b [176]. Verma et al. [71] conducted a comprehensive study on CV plots obtained from both three-electrode (3E) and symmetric two-electrode (2E) systems. The findings showed that 3E systems had higher specific capacitance values than 2E systems [71]. Cyclic voltammetry is a versatile electrochemical method widely employed to comprehensively study a system's behavior, encompassing thermodynamics and kinetics [202, 203]. It is an advanced technique involving both potentiometry and voltammetry. Potentiometry measures electric potential in a static electrochemical cell, while in voltammetry, current is measured as the potential between two electrodes changes [97, 171, 204].

CV measurements were conducted at various scan rates, expressed in mV/s while maintaining a constant current density in A/g [205, 206]. The derivative of charge Q with respect to potential V, as mentioned in Eq. (1) is the differential capacitance C, providing important insights into the process [64, 112] as shown in Eq. (2). Equation (1) is the fundamental mathematical relation governing charge storage at a constant current, whereas Eq. (2) is the estimation of specific capacitance from cyclic voltammetry curves at varying current density.

$$C = \frac{Q}{V} \tag{1}$$

where $C$ is the capacitance, $Q$ is the charges, and $V$ is the voltage.

$$C_s = \int_{-v}^{+v} \frac{\mathrm{I}d\mathrm{V}}{mv((+v) - (-v))} \tag{2}$$

where $m$ is the mass of the electrode, $v$ is the scan rate, $\int_{-v}^{+v} \mathrm{I}d\mathrm{V}$ is the Integral area of CV curve, and $((+v) - (-v))$ is the operational potential window.

In a full supercapacitor cell, the mass of the fabricated electrode is multiplied by 2 [65, 181, 207], as shown in Eq. (3).

$$C_s = \frac{1}{2mv((+v) - (-v))} \int_{v_o}^{v_1} \mathrm{I(V)}d\mathrm{V} \tag{3}$$

where $m$ is the mass of active material on an electrode in gram, $v$ is the scan rate, $\Delta V$ is the potential window, and $\int_{v_o}^{v_1} \mathrm{I(V)}d\mathrm{V}$ is the area under the curve.

Using a 3-electrode setup yields a distinctive duck-shaped plot called a cyclic voltammogram [167, 184]. In 3-electrode electrochemical cells, a key component is the working electrode (WE), where the compound of interest undergoes reduction or oxidation. The working electrode must be conductive to facilitate the movement of charges to and from the solution. Common materials for the working electrode are platinum, gold, graphite, etc. [15, 186]. The reference electrode (RE) acts as a stable and non-polarizable reference point for measuring the potential of other electrodes. Common reference electrodes include the saturated calomel and AgCl/Ag electrodes [186, 187]. When a potential is applied to the working electrode, the counter electrode (CE) closes the electrical circuit in an electrochemical cell, registering the current between the working electrode and itself [208]. The supporting electrolyte must be chosen based on the electrolyte's solubility in the solvent, chemical and electrochemical inertness, and ability to dissolve both the compound of interest and the electrolyte [57, 93, 209]. The Nernst equation [186] (Eq. (4)), which is a thermodynamic mathematical model, is used to determine the concentrations of redox species at the electrode surface [65].

$$E_o = E^T + \frac{RT}{nF}\ln\frac{C_{\mathrm{Red}}}{C_{\mathrm{Oxid}}} \tag{4}$$

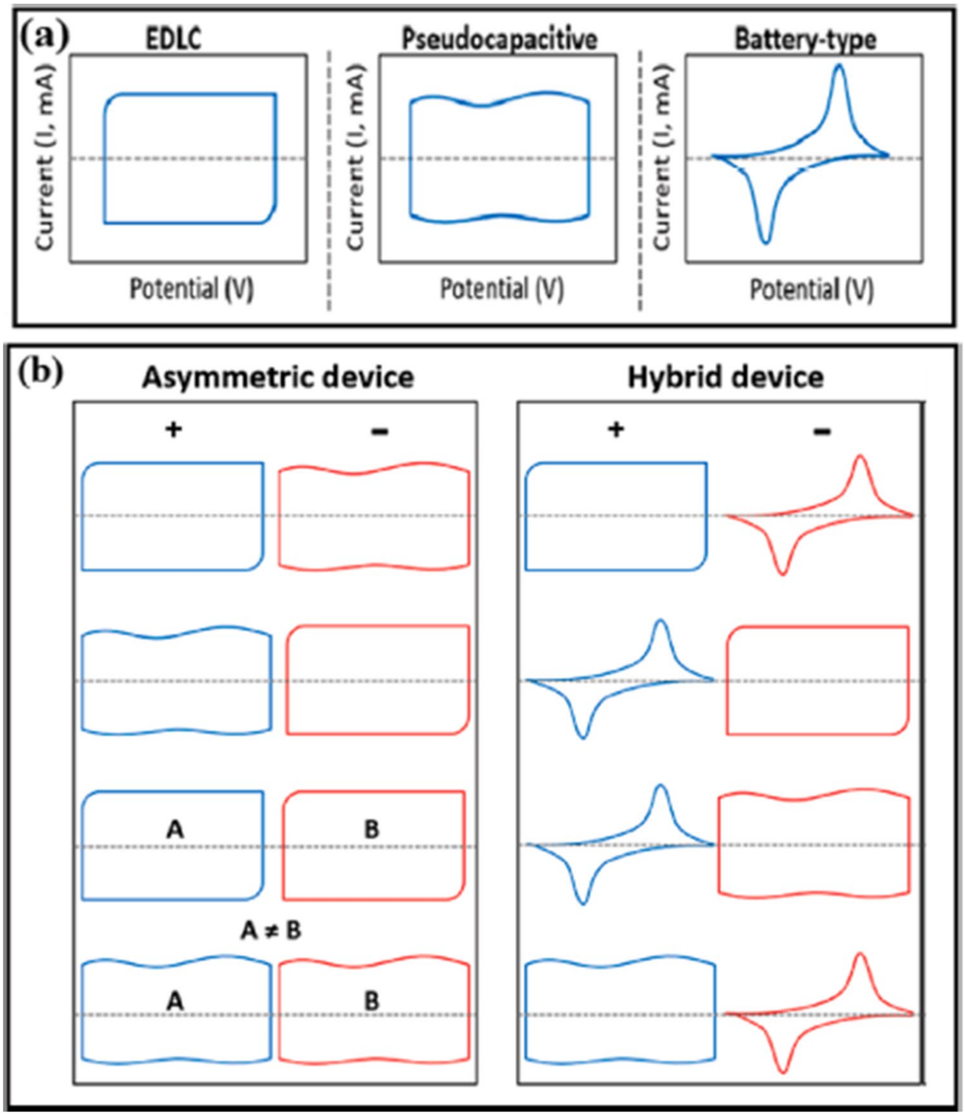

**Fig. 18** **a** Different shapes of cyclic voltammograms (CV) for electric double-layer capacitors (EDLC), pseudocapacitive, and battery-type materials. **b** Various asymmetric and hybrid CV configurations achieved by combining materials A and B. Source: [65]

where $E_o =$ Standard state reversible cell voltage, $E^T$ is the reversible cell voltage at an arbitrary temperature $T$, $F$ is the Faraday's constant, $R$ is the gas constant, $C_{\text{Red}}$ is the concentration of reductive species, and $C_{\text{Oxid}}$ is the concentration of oxidative species.

The Randles–Sevcik equation (Eq. (5)) [186] describes the relation between concentration and peak current, providing valuable information about the kinetics and phenomenon of the redox reaction.

$$i_p = 2.69 * 10^5 A C_o n^{3/2} D^{1/2} v^{1/2} \tag{5}$$

where $i_p$ is described as peak current, $A$ is described as area of electrode, $D$ is described as diffusion coefficient (cm$^2$/s), $C_0$ is described concentration, $v$ is described as scan rate, and $n$ is described as the number of electrons.

The overall relation between peak current and sweep rate assists in characterizing different nano-electrode materials using the mathematical model depicted in Eq. (6), which is a phenomenological observation.

$$i(\text{V}) = a v^b \tag{6}$$

where $i_p$ is described as peak current, $v$ is described as scan (sweep) rate, constant of proportionality, and $b$ is the exponential constant.

The calculation of the diffusion-controlled contribution and capacitive contribution relies on determining the value of parameter "$b$." Eq. (6) is then utilized to assess the kinetic performance of diverse nano-electrode materials. Cyclic voltammetry can be used to distinguish EDLC (electric double-layer capacitor) [69], pseudo-capacitance

[57], and battery-type materials [170] based on the shape of the CV curve and the value of the parameter "*b*." EDLC materials exhibit a rectangular CV curve with a constant value of "*b*" equal to 1. Pseudocapacitive materials display a nearly rectangular CV curve with inflection points where the value of "*b*" is close to 1. In contrast, battery-type materials exhibit redox peaks in the CV curve, signaling a quasi-reversible electron transfer process (refer to Fig. 18), with the typical value of "*b*" being around 0.5 [65]. Combining EDLC, pseudo, and battery-type electrodes in different ways leads to fabricating asymmetric and hybrid supercapacitors [210], as shown in Fig. 18. CV data can be used to assess specific capacitance (Cs) values, energy density, and power density of fabricated electrodes [12]. At lower scan rates, $C_s$ values increase, allowing ample time for electrolyte ions to undergo adsorption/desorption at the electrode surface [7]. CV is applied in diverse fields, such as the conversion and storage of energy (e.g., lithium-ion batteries, supercapacitors, and fuel cells), as well as in materials science, photonics, cell biology, neuroscience, electrical engineering, and condensed-phase physics [65].

## Galvanostatic charge and discharge cycles

Conducting electrochemical charging and discharging experiments on a new electrode material is a fundamental and pivotal practice in the quest for advanced supercapacitor and battery technologies [211]. A complete cycle involves charging the electrode and then discharging it, as shown in Fig. 19, with each of these steps constituting a half-cycle. Cycling is often performed in with a constant current (galvanostatically). The suitability of alternative charging methods varies depending on specific situations [117, 212]. It is crucial to end each charge or discharge half-cycle based on set time, charge level, or when the working electrode reaches a specific potential. Ignoring these limits can result in overcharging or overdischarging over multiple cycles. This means charging or discharging beyond the point where all active material is used up, leading to a breakdown in other cell components like the electrolyte, which either absorbs or provides electrons [162, 213, 214]. Non-aqueous electrolytes typically employ potential limits to prevent overcharging or

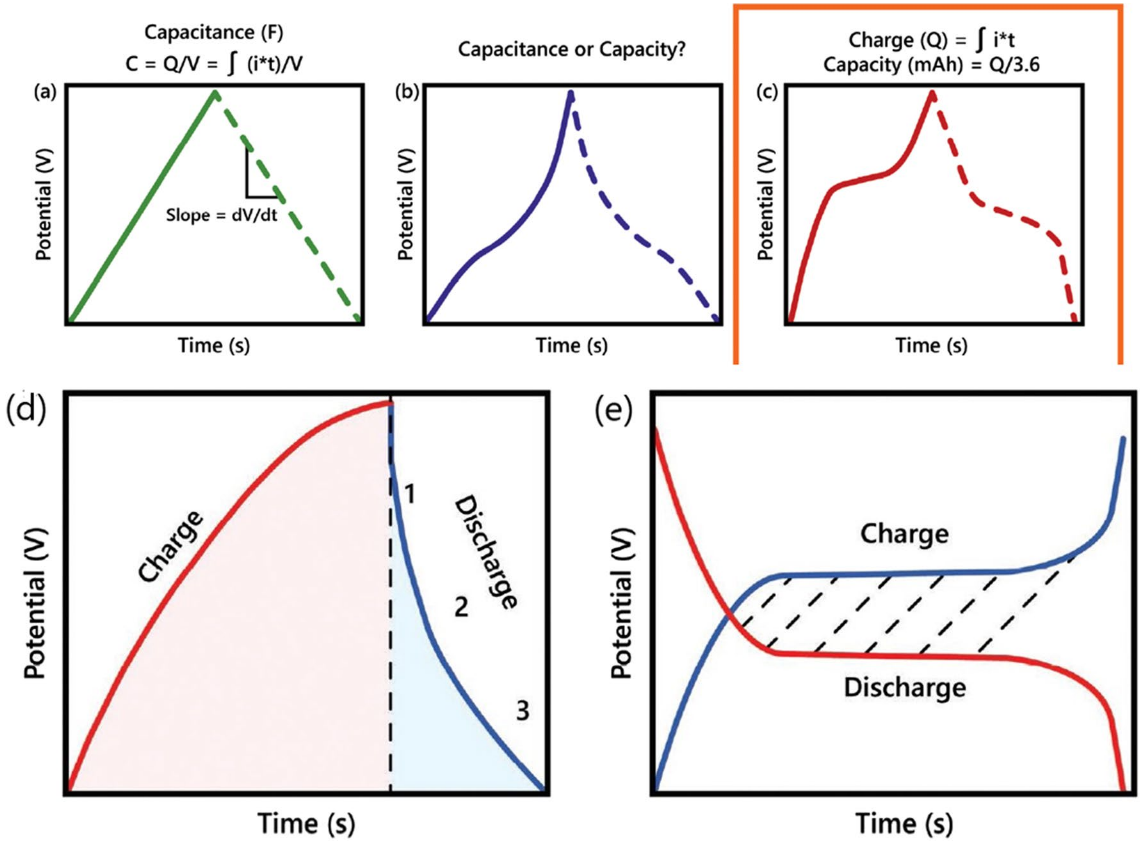

**Fig. 19** Illustrations depicting galvanostatic charge–discharge profiles showcasing linear and nonlinear behaviors over time for **a** EDLC, **b** pseudo-capacitive, and **c** battery-like materials. Additionally, demonstrating practical disparities between supercapacitors and batteries in GCD with **d** nonlinear supercapacitor curves and **e** curves showing charge (red) and discharge (blue) plateaus at varying potentials. Source [226]:

over-discharging, preserving the cell's state of health. Excessive charging or discharging in aqueous cells usually generates $H_2$ or $O_2$ gas, which can be safely vented. This permits the application of time or capacity limits [215, 216]. The term "*C*-rate" is prevalent in battery research, representing a constant current. Calculated by dividing the anticipated capacity ($C$) of the working electrode by the target hours for a complete charge/discharge, the *C*-rate aids in standardizing current for electrode capacity. Researchers determine the expected capacity by assessing the mass of the active material in the electrode, multiplied by the material's specific capacity (mAh/g), or by measuring the initial discharge capacity after one or two cycles. Reporting in *C*-rates assists readers by inherently adjusting the current for the electrode's capacity [65, 217]. For supercapacitor electrodes and complete supercapacitor cells, the specific capacitance is determined from galvanostatic charge and discharge data using Eq. (7) and Eq. (8).

$$C = \frac{2I_m}{V^2}\int_{v_o}^{v_1} \mathrm{V}d\mathrm{t} \tag{7}$$

In this equation, CCD represents charging-discharging capacitance, $V$ is the operational voltage window, and $I_m$ is the current density in A/g, $\int_{v_o}^{v_1}\mathrm{V}dt$ is the current integral area.

$$C = \frac{I_m\Delta t}{m\Delta V} \tag{8}$$

Herein, $I$ is the discharge current (A), $\Delta t$ is the discharge time (s), $\Delta V$ is the potential window, and $m$ is the mass of active materials.

Readers often focus on the discharge/charge curve, a graph showing potential against time (see Fig. 19), specific capacity, or a stoichiometric variable. The curve's length indicates charge or discharge capacity and is affected by factors like temperature, rate (/cm$^2$), and electrode condition. Higher capacities are usually achieved at higher temperatures, lower rates, and lower cycle numbers [200, 218]. Researchers should report how temperature, rate, and cycle number affect the capacity and shape of the potential curve to provide a thorough understanding of a new material. The curve's shape is influenced by both thermodynamics and kinetics, where flat plateaus suggest a two-phase reaction and sloped plateaus indicate a change in solution concentration [65, 175, 181]. Transitions such as ordering and staging are common in intercalation materials [168], with potential curve features more clearly observed in ${}^{dQ}/_{dV}$ as a differential capacity plot. While similar information is obtained from cyclic voltammograms (CV) [178, 199, 219], the differential capacity is measured at a constant current, giving electrochemical processes ample time to complete. Researchers studying electrode materials often prefer constant current differential capacity plots for superior resolution over CV [17, 189, 220, 221]. An essential part of characterizing new electrode material is evaluating its cycle life (cyclic stability) by comparing charge and discharge capacities with the cycle number. Reporting all cycles up to the 80% end-of-life threshold is crucial to accurately understand the cell's limitations [205, 218, 222]. Additionally, monitoring coulombic efficiency (CE) and the ratio of discharge to charge capacity reveals dependent reactions that redirect charge from the proposed reaction. Accurate measurement of CE is vital, considering that a large departure from 100% raises concerns about unsustainable rates of electrode or electrolyte consumption [223, 224]. In summary, the electrochemical investigation of new electrode materials involves a detailed exploration of charging and discharging behaviors, characterized by C-rates, potential curves, and advanced techniques like differential capacity plots. Understanding the impact of temperature, rate, and cycle number on the material's performance, along with accurate assessments of cycle life and coulombic efficiency, contributes to the ongoing advancement of battery technologies [65, 175, 225].

## Electrochemical impedance spectroscopy

EIS (electrochemical impedance spectroscopy) is commonly used to assess the impedance of an electrochemical system [65, 227]. It records the current response to an applied potential at different frequencies to analyze the impedance of electrochemical systems like supercapacitor and lithium-ion cells. The perturbative investigation involves applying a small AC voltage (1–10 mV) with frequencies from 1 to 1 MHz on a controlled DC voltage (usually OCV) due to the non-linear nature of the system's response [65]. High impedance in an electrochemical cell can cause large overpotentials [228], reduced energy efficiency, limited rate capability, and an increased risk of thermal runaway. It is crucial to study and understand the impedance evolution at each stage of discharge/charge and throughout extended cycling [229]. Usually, voltage drop comes from three sources: ohmic loss, charge transfer or activation polarization, and concentration polarization [65]. In supercapacitors and battery research, the Nyquist plot is frequently used to depict the impedance spectrum [65, 228, 230, 231]. It entails graphing the opposite of the imaginary part of impedance against the real part at various frequencies [206]. The Nyquist plot typically exhibits one [230] (for supercapacitors) or more semicircles [227] (for batteries) at high frequencies (representing charge transfer procedures) accompanied by a spike or 45° straight line at medium frequencies (indicating diffusion toward/moving away from the electrode material surface, known as Warburg impedance region or area) [65] and the vertical line or 90° straight line representing a highly capacitive material (electric double layer) [7] as shown in Fig. 20. In the Nyquist plot, the Warburg impedance manifests as a slanting line with a 45-degree slope. The impedance (Zf) displays a 45-degree phase shift on the bode plot. The values of Rw and Rct must be minimized to ensure a negligible IR drop, facilitating large output power. This is mostly critical in the setting of energy storage devices, where energy plays a pivotal role. It is essential to use symmetric axes when presenting the Nyquist plot [228]. EIS data are commonly analyzed by fitting the curve with an equivalent electrical circuit model (see Fig. 20). This method aids in understanding contributions from each interface or bulk process. To maintain physical relevance, the number of elements in the fit should be minimized, as an overly complex fit may lack significance. EIS provides supercapacitors with an alternating current in the frequency range of 0.01 Hz to 1 mHz. The circuit elements in the model, such as resistors which is usually represented as $R$ or $Z$, capacitors which is mathematically represented as $Z_c = iwC$, and inductors which is represented as $Z_L = iwL$ [175]. [65]. In practical terms, understanding interfacial diffusional processes (charge transfer) on electrodes can be complex. Charge transfer phenomena at electrode–electrolyte interfaces are seen as an extension of the semicircle from high to medium frequencies [231, 232]. The equivalent series resistance ($R_s$) is shown where the semicircle intercepts the real axis [233], the charge transfer resistance ($R_{ct}$) on the other hand is determined by analyzing the low-frequency regions, and it is equivalent to the diameter of the semicircle [234]. Lower charge transfer value indicates a quick charge transfer mechanism [65]. The Bode plot is created by graphing angular frequency ($w$) on the $X$-axis and either phase shift ($\theta$) or log $Z$ on the $Y$-axis [230]. Faradic impedance ($R_f$) for charge transfer and diffusional processes is calculated using Eq. (9) [65, 181].

$$R_f = R_{ct} + R_w \tag{9}$$

where $R_w$ is mathematically related as $R_w = \frac{\sigma}{w^{1/2}}$ and the Warburg coefficient $\sigma$ having a unit of Ω rad/s.

Warburg impedance (Zf) is determined using Eq. (10).

$$Z_f = \left(\frac{2}{w}\right)^{\frac{1}{2}}\sigma \tag{10}$$

The phase angle for the Bode plot is calculated using Eq. (11).

$$\theta = \tan^{-1}\left(\frac{R_w}{R_{ct} + R_w}\right) \tag{11}$$

In an instance where the measurement process is a quasi-reversible process, $R_{ct} > 0 < 45°$, while for a reversible process, $R_{ct} = 0 \leq 45°$.

Finally, the electric double-layer capacitor is mathematically represented as $C_{dl} = \frac{1}{\sigma w^{1/2}}$.

$$C_{dl} = \frac{1}{\sigma w^{1/2}} \tag{12}$$

where $w$ represents angular frequency in rad/s.

Consequently, the charge transfer features of the fabricated electrodes are thoroughly examined through electrochemical impedance spectroscopy (EIS) as detailed by Talaie et al. [175]. Additionally, the Bode plot is constructed by plotting the frequency ($\omega$) on the $X$-axis and the phase shift $\theta$, which is represented as $\theta = \arg.Z.$, or log $Z$ on the $Y$-axis [228].

## Energy and power density

The energy and power density values are usually evaluated using different energy and power density mathematical

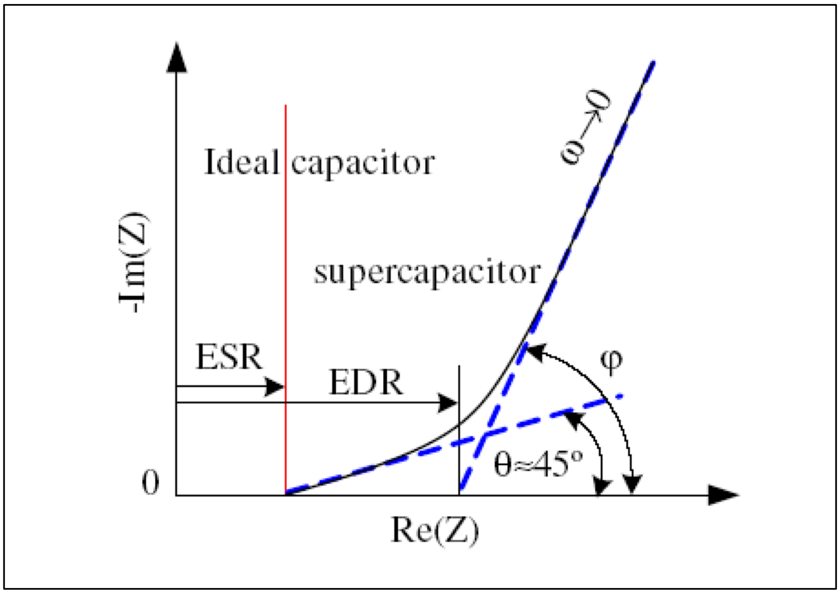

**Fig. 20** Graphical representation of equivalent series resistance (ESR) determination. Source: [235]

relations, including Eqs. (13) and (14) and Eqs. (15) and (16), respectively, from the CV curves data, GCD cycle data, and EIS data [65, 140, 170, 175, 236]. The (specific) energy and (specific) power density values of the electrochemical storage devices are usually represented graphically as a Ragone plot as depicted in Fig. 21.

$$E = \frac{C_s V^2}{2} \tag{13}$$

where $E$ is the energy density, $C_s$ is the specific capacitance, and $V^2$ is the voltage window.

$$E = \frac{C_s V^2}{2 \times 3.6} \tag{14}$$

where $E$ is the energy density, $C_s$ is the specific capacitance, and $V^2$ is the voltage window.

$$P = \frac{V^2}{4Rs} \tag{15}$$

where $P$ is power density, $V^2$ is the voltage window, and Rs is the internal series resistance.

$$P = \frac{E \times 3600}{\Delta t} \tag{16}$$

where $P$ is power density, $E$ is the energy density, and $\Delta t$ is the change in the discharge time.

## Mechanical property characterization

Conventional mechanical property testing methods, such as tensile, impact, and creep tests, rely on standard procedures and often require significant material quantities. However, innovative small specimen testing methods, such as Impression Creep, Small Punch Creep, Ball Indentation, and Nanoindentation, offer alternatives to assess the mechanical properties of materials with reduced material consumption. The Impression Creep test is designed to evaluate the creep deformation behavior of materials, while the Small Punch Creep test assesses both creep deformation and fracture properties. The Ball Indentation test methods can be employed to evaluate tensile strength, hardness, and fracture toughness. In contrast, Nanoindentation test methods reveal the tensile strength, hardness, and fracture toughness of individual phases in a material but not the bulk. These small specimen testing methods are particularly advantageous as they are less material-intensive, finding applications in materials development, structural integrity assessment for component life extension, and the characterization of mechanical properties across various materials or components [238].

In their study, Kim et al. [148] highlight the promising potential of silicon-based nanocomposite materials as anode candidates for lithium-ion rechargeable batteries. Despite the initial interest, the volume fluctuations experienced by silicon during charge and discharge cycles have led to

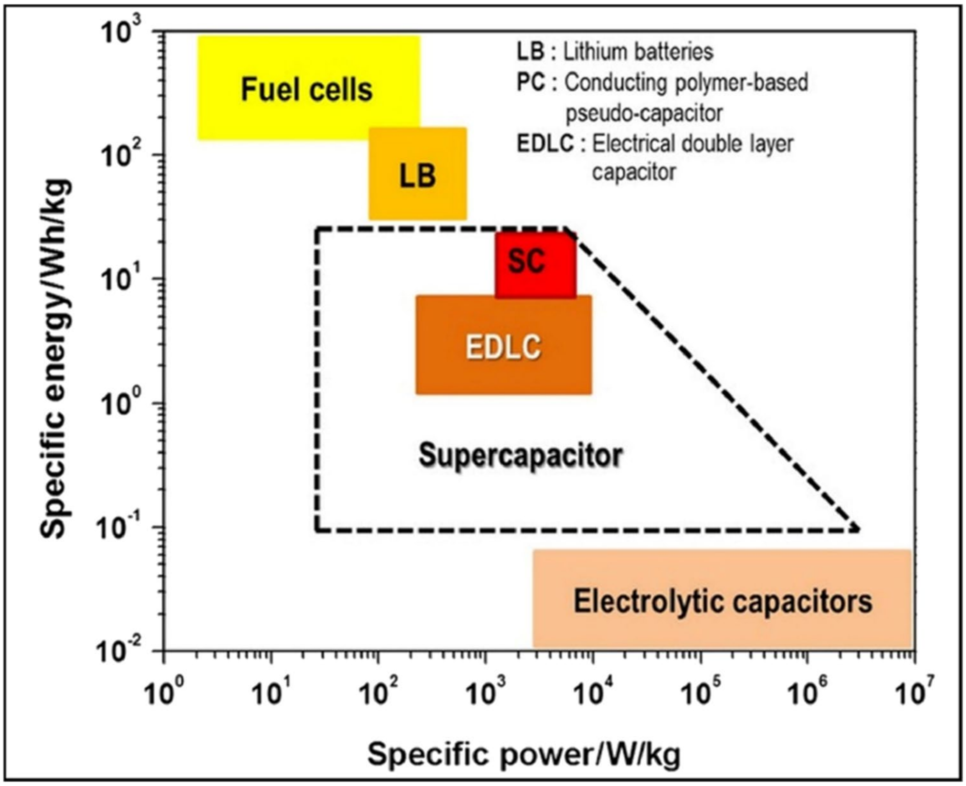

**Fig. 21** The Ragone plot compares power and energy densities of different energy storage methods. Source: [237]

diminished capacity retention and suboptimal coulombic efficiency. Addressing this challenge, the researchers present a novel Si-FeSi$_2$/EG nanocomposite, where nano-scale Si-FeSi$_2$ particles are encapsulated within exfoliated graphite (EG), synthesized through a scalable two-stage high-energy mechanical milling process. Utilizing XRD, FE-SEM, and HR-TEM techniques, they investigate the structure and microstructure of the nanocomposite. Analysis reveals a random dispersion of Si-FeSi$_2$ within the EG matrix. Remarkably, nano-indentation tests demonstrate that the Si-FeSi$_2$/EG electrode exhibits significantly higher elastic recoverable energy than pure Si and Si-FeSi$_2$ counterparts, as depicted in Fig. 22. The nanocomposite displays a stable reversible capacity of ~ 1002 mAh g$^{-1}$ even after 50 cycles, with a coulombic efficiency reaching ~ 99.8%. Notably, the irreversible capacity loss of the Si-FeSi$_2$/EG anode reduces drastically after subsequent cycles, showcasing only a 0.2% loss by the 50th cycle. This enhanced cyclic performance is attributed to reduced silicon crystal size and the highly elastic nature of the Si-FeSi$_2$/EG nanocomposite facilitated by the encapsulation of Si-FeSi$_2$ within the exfoliated graphite matrix.

However, Shin et al. [239] studied the potential of multivalent metals such as calcium, magnesium, and aluminium as promising candidates for rechargeable battery anodes due to their high theoretical capacity, enabled by multiple electron transfer per redox center. Calcium stands out with its low electrochemical potential of − 2.87 V relative to the standard hydrogen electrode, coupled with being the fifth most abundant element in the earth's crust. Despite these advantages, it is imperative to comprehensively understand calcium's mechanical properties to address potential degradation and failure mechanisms before practical implementation. To this end, the authors conducted mechanical testing on calcium at both nano- and macro-scales using nanoindentation and bulk compression testing techniques. Nanoindentation tests revealed an elastic modulus ranging from 25.2 to 21.7 GPa and a hardness ranging from 0.88 to 0.46 GPa across indentation depths ranging from 0.25 to 10 µm, as illustrated in Fig. 23a and b, respectively.

Nevertheless, the bulk compression tests yielded a yield strength of 107 ± 4.6 MPa (average ± standard deviation), as shown in Fig. 24. Notably, these tests indicated minimal sensitivity of calcium's mechanical properties to strain rate or "size effects," which differs from previous studies on alkali metal anodes, likely due to calcium's relatively high melting point compared to alkali metals. Table 2 compares the merits and demerits of the various characterization techniques used in the assessment of the physiochemical, mechanical, and electrochemical properties of electrochemical energy storage devices (including supercapacitors, lithium-ion, and lithium-sulfur batteries).

## Applications of diatomaceous earth bio-templated electrode material in energy storage

Energy conversion and storage systems play crucial roles in addressing the intermittent of sustainable energy sources [108, 240, 241]. However, the materials used in these supercapacitors or battery systems often involve complex chemical processes, leading to inevitable environmental pollution and high energy consumption [47, 127, 179, 242]. With their unique architecture, adsorption capability, and rich active sites, natural mineral resources have attracted significant attention for their remarkable

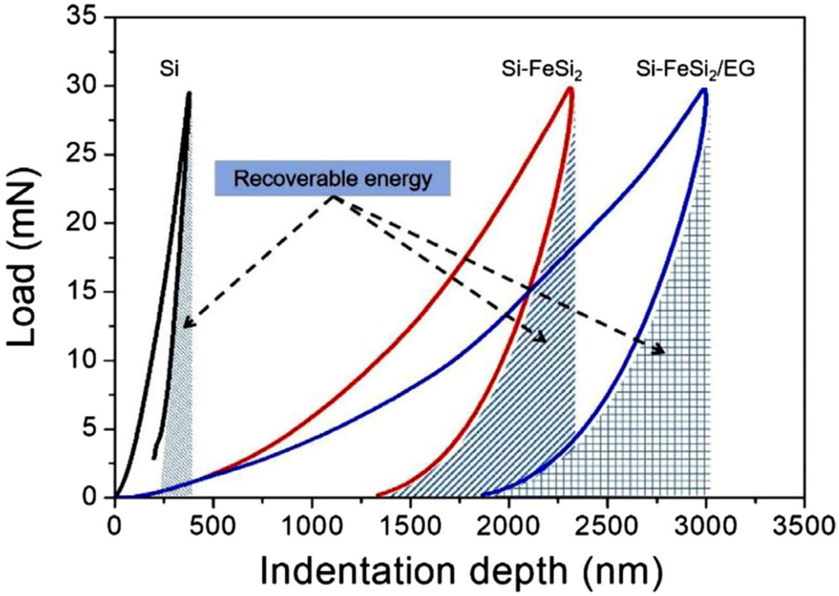

**Fig. 22** Nano-indentation test results showing load-indentation displacement curves. Source: [148]

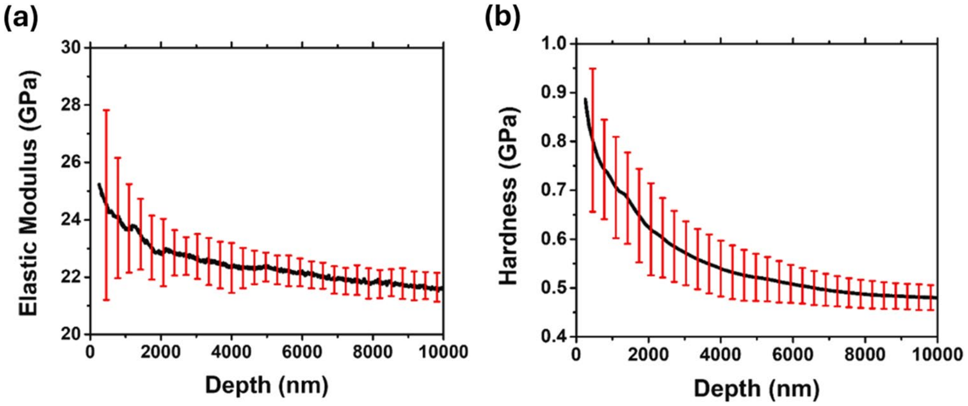

**Fig. 23** **a** Results of nanoindentation tests showing the elastic modulus of Ca metal at room temperature as a function of depth. Tests were conducted at a constant loading rate of 0.05 1/s to a depth of 10 µm. The black line represents the average of seven individual tests, with error bars (in red) indicating one standard deviation from the average. **b** Nanoindentation hardness measurements of calcium metal at room temperature. The black line represents the average of seven individual tests, with error bars (in red) indicating one standard deviation from the average. Source: [239]

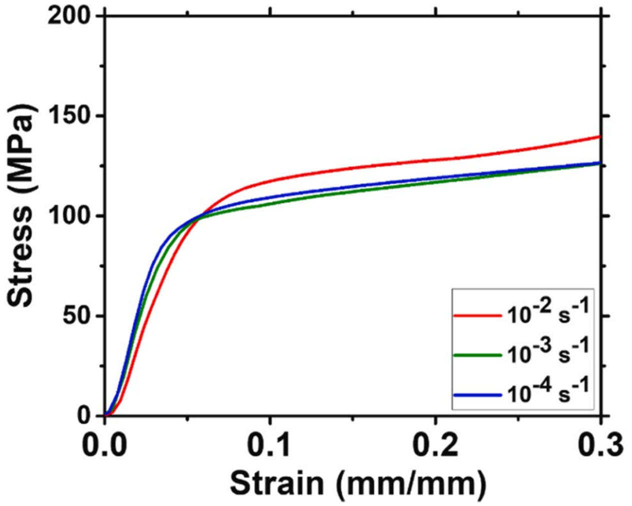

**Fig. 24** Engineering stress–strain curves of solid calcium metal compressed at room temperature. Each strain rate was tested three times, and the plot shows the average for each rate. The colors represent different rates: red for $10^{-2}$ 1/s, green for $10^{-3}$ 1/s, and blue for $10^{-4}$ 1/s. Source: [239]

advancements [50]. In recent developments, mineral compounds with 1D structures (such as halloysites, attapulgites, and sepiolite), 2D structures (including montmorillonite, vermiculite, and molybdenite), and 3D structures (like diatomite and pyrites) have found applications in various fields. Specifically focusing on their roles in energy storage, these minerals have been extensively utilized in electrodes, separators, electrolytes, and metal protection in lithium-ion batteries, lithium-sulfur batteries, solid-state batteries, and more [44, 50, 185].

Nonetheless, recognizing the limitations of basic minerals in fulfilling the requirements of energy storage systems, given their inadequate conductivity and restricted active substances. Conversely, their hierarchical and porous nature occasionally positions them as promising template materials. Consequently, diverse modification strategies have been employed, encompassing phase evolution (transitioning from silicate mineral to Si), integration with carbon/polymer, and tailoring surface traits [35]. A critical analysis of template-assisted growth using diatomaceous earth reveals a significant impact on energy storage performance. With its intricate and hierarchical porous structure, diatomaceous earth is an ideal scaffold for growing active materials such as metal oxides or conducting polymers. The porous architecture allows for enhanced surface area, promoting better interaction between the electrolyte and electrode materials and improving ion diffusion rates. However, the challenge lies in ensuring uniform material deposition across the intricate surface of diatomaceous earth. Uneven growth can result in reduced conductivity and hindered charge transfer.

Additionally, while the template-assisted approach provides structural stability, the inherent insulating nature of diatomaceous earth necessitates further modifications, such as doping with conductive materials or integration with carbon-based materials, to enhance electrical conductivity. Nevertheless, when effectively optimized, using diatomaceous earth as a template can significantly improve the electrochemical performance of energy storage systems, particularly in terms of cycle stability, rate capability, and overall energy density. The morphological modification of electrode materials using natural minerals, specifically diatomaceous earth [35, 52, 74, 98], as a precursor and a template material

**Table 2** Compares the merits and demerits of the various characterization techniques of electrochemical energy storage devices to access the physiochemical, mechanical, and electrochemical properties

| Characterization technique | Uses | Merits | Demerits |
|---|---|---|---|
| X-ray diffraction (XRD) | Crystal structure and material composition | Operating conditions do not require a vacuum. Sample preparation is either not needed or minimal | Examination of amorphous materials is impossible, and no depth profile information can be obtained |
| Fourier-transform infrared spectroscopy (FT-IR) | Energy levels of molecules and molecular interactions | Improved wavenumber accuracy and flexible range. Reduced time consumption. Increased sensitivity and brightness. Enhanced frequency resolution | Compound detection is typically influenced by chemical interference, water vapor, and pathlength |
| Raman spectroscopy | Chemical structure, phase and polymorph, crystallinity, and molecular interactions | It can be employed to detect vibrational modes that are not active in the IR. It can be utilized to distinguish smaller particles with a shorter wavelength. Materials with higher chemical specificity can be differentiated due to the narrower Raman bands | Due to its weak effect, metals or alloys cannot be analyzed using Raman spectroscopy |
| BET analysis | Specific surface area estimation | The adsorbed gas volume is predicted as a function of the gas partial pressure | Its usage is limited to a narrow range of partial pressures |
| BJH analysis | Pore area and specific pore volume estimation | The non-destructive test allows data on surface area, pore volumes, and distribution to be obtained in a single experiment | Closed pores cannot be accessed through the material surface, and this technique only applies to physical adsorption |
| Scanning electron microscopy (SEM) | Surface morphology | Different detectors can be used to obtain 3D topographical images and versatile data of the sample | Operating it is very expensive |
| Transmission electron microscopy (TEM) | Capturing the interior structure of a sample using a broad electron beam revealing its morphology, chemical composition, and crystal structure | TEM provides improved spatial resolution and additional analytical measurements | The experiment needs a highly vacuumed environment, thin sample cutting, and takes more time to be conducted |
| Energy dispersive X-ray spectroscopy (EDX) | Chemical or elemental composition | SEM/EDS provides information about the surface structure of various materials, and their elemental composition can also be measured | The SEM–EDS method's limitations in examining food and textile samples are mainly linked to the inability to analyze wet samples |
| Electron backscattered diffraction (EBSD) | Crystallographic orientations, misorientations, texture trends, and grain boundary types on a micron scale | Can provide information on several different planes of symmetry simultaneously, allowing for an adequate understanding of a specific region of the crystal structure | The specimen surface needs to be polished extremely well, ensuring it is free from contaminants, debris, or damage |
| Cyclic voltammetry analysis (CV) | Capacitance of the working electrode | Distinguish between EDLC, pseudo capacitors, and battery-grade materials. Calculate capacitance, capacity, energy, and power density | Thermodynamic aspects are entirely overlooked |
| Galvanostatic charge and discharge cycles (GCD) | Capacitance, cyclic stability | Calculation of capacitance, capacity, energy, and power density is performed. EDLC, pseudo-capacitors, and battery-grade materials are differentiated | Provide a rectangular shape for all electrode materials of EDLCs |

**Table 2** (continued)

| Characterization technique | Uses | Merits | Demerits |
|---|---|---|---|
| Electrochemical impedance spectroscopy (EIS) | Impedance or resistance in the working electrode and electrolyte | High resistance materials (coatings) can be effectively used. Time-dependent data is accessible and nondestructive, quantitative data is obtainable | Quantifying involves complex data analysis, and it can be costly. Evaluation is generally carried out at lower voltages |
| Tensile testing (single layered and multilayered compounds) | Mechanical properties (ultimate tensile strength, yield strength, toughness, etc.) | Different thicknesses can be examined to study the effects of size. The determination of Young's modulus and fracture strength is made easy. Stress states relevant to flexible electronics are considered. Fabrication is easy, and there is no third-body interaction. Adhesion properties can be measured | Making a single-layer sample is challenging and time-consuming. The experimentation takes time and directly provides information about the failure mode |
| Nano indentation or ball indentation | Tensile strength, hardness, and fracture toughness of individual phases | Ease of fabrication of sample. It is quick, automated, and involves many points per sample. We usually use thin samples in the experiment. When we attach a nanoindenter to an SEM (scanning electron microscope) in an in situ or operando mode, we can observe the contact zone in real time during the nanoindentation cycle | Doing nanoindentation in real-time is only possible when it's done in in-situ or operando |

for energy storage applications in supercapacitors or batteries are discussed in the following sections.

## Supercapacitors

In present-day research, the attention of scientists is drawn to supercapacitors [243] due to their advancements over batteries [162, 170]. Unlike batteries that suddenly decrease efficiency during fast charging cycles, supercapacitors offer substantial efficiency improvements [70, 118]. Batteries, characterized by a short lifetime, act as intermediaries between supercapacitors and fuel cells, as depicted in the Ragone plot (Fig. 25).

Supercapacitors offer high capacitance, power density, and durability and can operate across a wide temperature range [13, 205, 245, 246]. Their performance is enhanced using electrical double-layer capacitance and pseudo-capacitance [13, 14, 247] rather than the solid dielectric in traditional capacitors [64, 203, 248]. The effectiveness of supercapacitors depends on the materials used for the electrodes, separator, and electrolyte [14]. They typically consist of two electrodes, a separator, and an electrolyte, which ionically connects the electrodes [69, 249]. Two types of electrolytes are used: aqueous (higher ionic conduction, lower voltage) [216] and organic (larger voltage window) [250]. Supercapacitors are categorized by their structure, which includes thin film, flexible, and planar. Electric double-layer capacitors (EDLCs) are commonly used due to their stability. EDLCs use organic electrolytes for higher charge storage, while pseudo-capacitors rely on redox reactions for charge transfer. Materials like activated carbon, CNTs, graphene, and transition metal oxides enhance electrochemical performance and charge storage. Hybrid supercapacitors [251], which combine both EDLC and pseudocapacitive materials, are further divided into asymmetric and symmetric hybrids [252], battery-type hybrids [253], and composite hybrids [57, 251] (e.g., $Fe_3O_4$/graphene, r-GO-f/PANI)) as shown in Fig. 26.

Hybrid supercapacitors balance faradic and non-faradic processes, addressing the limitations of EDLCs and pseudocapacitors. They offer high energy density, cyclic stability, power density, low cost, mechanical strength, and superior performance across a wide temperature range [251]. Widely used in vehicular power sources, recent research focuses on cost-effective, environmentally compatible transition metal oxides like Fe2O3 and MnO2 for their high specific capacitance [65, 200]. Porous templates like diatomite (DE) have advanced electrode synthesis [35]. Electrochemical techniques such as cyclic voltammetry (CV), electrochemical impedance spectroscopy (EIS), and galvanostatic charge–discharge (GCD) testing are used to evaluate their performance [65]. In a groundbreaking study, Li et al. [92] have demonstrated a controlled synthesis of tunable

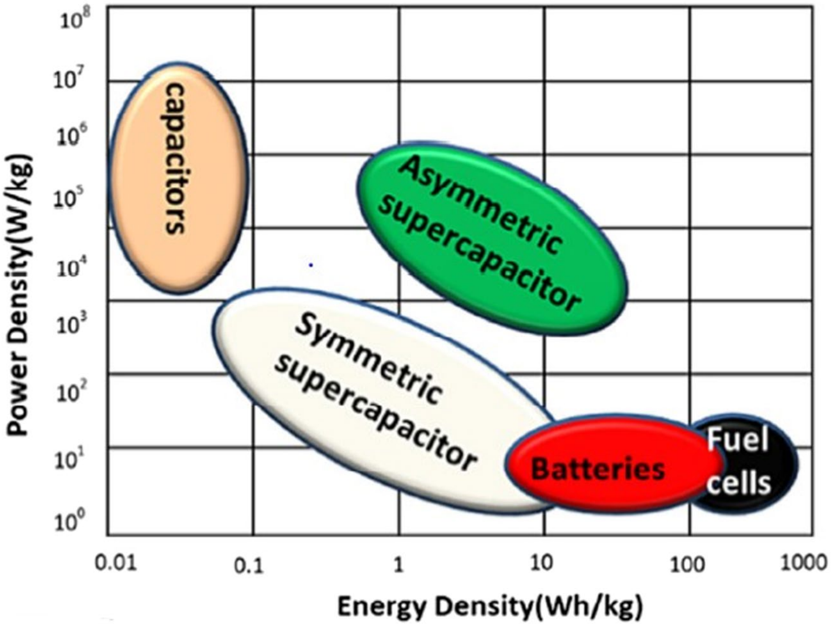

**Fig. 25** Comparison of energy density versus power density for various energy storage devices. Source: [244]

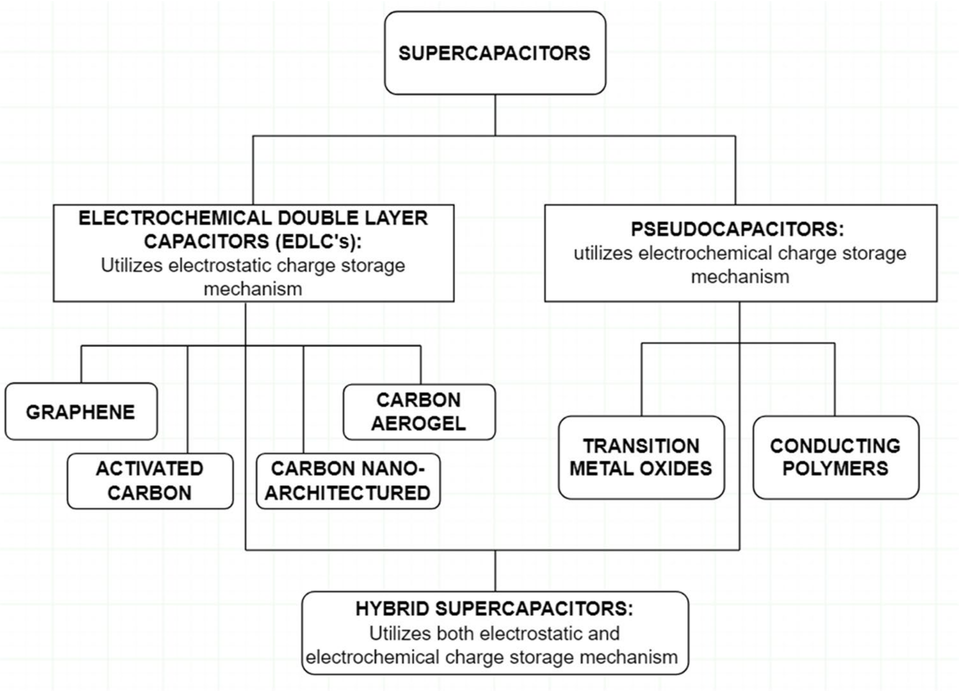

**Fig. 26** Categories of supercapacitors based on their charge storage method

Mn-iron-oxide (Mn-FeOx) hybrids, leveraging the exclusive three-dimensional (3D) porous structure derived from diatoms to enhance the performance of supercapacitors. Employing a meticulous two-step hydrothermal method, the researchers successfully facilitated the transition from $MnO_2$ to FeOOH on diatomite, resulting in replicas characterized by a 3D diatom morphology through a subsequent etching process. The MnFeOx-0 diatom replica, excluding the transition, showcased $MnO_2$ nanosheets and exhibited remarkable electrochemical performance. Notably, it established a high specific capacitance of 228.6 F/g at 1 A/g, coupled with commendable rate capability (capacitance retention of 74.6% at higher current density of 10 A/g), high coulombic efficiency (approximately 93.1% at 10 A/g), and consistent cycling performance resulting in a capacitance retention of 94.3% after 4000 cycles. Conversely, the $MnFeO_x$ -110 replica, featuring FeOOH nanorods, demonstrated a specific capacitance of 224.6 F/g at 1 A/g, coupled with a high coulombic efficiency of about 80% at 10 A/g and steady cycling performance with 92.5% capacity retention after 4000 cycles. Building upon these advancements, an asymmetric supercapacitor was meticulously built, with $MnO_2$ nanosheets serving as the positive electrode and FeOOH nanorods as the negative electrode. This configuration yielded a wide voltage of 2 V, delivering an impressively high energy density of 51.5 Wh/kg and a notable power density of 9.1 kW/kg. The cumulative outstanding energy storage properties exhibited by the two replicas open new opportunities for the balanced design of diatom morphology samples, showcasing the voltage for the development of high-presentation supercapacitors.

In contrast, Guo et al. [101] present an innovative method for creating a sophisticated three-dimensional (3D) composite for supercapacitors. They utilize hollow diatom silica structures combined with interconnected coatings of $TiO_2$ nanospheres and $MnO_2$ mesoporous nanosheets (diatomite@$TiO_2$@$MnO_2$). The coating process involves hydrolysis and a metathetic reaction of the $TiF_4$ precursor, followed by a reaction with $KMnO_4$, enabling the coating of both the internal and external surfaces of the diatom hollow structure with $TiO_2$ and $MnO_2$ layers. The results demonstrate that incorporating the anatase $TiO_2$ film onto the 3D diatomite@$TiO_2$@$MnO_2$ electrodes significantly enhances specific capacitance, resistance, and rate capability, as shown in Fig. 27.

This underscores the pivotal role of an additional conductive layer on the diatom surface. Furthermore, owing to its unique 3D structure, the diatomite@$TiO_2$@$MnO_2$ electrode exhibits prolonged cyclic stability, retaining 94.1% capacity after 2000 cycles, along with a great coulombic efficiency maintaining 98.2–99.6% over 2000 cycles as shown in Fig. 28. These findings underscore the superior supercapacitor performance of the diatomite@$TiO_2$@$MnO_2$ electrodes, as shown in Figs. 27 and 28, prepared using less-costly natural diatomite material and a scalable, cost-effective process. The study confirms their obvious voltage for applications in energy storage and conversion.

Huang et al. [74] also initiated a study emphasizing the environmental importance of repurposing biomass waste for ecological improvement and addressing the ongoing energy crisis. Specifically, waste diatomite laden with adsorbed yeast protein, a byproduct of beer filtration, was effectively transformed into nitrogen-doped porous carbon (NPC) through high-temperature thermal treatment. The resulting NPC inherits the intricate three-dimensional hierarchical structure of diatomite, featuring a distinctive rich-pore composition encompassing micro/meso/macropores. This composition proves advantageous for enhancing exposure to electrocatalytic sites and facilitating ion transfer and diffusion. The controllably nitrogen-doped NPC compounds were employed for the oxygen reduction reaction (ORR) and as a component in a supercapacitor. In ORR applications, NPC-2 exhibited a noteworthy half-wave voltage of 0.801 V, comparable to the commercially available Pt/C (0.812 V) in alkaline media. NPC-2 demonstrated excellent methanol tolerance and long-term stability during the ORR. Moreover, when employed as an electrode material in a symmetric

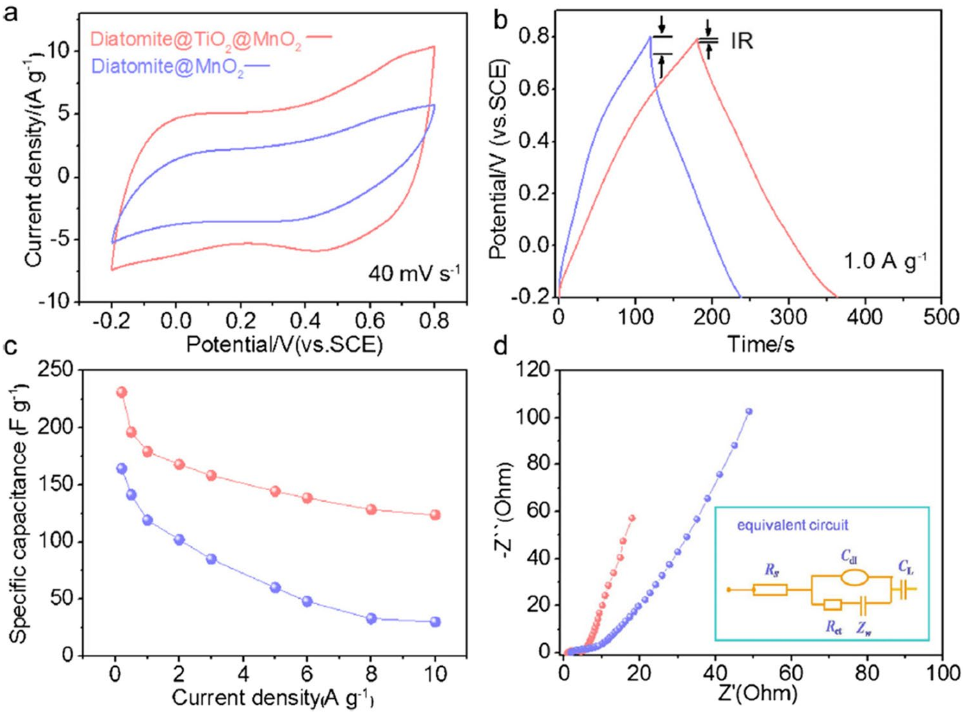

**Fig. 27** Comparison of electrochemical properties between diatomite@$TiO_2$@$MnO_2$ (red line) and diatomite@$MnO_2$ (blue line) electrodes: **a** Cyclic voltammograms at 40 mV/s. **b** Charge–discharge curves at 1 A/g. **c** Specific capacitance ($C_s$) vs. discharge current density. **d** Initial electrochemical impedance spectra. The inset illustrates the equivalent circuit. Note: $C_s$ can be calculated using the formula $C = I\mathrm{d}t/m\mathrm{d}V$, where $I$ is the discharge current, dt is the discharge time, dV is the voltage range, and $m$ is the mass of the active material. Source: [101]

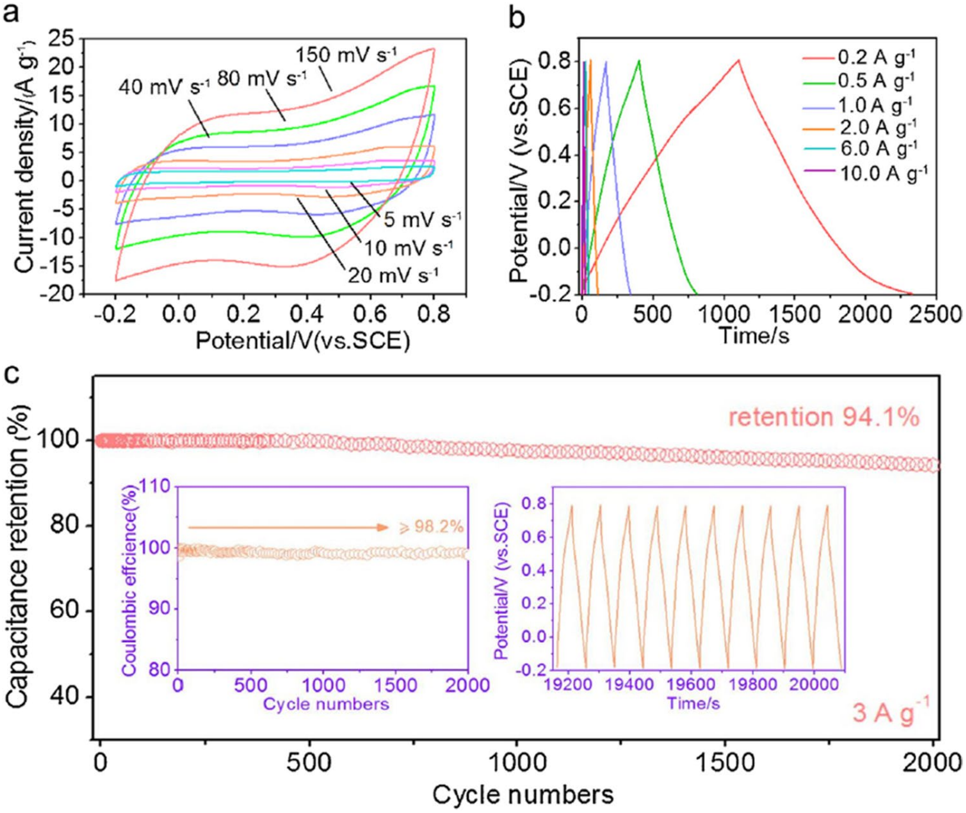

**Fig. 28** Cyclic voltammograms display the behavior of the diatomite@$TiO_2$@$MnO_2$ electrode at various scan rates. Charge–discharge curves illustrate its performance at different current densities. The cycling performance at a 3 A/g current density is depicted, with insets showing coulombic efficiency and the GCD curves of the last 10 cycles. Source: [101]

supercapacitor, NPC-2 displayed an impressive specific capacitance of 151.5 F/g at a current density of 1 A/g, with notable capacitance retention of 90.5% after 10,000 cycles. The symmetric supercapacitor based on NPC-2 delivered an energy density of 13.47 Wh/kg at a power density of 400 W/kg. This research underscores the environmental significance of repurposing waste diatomite into metal-free ORR catalysts and electrode materials for advancements in energy conversion and storage technologies.

In the research conducted by Hu et al. [254], natural and readily available biomass diatomite serves as a porous template material for the in situ development of a graphene layer (G). Subsequently, carbon nanotube (CNT) arrays are cultivated on the graphene surface. The resulting seamlessly anchored 1D CNT's arrays, combined with 3D interconnected graphene networks, form a conductive hierarchical framework that significantly enhances electric conductivity. Additionally, the expanded effective surface area of the CNTs/G/diatomite composite contributes to increased active material loading and facilitates electrolyte infiltration. Because of these structural features, the $MnO_2$@CNTs/G/diatomite hybrid demonstrates an impressive specific capacitance of 264.0 F/g resulting from the presence of $MnO_2$ electrode with a capacitance value of approximately 880.0 F/g. This hybrid material exhibits commendable rate capability and exceptional cyclic stability. Furthermore, an asymmetric supercapacitor, assembled using $MnO_2$@CNTs/G/diatomite and microwave-exfoliated graphite oxide, attains the highest energy density of 64.3 Wh/kg and an impressive power density of 19.8 kW/kg, respectively.

However, Xin et al. [45] introduced an innovative method for fabricating hierarchically porous NiO-modified diatomite structures using a one-pot hydrothermal method. These structures feature a moss-like arrangement composed of NiO nanofiber arrays. The electrochemical properties of the resulting NiO-modified diatomite materials were thoroughly investigated through cyclic voltammograms, electrochemical impedance spectroscopy, and galvanostatic charge/discharge tests in a 1 M KOH electrolytic solution. The electrochemical findings from this study reveal that the distinct NiO-modified diatomite structures exhibit a specific capacitance value of 218.7 F/g, coupled with outstanding cyclic stability of capacitance retention of 90.61% after 1000 cycles. This remarkable capacitive performance suggests that these cost-effective NiO-modified diatomite structures hold significant promise as electrode materials in developing an extraordinary supercapacitor device.

In a different study, Zhang et al. [46] employed a one-pot hydrothermal method to create hierarchical and porous $MnO_2$-modified diatomite structures. The morphology and structure were carefully examined using focus ion beam scanning electron microscopy (FIB/SEM) and X-ray diffraction spectroscopy (XRD). The results reveal the growth of vertically aligned Birnessite-type $MnO_2$ nanosheets on purified diatomite, forming a complex hierarchical architecture. Electrochemical properties were thoroughly explained through cyclic voltammograms, galvanostatic charge/discharge tests, and electrochemical impedance spectroscopy in a 1 M $Na_2SO_4$ electrolyte. The findings highlight the $MnO_2$-modified diatomite electrode's high reversibility and commendable rate abilities, demonstrating a specific capacitance of 202.6 F/g for $MnO_2$-modified diatomite and 297.8 F/g for $MnO_2$ nanostructures after etching the diatomite. With an impressive capacitance retention of 95.92% over 5000 cycles, the cost-effective $MnO_2$-modified diatomite structure shows potential as a promising electrode material for supercapacitors, as depicted in Fig. 29.

## *Lithium*-ion batteries

Addressing the contemporary limitation of advancing efficient energy generation and storage systems is crucial in modern society [168]. Lithium-ion batteries [255] have emerged as the primary power source for portable electronics, enjoying widespread adoption in recent years due to their efficiency, extended lifespan, and minimal environmental impact [256]. During discharge, lithium ions are transported from an electrolyte from the cathode to the anode and vice versa during charging, forming the core of the lithium-ion battery's electrochemistry [52]. The anode and cathode are usually parted by a micro-permeable separating material facilitating the movement of lithium ions. The electrochemical characteristics of lithium-ion batteries are severely influenced by the electrode material selection, emphasizing the importance of exploring electrodes with high lithium storage capacity and prolonged cycling stability. Cycling stability, indicative of a battery's ability to maintain performance through multiple charge and discharge cycles, is a critical consideration [257]. Many lithium-ion batteries face challenges related to limited cycling stability, and selecting appropriate materials is crucial in overcoming this hurdle [52]. Another pivotal parameter defining lithium-ion battery performance is rate capacity, which reflects the battery's capability to efficiently receive and deliver charges at high charging or discharging rates. Rate capacity determines the speed at which lithium-ion batteries store electrical energy, and the electrode material significantly impacts this aspect [258]. Additionally, the operational conditions, including temperature, cycle life, and power output, play a crucial role in determining the efficiency of lithium-ion batteries. Successful advancements in addressing these parameters are essential for the continued evolution of energy storage and conversion technologies [68].

Wang et al. [44] utilized diatomite as a critical raw material for synthesizing several porous Si/C composite materials. The synthesis process involved low-temperature magnesiothermic reduction, carbonization of phenolic, and resin impregnation. The resulting Si/C composites feature porous

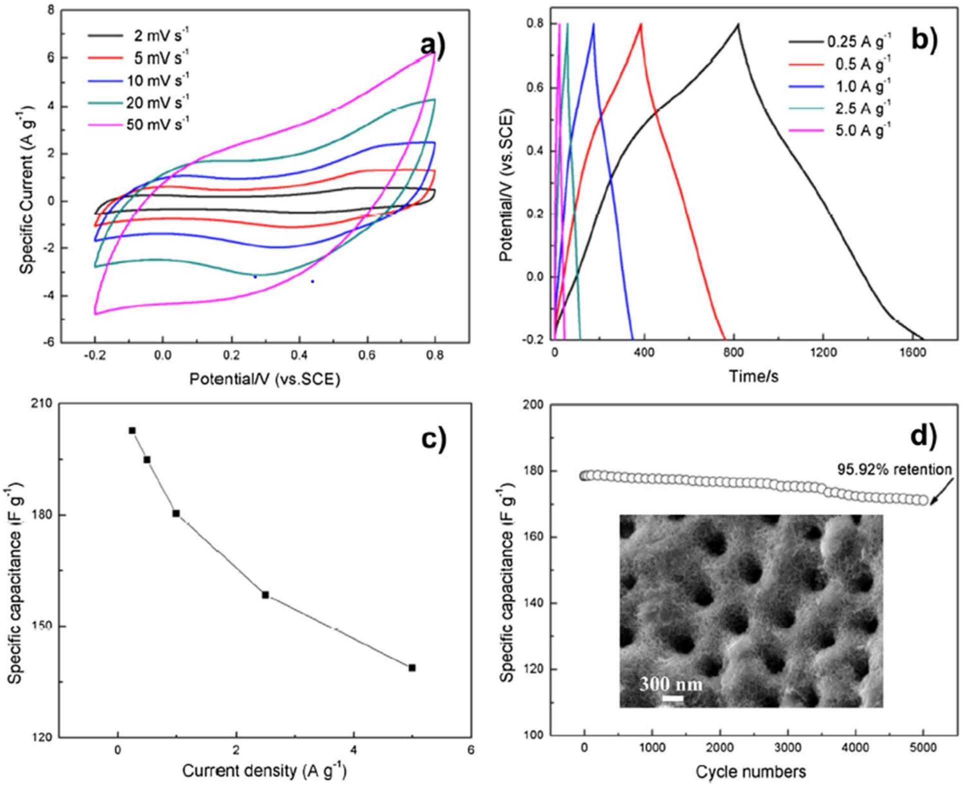

**Fig. 29** **a** Cyclic voltammograms of $MnO_2$-modified diatomite composite at varying scan rates (2, 5, 10, 20, and 50 mV/s) in a 1 M $Na_2SO_4$ aqueous electrolyte; **b** charge–discharge curves of $MnO_2$-diatomite electrodes under different current densities (0.5, 1, 2, 5, and 10 mA/cm$^2$); **c** specific capacitance of $MnO_2$-diatomite measured at various current densities; **d** cycling performance of $MnO_2$-diatomite at 1 A/g current density with SEM image (inset) of the electrode post 5000 electrochemical cycles. Source: [46]

Si layered with a 15 nm copious amorphous carbon layer, as shown in Figs. 30 and 31.

Various compositions of Si and C were investigated in porous Si/C composites to assess their suitability as anode materials for Li-ion batteries. Among the tested configurations, the porous Si/C composite with 33% carbon content showed the highest reversible capacity, reaching approximately 1628 mAh/g in the initial cycle. This composite exhibited outstanding capacity retention in subsequent cycles and demonstrated excellent rate performance, particularly at high current densities such as 1 and 2 A/g, as illustrated in Fig. 32a, b. The electrochemical performance of these composites was adjustable by varying the proportions of porous Si and carbon precursors during the preparation process. The outcomes indicate that the inherent pore structures of Si and C contribute positively to the electrochemical performance. Additionally, the clay mineral diatomite is identified as a promising raw material for Si/C composites intended for use in lithium-ion batteries.

Wang et al. [259] successfully developed a dual-carbon-enhanced Si-based composite (Si/C/G) by utilizing diatomite mineral as a silicon raw material. This mineral is abundant, cost-effective, and environmentally friendly. The preparation processes for this composite are straightforward, non-toxic, and easily scalable. In electrochemical tests as a lithium-ion battery (LIB) anode material, the Si/C/G composite shows markedly enhanced Li-storage properties, outperforming both pristine Si material and single-carbon-modified composites. Notably, the Si/C/G composite exhibits superior high-rate capabilities and

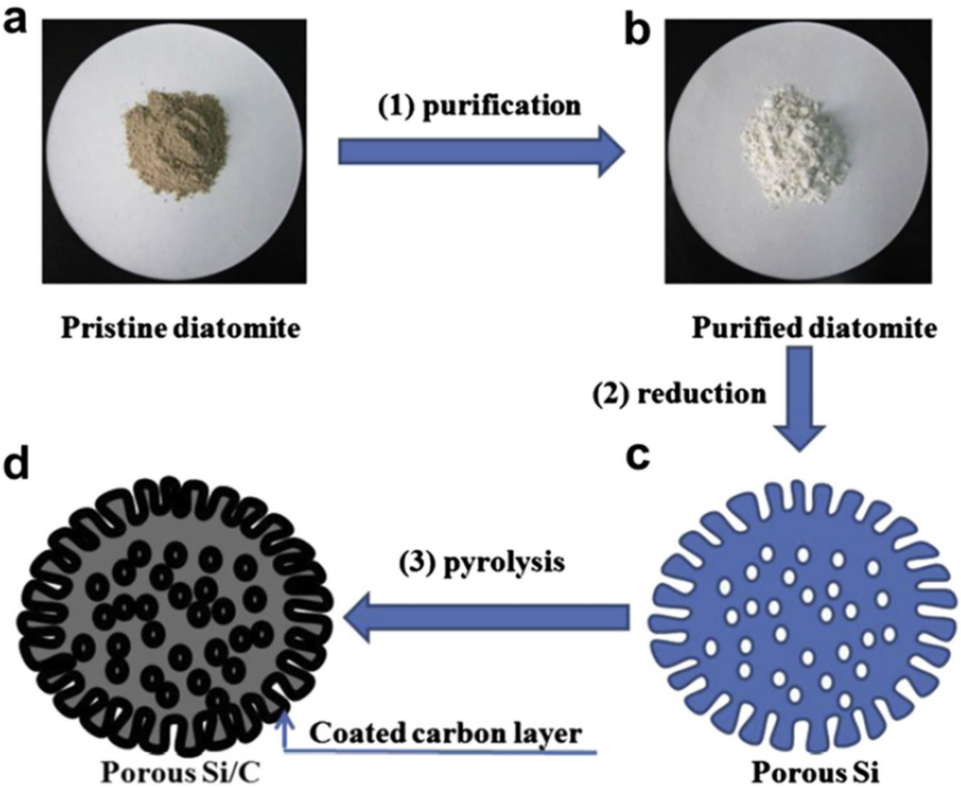

**Fig. 30** Fabrication of porous Si/C composite: (1) purify diatomite via calcination and acid treatment; (2) form porous Si electrode by reducing with Mg; (3) produce Si/C composites by pyrolyzing phenolic resin. Source: [44]

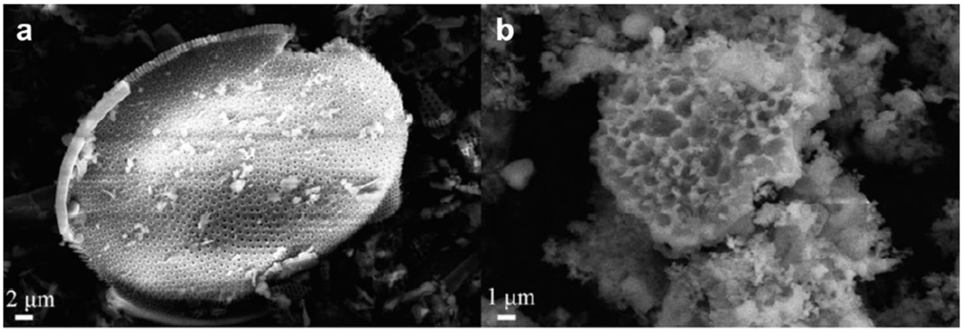

**Fig. 31** FE-SEM of **a** purified diatomite and **b** porous Si. Source: [44]

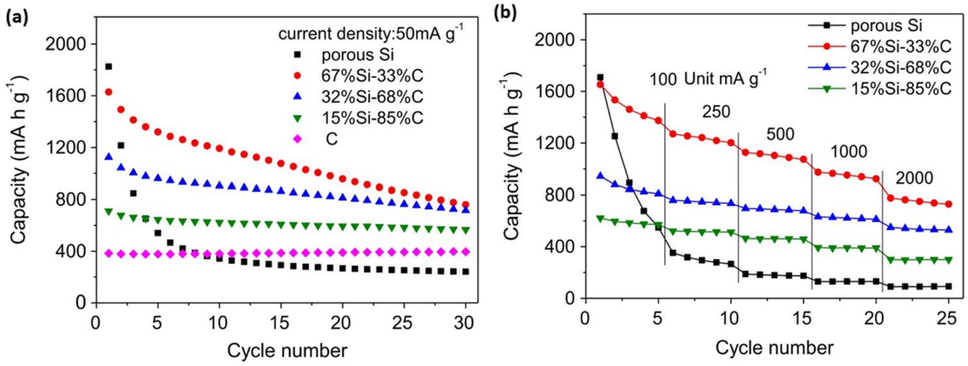

**Fig. 32** The electrochemical behavior of porous Si and porous Si/C composites with varying ratios: **a** cycling performance at 50 mA/g current density and **b** rate stability at different current densities. Source: [44]

excellent cycle stability. Even at an ultrahigh current density of 5 A/g, it maintains a high specific capacity value of approximately 470 mAh/g. Moreover, at a lower current density of 0.1 A/g, it achieves a substantial capacity of 938 mAh/g with outstanding capacity retention over 300 cycles. The notable Li-storage properties of the Si/C/G composite can be ascribed to the co-existence of highly conductive graphite and amorphous carbon within the composite. The presence of highly conductive graphite enhances the electrical conductivity of the composite, while amorphous carbon serves as an adhesive, connecting porous Si particulates and conductive graphite flakes. This connectivity forms a robust and stable conductive network, contributing to the improved characteristics of the Si/C/G composite in lithium-ion batteries.

Also, Li et al. [43] presented silicon oxides (SiO, $SiO_2$, $SiO_x$, etc.) as a novel generation of anode materials for lithium-ion batteries, given their highly high theoretical specific capacity values and cost-effectiveness. Despite these advantages, their progress has been hindered by low conductivity and sub-optimal electrochemical performance. To address these challenges, this study presents a novel approach involving designing and fabricating a porous $SiO_2$ occupied by Al anode. This is achieved through a straightforward yet highly effective melt-self-assembly method, wherein the $SiO_2$ originates from diatomite with a natural porous structure serving as a framework for synthesizing the highly porous electrode material, as depicted in Figs. 33 and 34.

The inclusion of aluminium (Al) in the $SiO_2$ anodes not only contributes to a higher specific capacity value but also induces significantly the overall conduction of the electrode. As anticipated, the $SiO_2$@Al electrode exhibits a noteworthy high capacity of 730 mAh/g, with an impressive capacity retention rate of 95% after 312 cycles. Notably, the rate capability was highly improved, showcasing a capacity value of up to 635 mAh/g at a current density of 800 mA/g, surpassing the performance of the standalone $SiO_2$ electrode, as illustrated in Figs. 35 and 36. These results underscore the viability of $SiO_2$@Al composite electrode as a great-performance and cost-effective material for the next generation of lithium-ion batteries with high specific energy.

## *Lithium*-sulfur batteries

Addressing energy and environmental challenges means improving sustainable and dependable energy storage. Lithium-sulfur (Li–S) batteries, known for their high theoretical capacity of 1675 mAh/g, offer promising energy storage

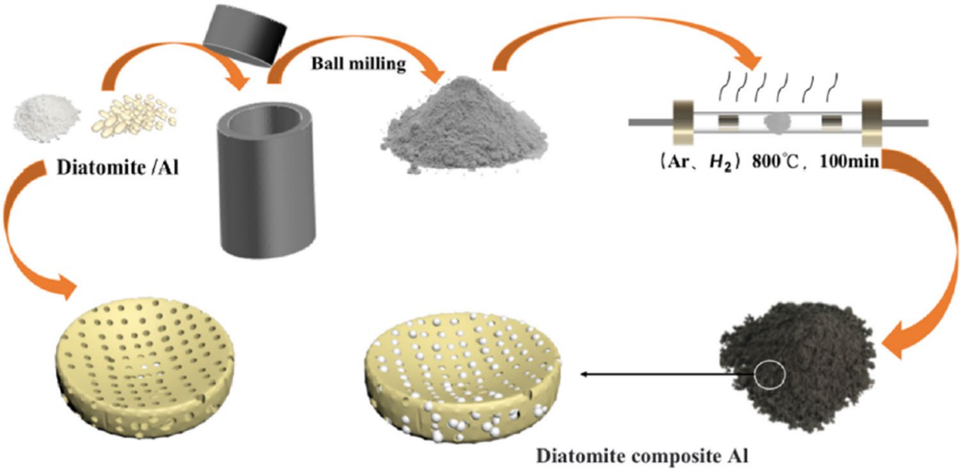

**Fig. 33** Diagram illustrating the preparation process of $SiO_2$@Al electrode material. Source: [43]

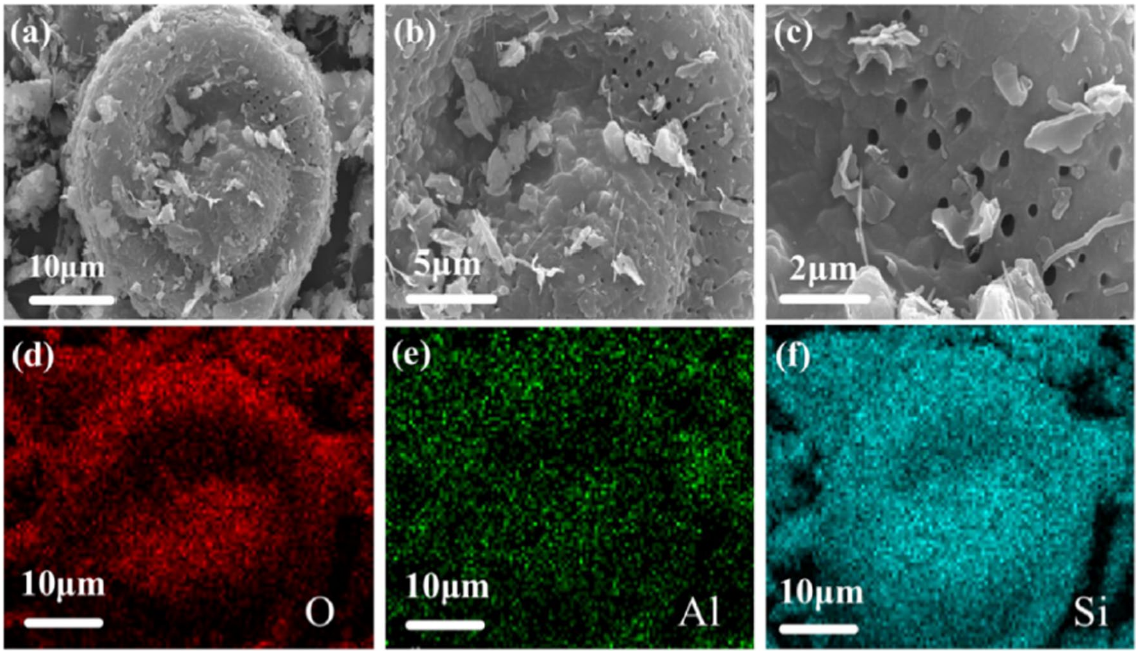

**Fig. 34** **a**–**d** SEM images showing the $SiO_2$@Al electrode at various magnifications; **d**–**f** elemental mapping images of $SiO_2$@Al, depicting O (**d**), Al (**e**), and Si (**f**) elements. Source: [43]

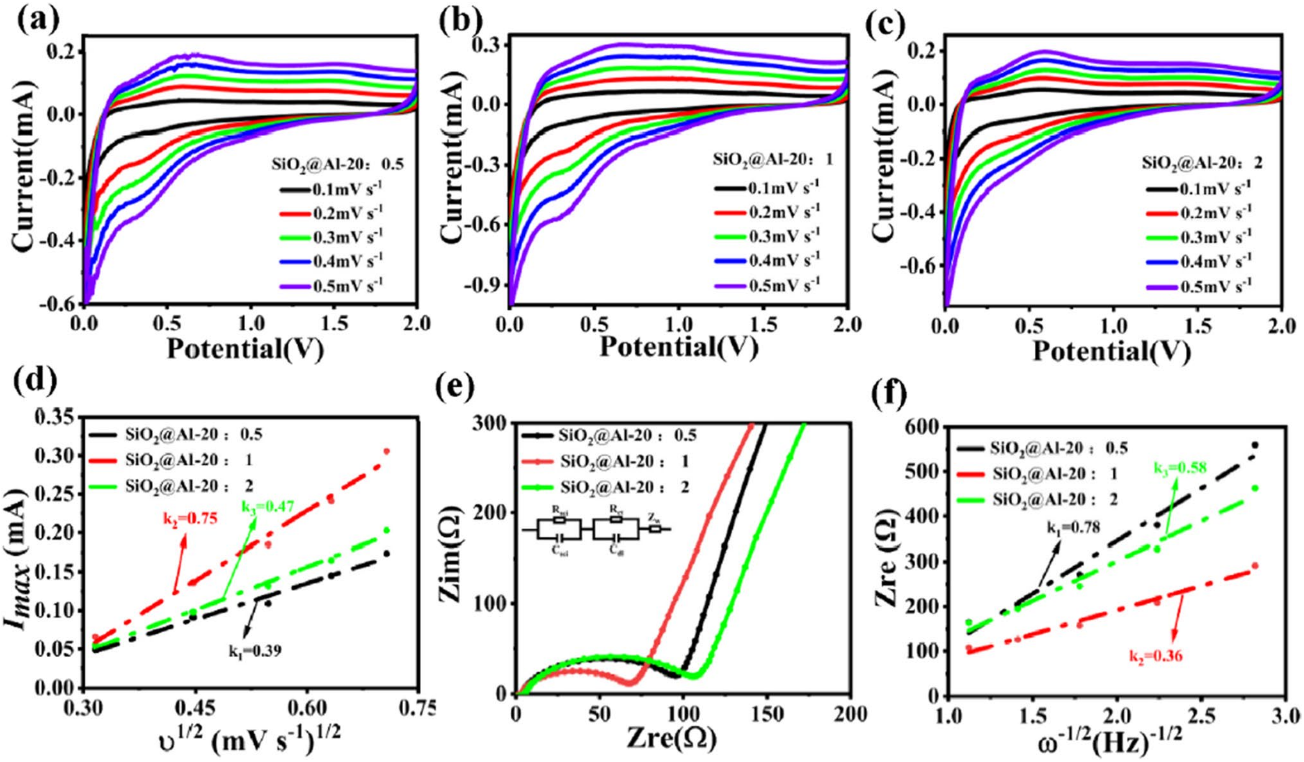

**Fig. 35** Electrochemical performance comparison of various samples: **a**–**c** CV curves of different $SiO_2$@Al electrode material ratios at varying scanning rates. **d** Linear correlation between peak current densities and scanning rates for each sample. **e** EIS spectra of different samples. **f** Linear fit between the real part of impedance ($Z_{re}$) and the negative square root of test frequency ($\omega^{(-1/2)}$). Source: [43]

potential [22, 118, 178, 213]. However, obstacles like the slow reaction kinetics of lithium polysulfide molecules, degradation of lithium anode structure, and the shuttle effect from lithium polysulfide molecules hinder widespread commercialization [73, 82]. The insulating nature of sulfur presents a significant obstacle to efficient sulfur utilization and rapid charge transfer reactions within the electrode matrix. Recently, significant works have been keen to enhancing the conductivity of the sulfur cathode [178]. An effective strategy involves incorporating sulfur into a carbonaceous host, improving the electronic conductivity of the S-cathode [44, 50, 260]. Despite these advancements, challenges related to the lithium polysulfide shuttle effect persist, resulting in considerable volume expansion and low sulfur utilization [82]. A rational approach to tackle this issue is the design of nanostructures to serve as mechanical support for sulfur. Nanosized materials prove beneficial in sustaining the structural reliability of the S-cathode during charging-discharging cycles of the electrode [73, 118]. The current manufacturing of battery components heavily relies on non-renewable resources such as oil, gas, and coal, contributing to increased fossil fuel consumption [95, 261]. An excellent alternative lies in utilizing biomass and bio-polymeric-derived products as substitutes for raw materials. Among various biomass and bio-polymeric options, their unique morphology and three-dimensional interlaced network structures emerge as ideal carbon sources. Biomass and bio-polymeric waste materials are easily accessible, cost-effective, and sustainable carbon resources with high adsorption capacity and conductivity [118, 169, 260]. To mitigate the challenges associated with the lithium polysulfide shuttle effect, a practical solution involves introducing transition metal compounds (TMCs) into the S-cathode. TMCs play a crucial role in absorbing/expediting the redox kinetics of lithium polysulfides in electrode reactions, limiting their dissolution in the battery electrolyte [213].

Gou et al. [111] initiated a study on the growing interest in transition metal chalcogenides due to their intriguing electronic and catalytic properties, making them pivotal for energy generation and storage applications. The controllable and less costly large-scale synthesis of these materials has become a focal point of research. In this context, we present a diatomite-template approach for the generic and scalable production of $VS_2$ and other transition metal sulfides, tailored explicitly for emerging energy generation and storage applications. The conformal development of $VS_2$ over the diatomite template imparts defect-abundant features to the resulting structures. Through a comprehensive experimental investigation complemented by theoretical simulations, we unveil that the enriched active sites and sulfur vacancies in these $VS_2$ architectures positively influence catalytic performance, particularly in electrocatalytic hydrogen evolution reactions. Additionally, we demonstrate that the favorable electrical conductivity and highly exposed sites of $VS_2$ hold significant promise as a sulfur host in the realm of Li–S batteries. This work contributes novel insights into the

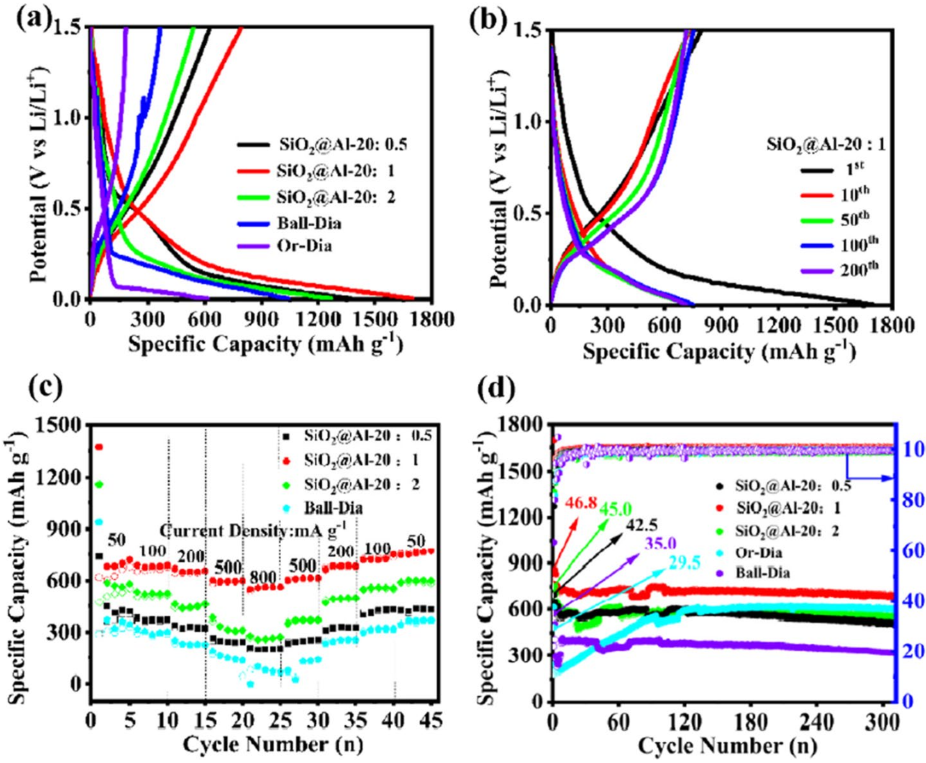

**Fig. 36** Electrochemical performance of different samples: **a** initial charge/discharge curves of various samples at 50 mA/g current density. **b** Cycle performance of $SiO_2$@Al-20:1 electrode material over different cycles. **c** Rate performance comparison among different samples. **d** Cycle performance comparison of various samples at 100 mA/g current density. Source: [43]

templated and customized synthesis of defect-rich sulfides on a scalable platform, offering potential benefits for multifunctional energy applications.

Li et al. [73] also highlighted the considerable potential of lithium-sulfur batteries as leading candidates for high-energy applications. However, the performance of these batteries is significantly compromised by the undesirable shuttling of soluble polysulfides. To address this issue, the authors incorporated diatomite, known for its abundant natural three-dimensional ordered pores, into the cathode to effectively trap polysulfides as shown in Fig. 37. The resulting composite cathode material, abbreviated as S-DM-AB, comprises sulfur (S), diatomite (DM), and acetylene black (AB), prepared through an impregnation method.

The initial discharge capacity of the S-AB cathode is 1167.2 mAh/g, while the S-DM-AB cathode exhibits a little shorter first discharge capacity value of 1160.8 mAh/g. However, notable differences arise in the discharge capacities during subsequent cycles. At the 50th and 100th cycles, the S-DM-AB cathode demonstrates significantly higher capacities, measuring 725.1 mAh/g and 508.8 mAh/g, respectively. In contrast, the S-AB cathode exhibits lower capacities of 294.4 mAh/g at the 50th cycle and 151.2 mAh/g at the 100th cycle, as depicted in Fig. 38b. As a point of comparison, a different composite cathode material (S-AB), incorporating sulfur and acetylene black, was also prepared using the same method. In battery testing, the S-DM-AB composite cathode material exhibited promising results, delivering a discharge capacity value of 531.4 mAh/g after 300 cycles at 2 C, with an impressive capacity retention of 51.6% at room temperature (refer to Fig. 39a). In contrast, the battery with the S-AB composite cathode material only achieved a capacity of 196.9 mAh/g, coupled with a significantly lower capacity retention of 18.6% under an equivalent setting, as shown in Fig. 39a, b.

Prior to cycling, the ohmic resistance (Rs) and charge transfer resistance (Rct) of the S-DM-AB sample were greater than those of the S-AB sample, primarily due to the diatomite's poor conductivity. After undergoing 100 cycles at 0.5 C, both samples experience a slight increase in Rs values, accompanied by a significant decrease in Rct values. This notable reduction in Rct values for both samples is attributed to a diminished interface resistance between sulfur and electrolyte post-100 cycles. After 100 cycles, the S-DM-AB sample exhibits Rs and Rct values of 2.2 Ω and 10.9 Ω, respectively, which are lower than those of the S-AB cathode (2.8 Ω and 14.5 Ω), as illustrated in Fig. 40. This outcome underscores the effectiveness of incorporating diatomite into the cathode as a cost-effective and economical strategy for enhancing the lifespan of lithium-sulfur batteries.

In addressing the issue of the "shuttle" effect, which results from the dissolution of lithium polysulfides, Li et al. [110] have fabricated an innovative separator based on nepenthes-like N-doped hierarchical graphene (NHG), serving as an efficient polysulfide scavenger for Li–S

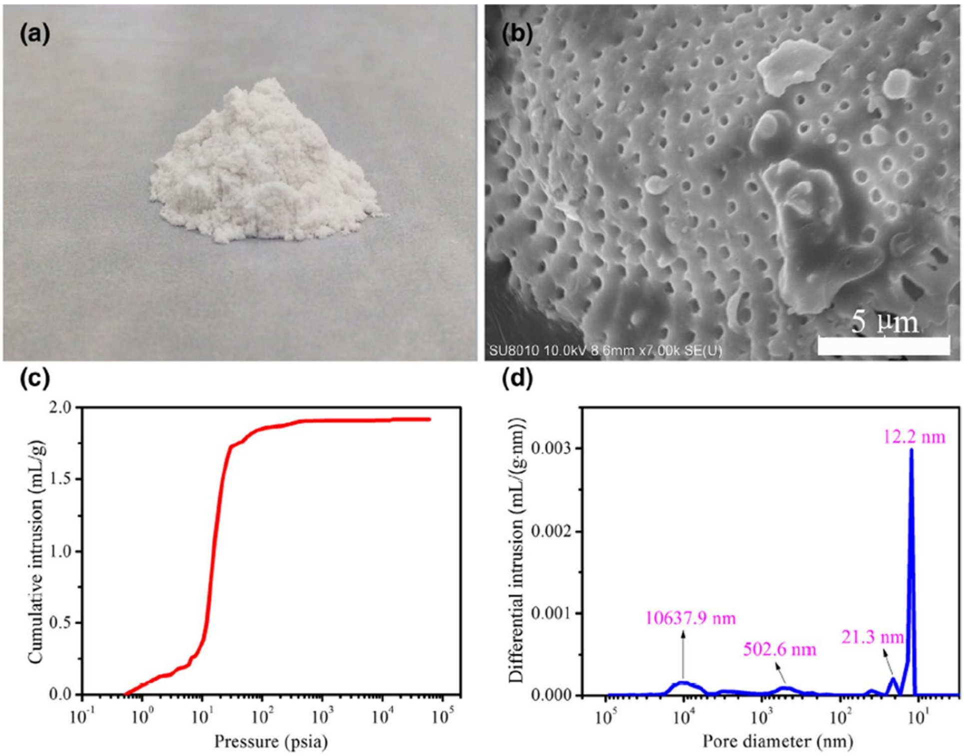

**Fig. 37** **a** Picture of diatomite powder under an optical microscope, **b** scanning electron microscope (SEM) image showing a diatomite particle, **c** graph illustrating cumulative mercury intrusion into diatomite powder, and **d** diagram depicting the pore size distribution of diatomite powder. Source: [73]

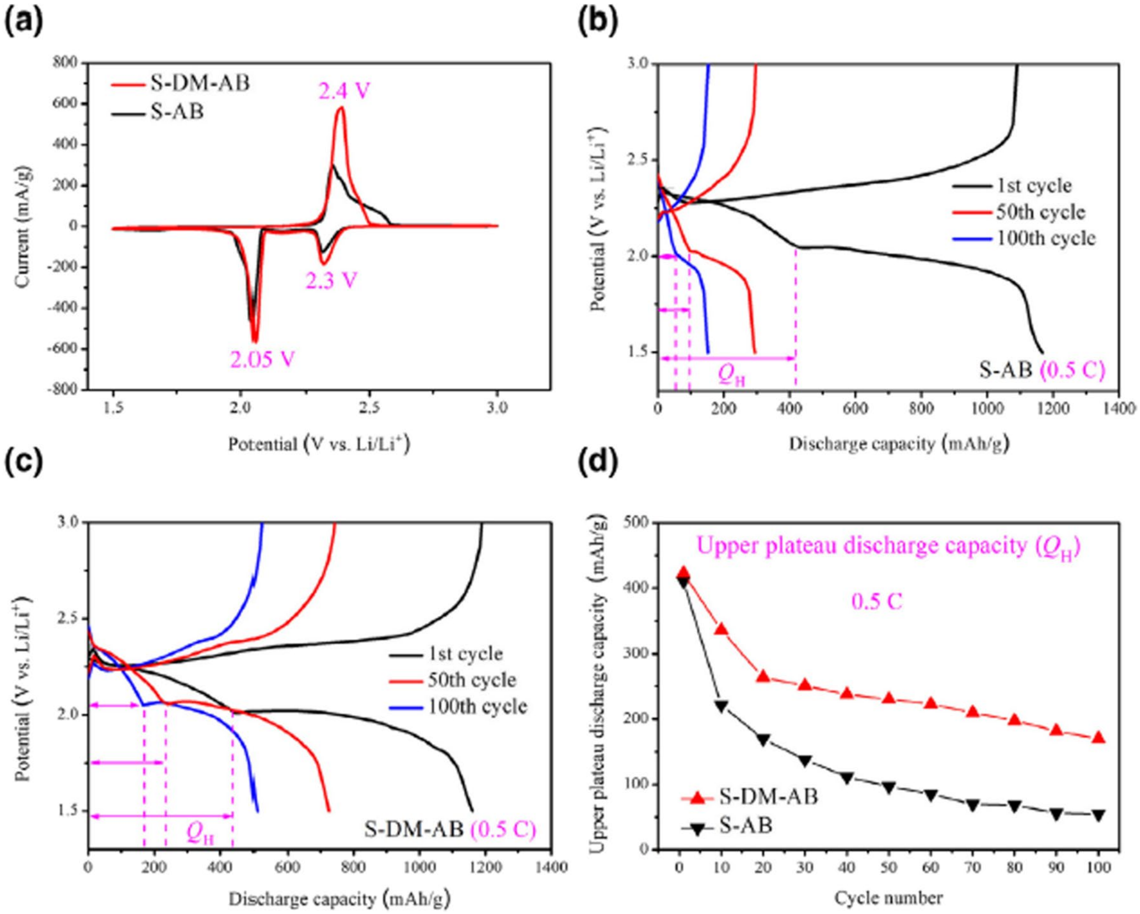

**Fig. 38** **a** CV curves at a scan rate of 0.05 mV/s for S-AB and S-DM-AB cathodes. **b** Voltage plateaus at the 1st, 50th, and 100th cycles for S-AB at 0.5 C. **c** Voltage plateaus at the 1st, 50th, and 100th cycles for S-DM-AB at 0.5 C. **d** Upper plateau discharge capacity (QH) at 0.5 C. **e** Cycling performance of S-AB and S-DM-AB cathodes for 100 cycles at 0.5 C. Source: [73]

batteries. The approach involves the creation of 3D textural porous NHG architectures through a bio-templating chemical vapor deposition (CVD) method, utilizing diatomite as a naturally abundant growth substrate. The NHG separator, known for its high surface area, intricate inner-channel structure, and abundant nitrogen doping, combines physical confinement and chemical immobilization capabilities for polysulfides. This facilitates smooth lithium-ion diffusion, leading to impressive battery performance. Batteries with the NHG-based separator exhibit an initial capacity of 868 mAh/g, with an average capacity decay of only 0.067% per cycle at 2 C for 800 cycles. Additionally, a substantial 805 mAh/g capacity is achieved at a high sulfur loading of ~ 7.2 mg c/m$^2$. The study highlights the potential of constructing high-energy and long-life Li–S batteries through innovative separator modifications, showcasing the efficacy of the designed NHG architecture in addressing challenges posed by lithium polysulfides.

Similarly, Fan et al. [262] investigated lithium-sulfur (Li–S) batteries, known for their high theoretical energy density and potential as promising energy storage systems. However, the practical performance is hindered by lithium polysulfide (LiPSs) shuttling due to the slow sulfur redox reaction. Studies have explored using an interlayer between the cathode and separator to block LiPSs physically or chemically. Another approach is incorporating catalytic materials to expedite the conversion of LiPSs, with MXene being a potential candidate. Despite MXene's abundant surface chemistry, the aggregation of MXene sheets has been challenging, resulting in a loss of catalytic active sites. In their study, Fan et al. [262] introduce a novel diatomite/MXene (DE/MX) hybrid material as a bifunctional interlayer to enhance the adsorption/conversion of LiPSs in Li–S batteries. The diatomite's porous structure and silica-hydroxyl functional groups effectively trap LiPSs while preventing MXene aggregation. The DE/MX-based interlayer serves

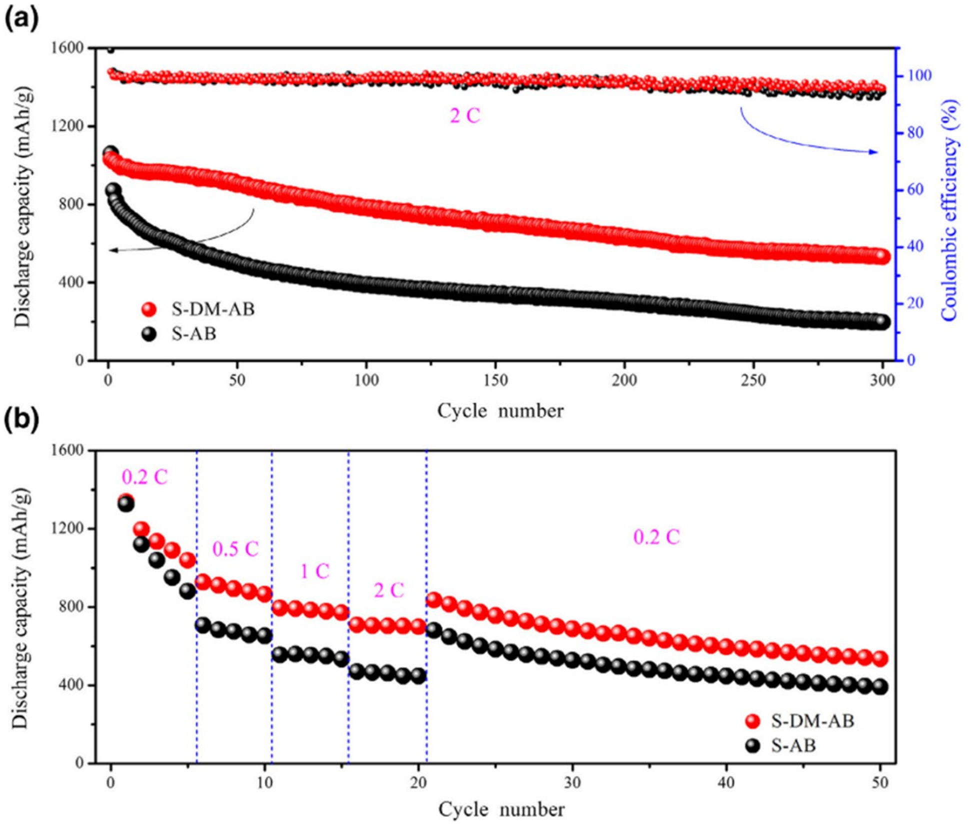

**Fig. 39** **a** Cycling performance comparison between S-AB and S-DM-AB cathodes at 2 C over 300 cycles. **b** Rate performance evaluation of S-AB and S-DM-AB cathodes across various *C* rates, ranging from 0.2 to 2 C. Source: [73]

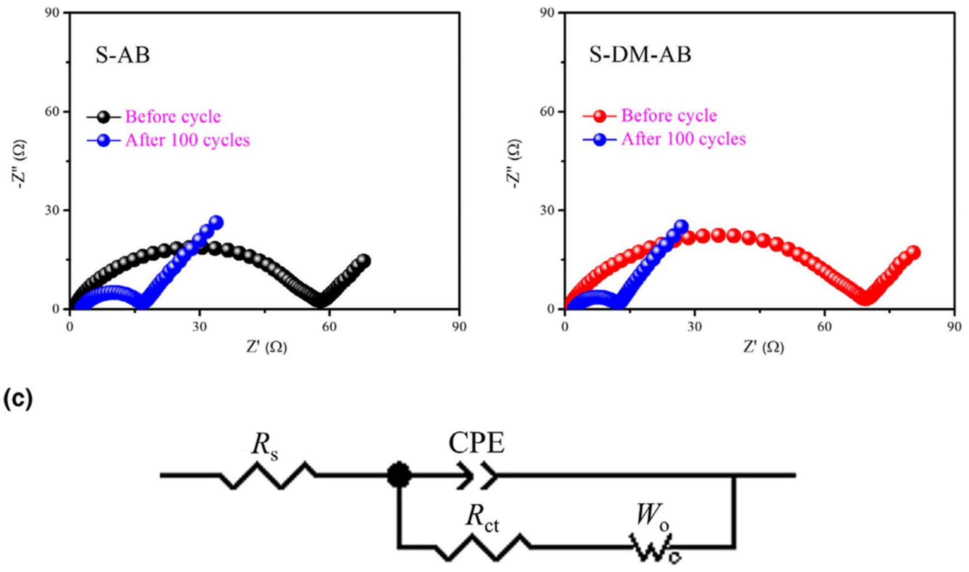

**Fig. 40** Electrochemical impedance spectra of **a** S-AB and **b** S-DM-AB pre- and post-100 cycles, along with **c** the corresponding equivalent circuit model. Source: [73]

dual functions, enhancing both chemical adsorption and promoting the conversion of LiPSs, as shown in Fig. 41a.

In their research, Fan et al. [262] introduced Li–S batteries featuring the DE/MX interlayer, resulting in enhanced cycling stability with a remarkably low-capacity decay of 0.059% per cycle over 1000 cycles at 1.0 C. Notably, the batteries demonstrated stable performance for 200 cycles, even with a high sulfur loading electrode of up to 6.0 mg/cm$^2$, as depicted in Fig. 42. The findings of this study offer a compelling strategy for constructing bifunctional interlayers, effectively impeding the shuttling of LiPS's and thereby advancing the real-world usage of Li–S batteries, as illustrated in Figs. 42 and 43.

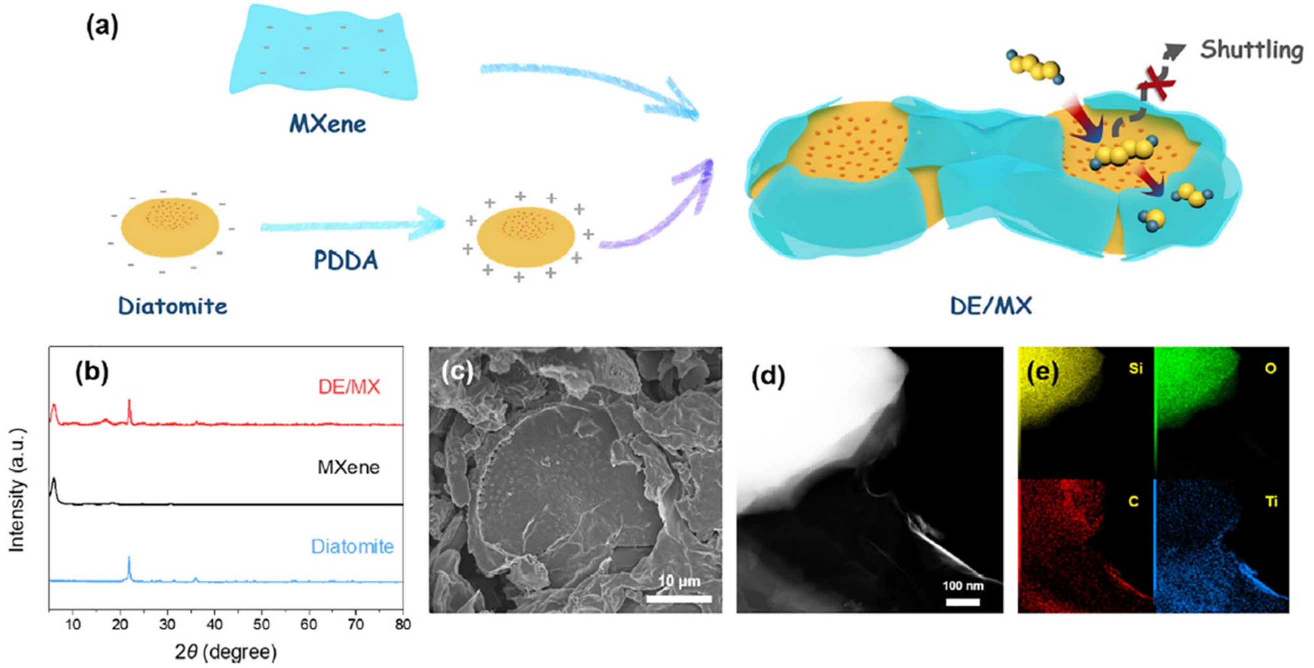

**Fig. 41** **a** Diagram illustrating the synthesis of DE/MX and the regulation of LiPSs on the DE/MX interlayer. **b** X-ray diffraction (XRD) profiles of DE/MX, diatomite, and MXene. **c** Scanning electron microscope (SEM) pictures. **d** High-angle annular dark-field scanning transmission electron microscope (HAADF-STEM) images. **e** EDS mapping corresponding to DE/MX. Source: [262]

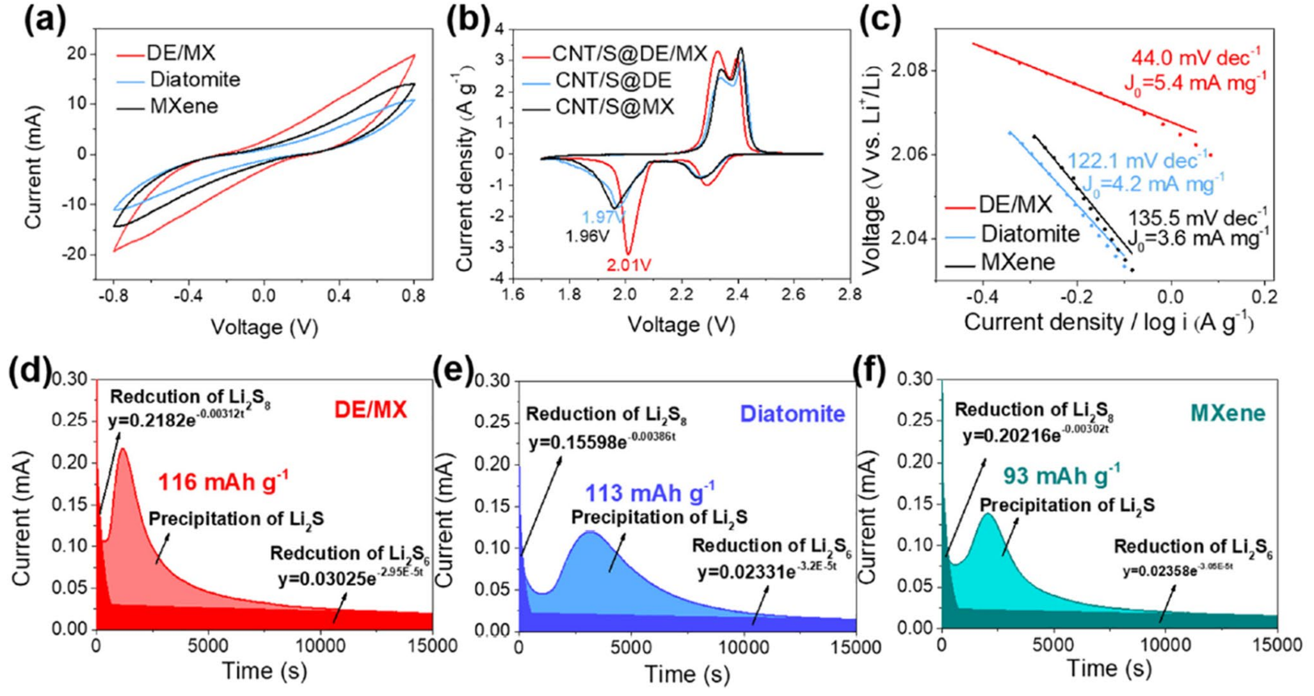

**Fig. 42** **a** CV profiles were recorded for $Li_2S_6$ symmetric cells employing electrodes composed of DE/MX, diatomite, and MXene loaded on CPs. **b** CV profiles were also obtained for cells utilizing CNT/S@DE/MX, CNT/S@DE, and CNT/S@MX configurations. **c** Tafel plots were generated to illustrate the reduction reaction of DE/MX, diatomite, and MXene as depicted in **b**. **d**–**f** Potentiostatic discharge profiles were examined for $Li_2S_8$/tetraglyme solution on DE/MX, diatomite, and MXene electrodes in separate experiments. Source: [262]

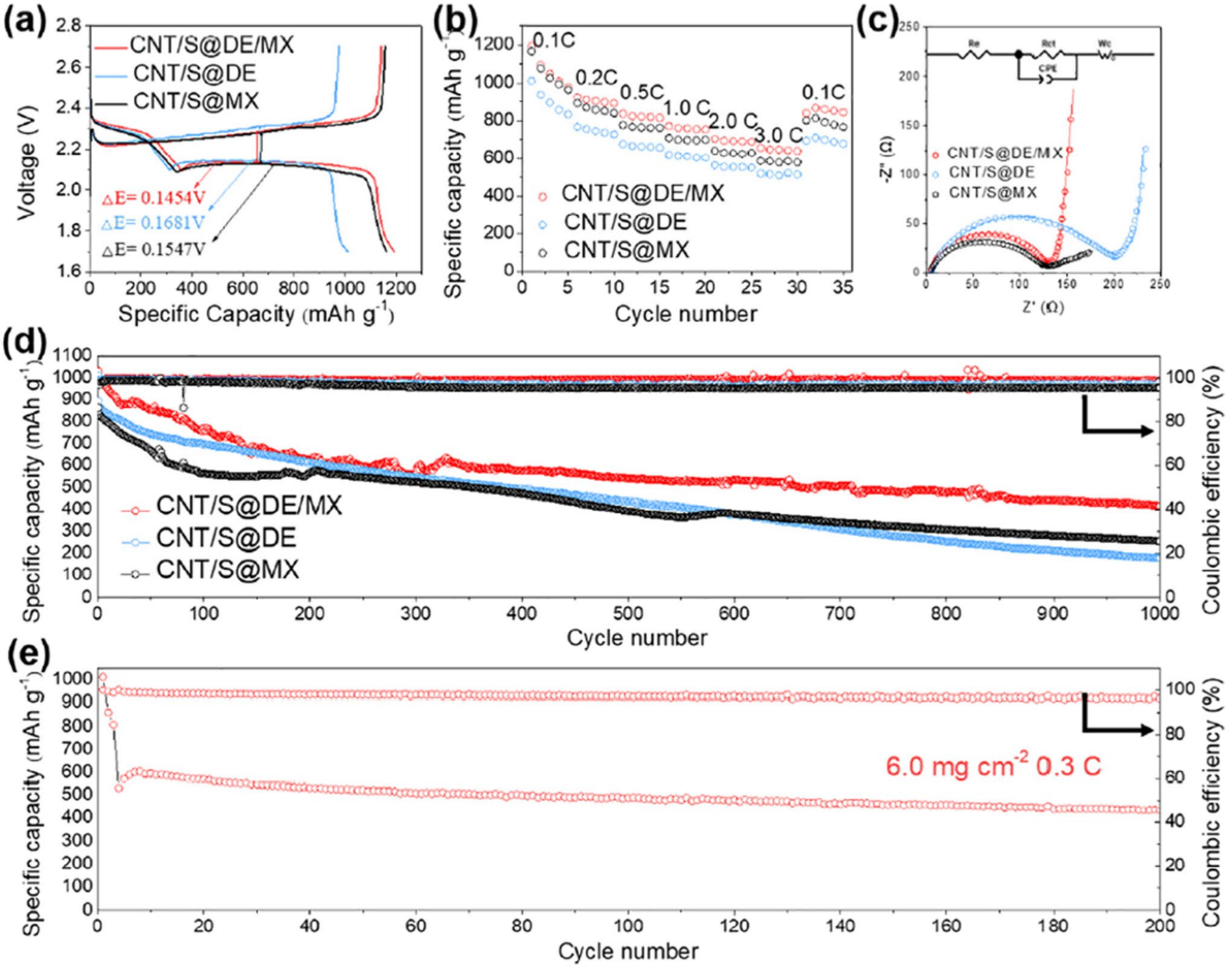

**Fig. 43** **a** Galvanostatic discharge/charge profiles of cells using various interlayers. **b** Rate performance comparison of cells with different interlayers under varying current densities. **c** Nyquist plots depicting impedance characteristics of cells with differing interlayers. Inset shows equivalent circuit fitting. **d** Long-term cycling performance at 1.0 C rate. **e** Cycling performance evaluation of cells employing DE/MX interlayer at high sulfur loading. Source: [262]

Similarly, Xia et al. [82] successfully produced porous carbon microspheres using Schizochytrium sp. microalgae. These microspheres demonstrated outstanding reversible capability and cathode properties and exhibited the capacity to encapsulate sulfur. The sulfur encapsulation played a pivotal role in mitigating electrode degradation in Li–S batteries, effectively addressing the well-known issue of lithium polysulfide accumulation, commonly referred to as the “shuttle effect.” This reduction in the shuttle effect holds significant importance in bolstering the overall performance of lithium-sulfur batteries, positioning them as a compelling and more energy-efficient alternative to traditional lithium batteries. To evaluate the electrochemical performance of the diatomite bio-templated synthesized electrode materials mentioned earlier, Table 3 outlines the electrochemical performances of numerous diatomite bio-templated synthesized electrode materials for electrochemical energy storage applications (supercapacitors, lithium-ion and lithium-sulfur batteries).

## Prospects and conclusion

### Prospects

Exploring diatomaceous earth (DE) as a material for electrode synthesis in supercapacitors and batteries shows promise and complexity. Insights from current research suggest many future development paths that could transform energy storage.

- Integration of Emerging Technologies: Emerging technologies will be crucial for future DE research. Using

**Table 3** Electrochemical performances of several diatomite bio-templated synthesized electrode for electrochemical energy storage application (supercapacitors, lithium ion and lithium sulfur batteries)

| Applications | Electrode material | Capacitance | Capacity decay | Capacitance retention | Energy density | Power density | Ref |
|---|---|---|---|---|---|---|---|
| Supercapacitor | MnFeOx-0 diatom replica | 228.6 F/g at 1 A/g | | 94.3% @ 4000 cycles | 51.5 Wh/kg | 9.1 kW/kg | [92] |
| Supercapacitor | diatomite@$TiO_2$@ $MnO_2$ | | | 94.1% @2000 cycles | | | [101] |
| Supercapacitor | Nitrogen-doped porous carbon (NPC-2) | 151.5 F/g@1 A/g | | 90.5% @10,000 cycles | 13.47 Wh/kg | 400 W/kg | [74] |
| Supercapacitor | $MnO_2$@CNTs/G/ diatomite | 880.0 F/g | | | 64.3 Wh/kg | 19.8 kW/kg | [254] |
| Supercapacitor | NiO-modified diatomite electrode | 218.7 F/g@1 M KOH | | 90.61% @1000 cycles | | | [45] |
| Supercapacitor | $MnO_2$-modified diatomite electrode | 202.6 F/g | | 95.92%@ 5000 cycles | | | [46] |
| Li-ion battery | Porous Si/C composites | 1628 mAh/g | | | | | [44] |
| Li-ion battery | 1D Si nanostructures coated with carbon (1D Si@C) | 813 mAh/g@1000 cycles@3 C | | 91%@200 cycles | 405 Wh/kg, | | [263] |
| Li-ion battery | SiO2@Al electrode | 730 mAh/g | | 95%@312 cycles | | | [43] |
| Li-ion battery | Dual-carbon-enhanced Si-based composite (Si/C/G) | 938 mAh/g | | | | | [259] |
| Li–S battery | S-DM-AB | 725.1 mAh/g | | | | | [73] |
| Li–S battery | N-doped hierarchical graphene (NHG) | 868 mAh/g | 0.067% per cycle | | | | [110] |
| Li–S battery | DE/MX | | 0.059% per cycle | | | | [262] |

artificial intelligence (AI) and machine learning (ML) to optimize the synthesis of DE-based electrode materials is promising. These tools help researchers find the best material configurations and synthesis conditions faster. This can improve research efficiency and lead to the discovery of new, high-performance electrode materials.

- Scalability and Practical Implementation: Scalability is a significant challenge. For DE to be widely adopted in industry, we need cost-effective and scalable synthesis methods. Future research should focus on making these methods suitable for large-scale production. Turning lab successes into commercially viable solutions is essential for using DE in supercapacitors and batteries.
- Environmental Sustainability: DE offers opportunities for eco-friendly electrode material synthesis. Future research could improve DE's use as a green, biocompatible template. This aligns with global trends toward sustainability. Combining DE with other sustainable materials or developing hybrid materials could enhance the environmental benefits of electrode materials.
- Interdisciplinary Collaboration: Interdisciplinary collaboration is vital for advancing DE research. Material science, chemistry, engineering, and environmental science researchers should work together. This can lead to innovative solutions, new synthesis methods, and a better understanding of DE's broader implications in supercapacitors and batteries.
- Technological Innovation: Technological innovation will drive the field forward. Using advanced computational tools, focusing on scalability, and adhering to sustainable practices are essential. Collaboration across disciplines will likely boost the development of DE-based electrode materials. As researchers explore DE's potential, exciting possibilities for sustainable, high-performance energy storage solutions will emerge.

## Conclusion

In conclusion, the comprehensive review on the utilization of diatomaceous earth (DE) as a bio-template material for synthesizing electrode materials in supercapacitors and battery applications represents a significant contribution to the field of energy storage research. The synthesis techniques, physiochemical characteristics, and electrochemical properties of DE-based electrode materials have been thoroughly examined, providing a better understanding of its potential to enhance supercapacitor and battery performance. This review emphasizes the usefulness of DE in creating hierarchical and porous structures within electrode materials. These unique structures facilitate efficient ion diffusion and maximize the surface area available for charge storage. By investigating the various materials synthesized using DE as a template, the paper further highlights the versatility of DE in accommodating various materials, thereby broadening its applicability in supercapacitor technology. A notable aspect of the review is its emphasis on the environmental sustainability of DE. The eco-friendly and biocompatible nature of DE distinguishes it from conventional synthesis methods that often involve hazardous chemicals and complex processes. This aligns with the global shift toward greener and more sustainable energy storage technologies, positioning DE as a promising candidate for environmentally conscious electrode material synthesis.

Despite the positive attributes of DE, the review acknowledges the existing challenges, such as scalability issues and cost considerations. These challenges, while serving as areas for improvement, also highlight the need for ongoing research efforts to optimize synthesis processes and overcome hurdles to practical implementation. The recognition of these challenges underscores the commitment of this review to presenting a balanced and realistic assessment of DE's potential in supercapacitor and battery applications. Integrating emerging technologies, particularly artificial intelligence and machine learning is proposed to optimize synthesis parameters and predict material performance. Such innovative approaches can potentially accelerate the development of efficient DE-based electrode materials. Additionally, the call for interdisciplinary collaboration among material scientists, chemists, engineers, and environmental scientists emphasizes the holistic approach needed to unlock the full potential of DE in supercapacitor and battery technology. The review consolidates existing knowledge and charts a course for future investigations. By addressing the challenges, highlighting the environmental benefits, and suggesting avenues for further exploration, the paper serves as a roadmap for researchers in the quest for sustainable and high-performance electrode materials for electrochemical energy storage devices. The findings presented in this review contribute significantly to the ongoing dialogue in the scientific community, fostering a deeper understanding of DE's role in shaping the future of energy storage technologies.

**Author contribution** Appiah Eugene Sefa: Conceptualization, Methodology, Validation, Formal analysis, Investigation, Resources, Writing – Original draft. Perseverance Dzikunu: Formal analysis, Writing – review & editing, Supervision, Validation, Samuel Olukayode Akinwamide: Conceptualization, Resources, Writing – review & editing, Supervision, Validation, Funding acquisition, Eric Agbemon Komla Fangnon: Formal analysis, Writing – review & editing, Supervision, Validation, Kwadwo Mensah-Darkwa: Conceptualization, Resources, Writing – review & editing, Supervision, Validation, Funding acquisition. Anthony Andrews: Conceptualization, Resources, Writing – review & editing, Supervision, Validation, Funding acquisition. Frank Ofori Agyemang: Formal analysis, Writing – review & editing, Supervision, Validation. Martinson Addo Nartey: Conceptualization, Formal analysis, Investigation, Resources, Writing – review & editing, Supervision, Validation. Katlego Makgopa: Conceptualization, Methodology, Formal analysis, Writing – review & editing, Supervision, Validation. Sven Bossuyt: Supervision and Funding acquisition.

**Funding** Open Access funding provided by Aalto University. The authors are grateful to the Ministry of Education and Culture Global South Programme, Finland, for financial support, the African Centre of Excellence (ACE) scholarship and Kwame Nkrumah University of Science and Technology (KNUST) Engineering Education Programme (KEEP), and the National Research Foundation (NRF) South Africa under the Competitive Support for Unrated Researchers (UID No. 138085) programmes.

**Data availability** No datasets were generated or analyzed during the current study.

## Declarations

**Conflict of interest** The authors declare no competing interests.

**Open Access** This article is licensed under a Creative Commons Attribution 4.0 International License, which permits use, sharing, adaptation, distribution and reproduction in any medium or format, as long as you give appropriate credit to the original author(s) and the source, provide a link to the Creative Commons licence, and indicate if changes were made. The images or other third party material in this article are included in the article's Creative Commons licence, unless indicated otherwise in a credit line to the material. If material is not included in the article's Creative Commons licence and your intended use is not permitted by statutory regulation or exceeds the permitted use, you will need to obtain permission directly from the copyright holder. To view a copy of this licence, visit http://creativecommons.org/licenses/by/4.0/.

## References

1. Herrera-Beurnio MC et al (2021) Bio-templating: an emerging synthetic technique for catalysts. A review. Catalysts 11(11):1364
2. Chodankar NR et al (2024) Revolutionizing implantable technology: biocompatible Supercapacitors as the future of power sources. Adv Funct Mater:2406819
3. Sarfraz N, Khan I, Hendi AH (2023) Biomass-derived graphene-based supercapacitors. In: Biomass-based supercapacitors: design, fabrication and sustainability, pp 269–287
4. Quach NKN et al (2017) The influence of the activation temperature on the structural properties of the activated carbon xerogels and their electrochemical performance. Adv Mater Sci Eng 2017(1):8308612
5. Shinde PA, Ariga K (2023) Two-dimensional nanoarchitectonics for two-dimensional materials: interfacial engineering of transition-metal dichalcogenides. Langmuir 39:18175–18186
6. Shinde PA, Mahamiya V, Safarkhani M, Chodankar NR, Ishii M, Ma R, Ghaferi A Al, Shrestha LK, Ariga K (2024) Unveiling the nanoarchitectonics of interfacial electronic coupling in

atomically thin 2D WO3/WSe2 heterostructure for sodium-ion storage in aqueous system. Adv Funct Mater. 2406333

7. Nanzumani NM, Agyemang FO, Mensah-Darkwa K, Appiah ES, Arthur EK, Gikunoo E, Koomson B, Jadhav AR, Raji A (2022) Molten salt synthesis of nitrogen-doped hierarchical porous carbon from plantain peels for high-performance supercapacitor. J Electroanal Chem 920:116645
8. Khan I, Lee JH, Park J, Wooh S (2022) Nano/micro-structural engineering of Nafion membranes for advanced electrochemical applications. J Saudi Chem Soc 26:101511
9. Shinde PA, Chodankar NR, Kim HJ, Abdelkareem MA, Al GA, Han YK, Olabi AG, Ariga K (2023) Ultrastable 1T–2H WS2 heterostructures by nanoarchitectonics of phosphorus-triggered phase transition for hybrid supercapacitors. ACS Energy Lett 8:4474–4487
10. Wang C, Yan B, Zheng J, Feng L, Chen Z, Zhang Q, Liao T, Chen J, Jiang S, Du C, He S (2022) Recent progress in template-assisted synthesis of porous carbons for supercapacitors. Adv Powder Mater 1:100018
11. Dai J, Ma Y, Ren S, Fang G (2018) Preparation and electrochemical capacitive performance of phenolated calcium lignosulfonate-based phenol formaldehyde resin porous carbon. J Mater Res 33:1211–1218
12. Balasubramaniam S et al (2020) Comprehensive insight into the mechanism, material selection and performance evaluation of supercapatteries. Nano-Micro Letters 12:1–46
13. Shinde PA, Jun SC (2020) Review on recent progress in the development of tungsten oxide based electrodes for electrochemical energy storage. Chemsuschem 13:11–38
14. Sarfraz N, Kanwal N, Ali M, Ali K, Hasnain A, Ashraf M, Ayaz M, Ifthikar J, Ali S, Hendi A, Baig N, Ehsan MF, Shah SS, Khan R, Khan I (2024) Materials advancements in solid-state inorganic electrolytes for highly anticipated all solid Li-ion batteries. Energy Storage Mater 71:103619
15. Huang DR, Jiang YJ, Liou RL, Chen CH, Chen YA, Tsai CH (2015) Enhancing the efficiency of dye-sensitized solar cells by adding diatom frustules into TiO 2 working electrodes. Appl Surf Sci 347:64–72
16. Bokov D et al (2021) Nanomaterial by sol-gel method: synthesis and application. Adv Mater Sci Eng 2021(1):5102014
17. Jeyabanu K, Devendran P, Manikandan A, Packiaraj R, Ramesh K, Nallamuthu N (2019) Preparation and characterization studies of La doped CuS nanospheres by microwave irradiation for high performance supercapacitors. Phys B Condens Matter 573:92–101
18. Mohamed MA, Wan Salleh WN, Jaafar J, Rosmi MS, Zul ZA, Abd Mutalib M, Ismail AF, Tanemura M (2017) Carbon as amorphous shell and interstitial dopant in mesoporous rutile TiO 2: bio-template assisted sol-gel synthesis and photocatalytic activity. Appl Surf Sci 393:46–59
19. Nassif N, Livage J (2011) From diatoms to silica-based biohybrids. Chem Soc Rev 40:849–859
20. Shang Y et al (2015) Enhancing solar cell efficiency using photon upconversion materials. Nanomaterials 5(4):1782–1809
21. Ababneh H, Hameed BH (2021) Chitosan-derived hydrothermally carbonized materials and its applications: a review of recent literature. Int J Biol Macromol 186:314–327
22. Woo H, Kang J, Kim J, Kim C, Nam S, Park B (2016) Development of carbon-based cathodes for Li-air batteries: present and future. Electron Mater Lett 12:551–567
23. Assirey EAR (2019) Perovskite synthesis, properties and their related biochemical and industrial application. Saudi Pharm J 27:817–829
24. Ould-Ely T, Bawazer LA, Morse DE (2017) 2.1 Bio-inspired silica nanomaterials for biomedical applications. Elsevier Ltd.
25. Arfin T (2021) Emerging trends in lab-on-a-chip for biosensing application. In: Functionalized nanomaterials based devices for environmental applications, pp 199–218
26. Leonardo S, Prieto-simón B, Campàs M (2016) Past, present and future of diatoms in biosensing. Trends Anal Chem 79:276–285
27. Owczarzy A, Kurasiński R, Kulig K, Rogóż W, Szkudlarek A, Maciążek-Jurczyk M (2020) Collagen-structure, properties and application. Eng Biomater 156:17–23
28. Stanisz M, Klapiszewski Ł, Jesionowski T (2020) Recent advances in the fabrication and application of biopolymer-based micro- and nanostructures: a comprehensive review. Chem Eng J 397:125409
29. Gelse K, Pöschl E, Aigner T (2003) Collagens - structure, function, and biosynthesis. Adv Drug Deliv Rev 55:1531–1546
30. Bertone JF, Cizeron J, Wahi RK, Bosworth JK, Colvin VL (2003) Hydrothermal synthesis of quartz nanocrystals. Nano Lett 3:655–659
31. Saadati M, Imani S, Warzaghany EN, Dehghani MA, Hajihosseini S, Mostaghaci M, Fu JJ (2016) Design and simulation of diatomaceous nano-filter using titanium oxide nanoparticles (Tio2-NPs) and frustule nanostructures: based on flow dynamics modeling in pilot-scale. Dig J Nanomater Biostructures 11:453–463
32. Zhang DY, Wang Y, Cai J, Pan JF, Jiang XG, Jiang YG (2012) Bio-manufacturing technology based on diatom micro- and nanostructure. Chinese Sci Bull 57:3836–3849
33. Karaman ES, Wang Z, Di Benedetto G, Zunino JL, Meng X, Mitra S (2019) Fabrication of supercapacitors and flexible electrodes using biosilica from cultured diatoms. Mater Today Energy 11:166–173
34. Gautam S, Pandey LK, Vinayak V, Arya A (2017) Morphological and physiological alterations in the diatom Gomphonema pseudoaugur due to heavy metal stress. Ecol Indic 72:67–76
35. Aggrey P, Nartey M, Andrews A, Salimon AI, Korsunsky AM (2021) On the diatomite-based nanostructure-preserving material synthesis for energy applications. 11:31884–31922
36. Hu Z, Zheng S, Li J, Zhang S, Liu M, Wang Z, Li J, Sun H (2022) Pore structure and surface properties of diatomite with mechanical grinding and its influence on humidity control. In: Physicochemical problems of mineral processing, vol 58
37. Weldemariam Y, Enke D, Schneider D, Alemayehu E (2019) Thermochemical purification, technical properties, and characterization of thermochemical purification, technical properties, and characterization of Ethiopian diatomite from Adami - Tulu deposit. Chem Africa. https://doi.org/10.1007/s42250-019-00080-z
38. Fields PG (1998) Diatomaceous earth: advantages and limitations. In: Proceedings of the seventh international working conference on stored-product protection, vol 1998, pp 781–784
39. Elden H, Morsy G, Bakr M (2010) Diatomite: its characterization, modifications and applications. Asian J Mater Sci 3:121–136
40. Sriram G, Kigga M, Uthappa UT, Rego RM, Thendral V, Kumeria T, Jung H, Kurkuri MD (2020) Naturally available diatomite and their surface modification for the removal of hazardous dye and metal ions: a review. Adv Colloid Interface Sci 282:102198
41. Villani M, Onesto V, Coluccio ML, Valpapuram I, Majewska R, Alabastri A, Battista E, Schirato A, Calestani D, Coppedé N, Zappettini A, Amato F, Di Fabrizio E, Gentile F (2019) Transforming diatomaceous earth into sensing devices by surface modification with gold nanoparticles. Micro Nano Eng 2:29–34
42. Li B, Wang T, Le Q, Qin R, Zhang Y, Chun H (2023) Surface reconstruction, modification and functionalization of natural

diatomites for miniaturization of shaped heterogeneous catalysts. Nano Mater Sci 5:293–311

43. Li Q, Zhao J, Yao W, Yu C, Ding X (2023) A SiO2@Al as stable and long-cycle anode for lithium-ion batteries. Mater Chem Phys 305:128015
44. Wang M, Fan L, Huang M, Li J, Qu X (2012) Conversion of diatomite to porous Si/C composites as promising anode materials for lithium-ion batteries. J Power Sources 219:29–35
45. Zhang YX, Li F, Huang M, Xing Y, Gao X, Li B, Guo ZY, Guan YM (2014b) Hierarchical NiO moss decorated diatomites via facile and templated method for high performance supercapacitors. Mater Lett 120:263–266
46. Zhang YX, Huang M, Li F, Wang XL, Wen ZQ (2014) One-pot synthesis of hierarchical MnO2-modified diatomites for electrochemical capacitor electrodes. J Power Sources 246:449–456
47. Sun L, Yuan G, Gao L, Yang J, Chhowalla M, Gharahcheshmeh MH, Gleason KK, Choi YS, Hong BH, Liu Z (2021) Chemical vapour deposition. Nat Rev Methods Primers 1(1):5
48. Schlee P, Hosseinaei O, Baker D, Landmér A, Tomani P, Mostazo-López MJ, Cazorla-Amorós D, Herou S, Titirici MM (2019) From waste to wealth: from kraft lignin to free-standing supercapacitors. Carbon N Y 145:470–480
49. Liu F, Gao Y, Zhang C, Huang H, Yan C, Chu X, Xu Z, Wang Z, Zhang H, Xiao X, Yang W (2019) Highly microporous carbon with nitrogen-doping derived from natural biowaste for high-performance flexible solid-state supercapacitor. J Colloid Interface Sci 548:322–332
50. Zeng Z, Dong Y, Yuan S, Zhao W, Wang L, Liu S, Yang Y, Ge P, Sun W, Ji X (2022) Natural mineral compounds in energy-storage systems: development, challenges, prospects. Energy Storage Mater 45:442–464
51. Wang C, Li K, Sun Q, Zhu S, Zhang C, Zhang Y, Shi Z, Hu Y, Zhang Y (2023) Diatomite-like KFeS2 for use in high-performance electrodes for energy storage and oxygen evolution. Nanomaterials 13(4):643
52. Assylkhanova D, Nazhipkyzy M, Maltay A, Zhaparova A, Niyazbaeva A (2022) Electrode materials for Li-ion batteries based on diatomite. Горение И Плазмохимия 20:191–197
53. Azwar E, Wan Mahari WA, Chuah JH, Vo DVN, Ma NL, Lam WH, Lam SS (2018) Transformation of biomass into carbon nanofiber for supercapacitor application – a review. Int J Hydrogen Energy 43:20811–20821
54. Li J, Jiang Q, Wei L, Zhong L, Wang X (2020) Simple and scalable synthesis of hierarchical porous carbon derived from cornstalk without pith for high capacitance and energy density. J Mater Chem A 8:1469–1479
55. Jiang G, Senthil RA, Sun Y, Kumar TR, Pan J (2022) Recent progress on porous carbon and its derivatives from plants as advanced electrode materials for supercapacitors. J Power Sources 520:230886
56. Jeżowski P, Kowalczewski PŁ (2019) Starch as a green binder for the formulation of conducting glue in supercapacitors. Polymers 11(10):1648
57. Zhuo H, Hu Y, Chen Z, Zhong L (2019) Cellulose carbon aerogel/PPy composites for high-performance supercapacitor. Carbohydr Polym 215:322–329
58. Enock TK, King'ondu CK, Pogrebnoi A, Jande YAC (2017) Status of biomass derived carbon materials for supercapacitor application. Int J Electrochem 2017:1–14
59. Al A, Meltem R (2021) High-performance nanostructured bio-based carbon electrodes for energy storage applications. Springer, Netherlands
60. Siburian R, Sihotang H, Lumban Raja S, Supeno M, Simanjuntak C (2018) New route to synthesize of graphene nano sheets. Orient J Chem 34:182–187
61. Azhar A, Yamauchi Y, Allah AE, Alothman ZA, Badjah AY, Naushad M, Habila M, Wabaidur S, Wang J, Zakaria MB (2019) Nanoporous iron oxide/carbon composites through in-situ deposition of Prussian blue nanoparticles on graphene oxide nanosheets and subsequent thermal treatment for supercapacitor applications. Nanomaterials 9(5):776
62. Liu C, Han G, Chang Y, Xiao Y, Li M, Zhou W, Fu D, Hou W (2016) Properties of porous carbon derived from cornstalk core in high-performance electrochemical capacitors. ChemElectroChem 3:323–331
63. Wang Y, Song Y, Xia Y (2016) Electrochemical capacitors: mechanism, materials, systems, characterization and applications. Chem Soc Rev 45:5925–5950
64. Zhao J, Burke AF (2021) Review on supercapacitors: technologies and performance evaluation. J Energy Chem 59:276–291
65. Sharma P, Kumar V (2023) Supercapacitor and electrochemical techniques: a brief review. Results Chem 5(1):100885
66. Pavlenko V, Żółtowska S, Haruna AB, Zahid M, Mansurov Z, Supiyeva Z, Galal A, Ozoemena KI, Abbas Q, Jesionowski T (2022) A comprehensive review of template-assisted porous carbons: modern preparation methods and advanced applications. Mater Sci Eng: R: Rep 149:100682
67. Losic D, Mitchell JG, Lal R, Voelcker NH (2007) Rapid fabrication of micro- and nanoscale patterns by replica molding from diatom biosilica. Adv Funct Mater 17:2439–2446
68. Roostaei T, Rahimpour MR, Zhao H, Eisapour M, Chen Z, Hu J (2023) Recent advances and progress in biotemplate catalysts for electrochemical energy storage and conversion. Adv Colloid Interface Sci 318:102958
69. Iro ZS, Subramani C, Dash SS (2016) A brief review on electrode materials for supercapacitor. Int J Electrochem Sci 11(12):10628–10643
70. Hui CY, Kan CW, Mak CL, Chau KH (2019) Flexible energy storage system—an introductory review of textile-based flexible supercapacitors. Processes 7(12):922
71. Verma S, Pandey VK, Verma B (2022) Synthesis and supercapacitor performance studies of graphene oxide based ternary composite. Mater Technol 37:2915–2931
72. Di F, Wang N, Li L, Geng X, Yang H, Zhou W, Sun C, An B (2021) Coral-like porous composite material of silicon and carbon synthesized by using diatomite as self-template and precursor with a good performance as anode of lithium-ions battery. J Alloys Compd 854:157253
73. Li Z, Zhang N, Sun Y, Ke H, Cheng H (2017) Application of diatomite as an effective polysulfides adsorbent for lithium-sulfur batteries. J Energy Chem 26:1267–1275
74. Huang Y, Wang Y, Cai Y, Wang H, Li Q, Wu Q, Liu K, Ma Z (2021) Diatomite waste derived N-doped porous carbon for applications in the oxygen reduction reaction and supercapacitors. Nanoscale Adv 3:3860–3866
75. Han J, Zhang LL, Lee S, Oh J, Lee KS, Potts JR, Ji J, Zhao X, Ruoff RS, Park S (2013) Generation of B-doped graphene nanoplatelets using a solution process and their supercapacitor applications. ACS Nano 7:19–26
76. Wu L, Li Y, Fu Z, Su BL (2020) Hierarchically structured porous materials: synthesis strategies and applications in energy storage. Natl Sci Rev 7(11):1667–1701
77. Ren M, Zhang C yun, Wang Y lin, Cai J jun (2018) Development of N-doped carbons from zeolite-templating route as potential electrode materials for symmetric supercapacitors. Int J Miner Metall Mater 25:1482–1492
78. Zhang W, Cheng RR, Bi HH, Lu YH, Ma LB, He XJ (2021) A review of porous carbons produced by template methods for supercapacitor applications. Xinxing Tan Cailiao/New Carbon Mater 36:69–81

79. Zhang L, Liu L, Hu X, Yu Y, Lv H, Chen A (2018) N-doped mesoporous carbon sheets/hollow carbon spheres composite for supercapacitors. Langmuir 34:15665–15673
80. Li R, Wang L, Shahbazi A (2015) A review of hydrothermal carbonization of carbohydrates for carbon spheres preparation. Trends Renew Energy 1:43–56
81. Du J, Liu L, Hu Z, Yu Y, Zhang Y, Hou S, Chen A (2018) Raw-cotton-derived N-doped carbon fiber aerogel as an efficient electrode for electrochemical capacitors. ACS Sustain Chem Eng 6:4008–4015
82. Xia Y, Fang R, Xiao Z, Huang H, Gan Y, Yan R, Lu X, Liang C, Zhang J, Tao X, Zhang W (2017) Confining sulfur in N-doped porous carbon microspheres derived from microalgaes for advanced lithium-sulfur batteries. ACS Appl Mater Interfaces 9:23782–23791
83. Ma C, Wu L, Dirican M, Cheng H, Li J, Song Y, Shi J, Zhang X (2021) ZnO-assisted synthesis of lignin-based ultra-fine microporous carbon nanofibers for supercapacitors. J Colloid Interface Sci 586:412–422
84. Díez N, Fuertes AB, Sevilla M (2021) Molten salt strategies towards carbon materials for energy storage and conversion. Energy Storage Mater 38:50–69
85. Zhang X, Jian W, Zhao L, Wen F, Chen J, Yin J, Qin Y, Lu K, Zhang W, Qiu X (2022) Direct carbonization of sodium lignosulfonate through selftemplate strategies for the synthesis of porous carbons toward supercapacitor applications. Colloids Surf A Physicochem Eng Asp 636:128191
86. Shreya MK, Indhumathi C, Rajarajeswari GR, Ashokkumar V, Preethi T (2021) Facile green route sol–gel synthesis of nanotitania using bio-waste materials as templates. Clean Technol Environ Policy 23:163–171
87. Estevez L, Prabhakaran V, Garcia AL, Shin Y, Tao J, Schwarz AM, Darsell J, Bhattacharya P, Shutthanandan V, Zhang JG (2017) Hierarchically porous graphitic carbon with simultaneously high surface area and colossal pore volume engineered via ice templating. ACS Nano 11:11047–11055
88. Vinodh R, Sasikumar Y, Kim HJ, Atchudan R, Yi M (2021) Chitin and chitosan based biopolymer derived electrode materials for supercapacitor applications: a critical review. J Ind Eng Chem 104:155–171
89. Pandey GP, Klankowski SA, Liu T, Wu J, Li J (2017) Toward highly stable solid-state unconventional thin-film battery-supercapacitor hybrid devices: interfacing vertical core-shell array electrodes with a gel polymer electrolyte. J Power Sources 342:1006–1016
90. Chen X, Chi M, Xing L, Xie X, Liu S, Liang Y, Zheng M, Hu H, Dong H, Liu Y, Jiang SP, Xiao Y (2019) Natural plant template-derived cellular framework porous carbon as a high-rate and long-life electrode material for energy storage. ACS Sustain Chem Eng 7:5845–5855
91. Li P, Xie H, Liu Y, Wang J, Wang X, Xie Y, Hu W, Xie T, Wang Y, Zhang Y (2020) Dual-templated 3D nitrogen-enriched hierarchical porous carbon aerogels with interconnected carbon nanosheets from self-assembly natural biopolymer gel for supercapacitors. Electrochim Acta 353:136514
92. Li K, Liu X, Zheng T, Jiang D, Zhou Z, Liu C (2019) Tuning MnO 2 to FeOOH replicas with bio-template 3D morphology as electrodes for high performance asymmetric supercapacitors. Chem Eng J 370:136–147
93. Loganathan NN, Perumal V, Pandian BR, Atchudan R, Edison TNJI, Ovinis M (2022) Recent studies on polymeric materials for supercapacitor development. J Energy Storage 49:104149
94. Jiang T, Duan Q, Zhu J, Liu H, Yu L (2020) Starch-based biodegradable materials: challenges and opportunities. Adv Ind Eng Polym Res 3:8–18
95. Loganathan, N.N., Perumal, V., Pandian, B.R., Atchudan, R., Edison, T.N.J.I. and Ovinis, M., 2022. Recent studies on polymeric materials for supercapacitor development. *Journal of Energy Storage*, *49*, p.104149.
96. Wickramaratne NP, Xu J, Wang M, Zhu L, Dai L, Jaroniec M (2014) Nitrogen enriched porous carbon spheres: attractive materials for supercapacitor electrodes and CO2 adsorption. Chem Mater 26:2820–2828
97. Asnawi ASFM, Aziz SB, Saeed SR, Yusof YM, Abdulwahid RT, Al-Zangana S, Karim WO, Kadir MFZ (2020) Solid-state EDLC device based on magnesium ion-conducting biopolymer composite membrane electrolytes: impedance, circuit modeling, dielectric properties and electrochemical characteristics. Membranes 10(12):389
98. Wu MH, Li KL, Zhang XY, Gan P, Ge JL, Tian DN, Jiang B, Liu XY, Zhang YX (2018) Tuning hierarchical ferric nanostructures-decorated diatomite for Supercapacitors. Nanoscale Res Lett 13(1):407
99. Angel N, Li S, Yan F, Kong L (2022) Recent advances in electrospinning of nanofibers from bio-based carbohydrate polymers and their applications. Trends Food Sci Technol 120:308–324
100. Cai X, Zhu G, Zhang W, Zhao H, Wang C, Qiu S, Wei Y (2006) Diatom-templated synthesis of ordered meso/macroporous hierarchical materials. Eur J Inorg Chem 2006(18):3641–3645
101. Guo XL, Kuang M, Li F, Ying X, Xin Y, Dong F, Losic D (2016) Engineering of three dimensional (3-D ) diatom @ TiO 2 @ MnO 2 composites with enhanced supercapacitor performance. Electrochim Acta 190:159–167
102. Alijani H (1999) Synthesis of carbon nanotubes by CVD method in the presence of Fe/diatomite nanocatalyst and application for removal of Co2+ ions. 90:159875
103. Junied Arbaz S, Chandra Sekhar S, Ramulu B, Nagaraju M, Su YuJ (2022) Electrodeposited cobalt sulfide nanolayer fenced nickel-copper carbonate hydroxide nanowires as an electrode for hybrid supercapacitors: a wind turbine-driven energy storage system for portable applications. Appl Surf Sci 602:154288
104. Biswas S, Drzal LT (2010) Multilayered nanoarchitecture of graphene nanosheets and polypyrrole nanowires for high performance supercapacitor electrodes. Chem Mater 22:5667–5671
105. Liu Y, Wang X, Jiang X, Li X, Yu L (2018) Shape-controlled synthesis of porous carbons for flexible asymmetric supercapacitors. Nanoscale 10:22848–22860
106. Cheng P, Gao S, Zang P, Yang X, Bai Y, Xu H, Liu Z, Lei Z (2015) Hierarchically porous carbon by activation of shiitake mushroom for capacitive energy storage. Carbon N Y 93:315–324
107. Chang J, Gao Z, Wang X, Wu D, Xu F, Wang X, Guo Y, Jiang K (2015) Activated porous carbon prepared from paulownia flower for high performance supercapacitor electrodes. Electrochim Acta 157:290–298
108. Hoffmann V, Jung D, Zimmermann J, Correa CR, Elleuch A, Halouani K, Kruse A (2019) Conductive carbon materials from the hydrothermal carbonization of vineyard residues for the application in electrochemical double-layer capacitors (EDLCs) and direct carbon fuel cells (DCFCs). Materials 12(10):1703
109. Mensah-Darkwa K, Zequine C, Kahol PK, Gupta RK (2019) Supercapacitor energy storage device using biowastes: a sustainable approach to green energy. Sustainability 11(2):414
110. Li Q, Song Y, Xu R, Zhang L, Gao J, Xia Z et al (2018) Biotemplating growth of nepenthes-like N-doped graphene as a bifunctional polysulfide scavenger for Li–S batteries. ACS Nano 12(10):10240–10250
111. Guo T, Song Y, Sun Z, Wu Y, Xia Y, Li Y, Sun J, Jiang K, Dou S, Sun J (2020) Bio-templated formation of defect-abundant VS 2 as a bifunctional material toward high-performance hydrogen

evolution reactions and lithium – sulfur batteries. J Energy Chem 42:34–42

112. Lv Y, Li L, Zhou Y, Yu M, Wang J, Liu J, Zhou J, Fan Z, Shao Z (2017) A cellulose-based hybrid 2D material aerogel for a flexible all-solid-state supercapacitor with high specific capacitance. RSC Adv 7:43512–43520
113. Xu Z, Zhang Z, Yin H, Hou S, Lin H, Zhou J, Zhuo S (2020) Investigation on the role of different conductive polymers in supercapacitors based on a zinc sulfide/reduced graphene oxide/conductive polymer ternary composite electrode. RSC Adv 10:3122–3129
114. Zhong Y, Shi T, Huang Y, Cheng S, Liao G, Tang Z (2018) One-step synthesis of porous carbon derived from starch for all-carbon binder-free high-rate supercapacitor. Electrochim Acta 269:676–685
115. Wang G, Xu Y, Wang C, Gao Y, Li L (2020) Synthesis of two kinds of mesoporous diatomite by microwave assisted sol-gel method and its adsorption of Ammonia nitrogen in wastewater. IOP Conf Ser Mater Sci: Eng 782:022044
116. Lamastra FR, Grilli ML, Leahu G, Belardini A, Li Voti R, Sibilia C, Salvatori D, Cacciotti I, Nanni F (2018) Photoacoustic spectroscopy investigation of zinc oxide/diatom frustules hybrid powders. Int J Thermophys 39:1–10
117. Lorkit P, Panapoy M, Ksapabutr B (2014) Iron oxide-based supercapacitor from ferratrane precursor via sol-gel-hydrothermal process. Energy Procedia 56:466–473
118. Cao Z, Wei B (2013) A perspective: carbon nanotube macro-films for energy storage. Energy Environ Sci 6:3183–3201
119. Wei K, Zhang F, Yang Y, Zhai B, Wang X, Song Y (2022) Oxygenated N-doped porous carbon derived from ammonium alginate: facile synthesis and superior electrochemical performance for supercapacitor. J Energy Storage 51:104342
120. Ma Y, Wu D, Wang T, Jia D (2020) Nitrogen, phosphorus Co-doped carbon obtained from amino acid based resin xerogel as efficient electrode for supercapacitor. ACS Appl Energy Mater 3:957–969
121. Wu C-W, Li P-H, Wei Y-M, Yang C, Wu W-J (2022) Review on the preparation and application of lignin-based carbon aerogels. RSC Adv 12:10755–10765
122. Peng K, Wang W, Zhang J, Ma Y, Lin L, Gan Q, Chen Y, Feng C (2022) Preparation of chitosan/sodium alginate conductive hydrogels with high salt contents and their application in flexible supercapacitors. Carbohydr Polym 278:118927
123. Al-luhaibi AA, Sendi RK (2022) Synthesis, potential of hydrogen activity, biological and chemical stability of zinc oxide nanoparticle preparation by sol – gel: a review. J Radiat Res Appl Sci 15:238–254
124. Chen X, Kierzek K, Cendrowski K, Pelech I, Zhao X, Feng J, Kalenczuk RJ, Tang T, Mijowska E (2012) CVD generated mesoporous hollow carbon spheres as supercapacitors. Colloids Surfaces A Physicochem Eng Asp 396:246–250
125. Wang B, Li F, Yang P, Yang Y, Hu J, Wei J, Yu Q (2018) In situ synthesis of diatomite–carbon nanotube composite adsorbent and its adsorption characteristics for phenolic compounds. J Chem Eng Data 64(1):360–371
126. Saleem AM, Boschin A, Lim D, Desmaris V, Johansson P (2017) Coin-cell supercapacitors based on CVD grown and vertically aligned carbon nanofibers (VACNFs). Int J Electrochem Sci 12(7):1452–3981
127. Imran M, Afzal AM, Iqbal MW, Hegazy HH, Iqbal MZ, Mumtaz S, Qureshi R (2023) Manganese (sulfide/oxide) based electrode materials advancement in supercapattery devices. Mater Sci Semicond Process 158:107366
128. Nazhipkyzy M, Nemkayeva RR, Nurgain A, Seitkazinova AR, Dinistanova BK, Issanbekova AT, Zhylybayeva N, Bergeneva NS, Mamatova GU (2022) The use of diatomite as a catalyst carrier for the synthesis of carbon nanotubes. Nanomaterials 12(11):1817
129. Li K, Hu Z, Zhao R, Zhou J, Jing C, Sun Q, Rao J, Yao K, Dong B, Liu X, Li H, Zhang Y, Ji J (2021) A multidimensional rational design of nickel–iron sulfide and carbon nanotubes on diatomite via synergistic modulation strategy for supercapacitors. J Colloid Interface Sci 603:799–809
130. Ma X, Kang Z (2019) A facile electrodeposition technique for synthesis of nickel sulfides/carbon nanotubes nanocomposites as high performance electrodes for supercapacitor. Mater Lett 236:468–471
131. Shari S (2021) Highly improved supercapacitance properties of MnFe2O4 nanoparticles by MoS2 nanosheets
132. Zhang L, You T, Zhou T, Zhou X, Xu F (2016) Interconnected hierarchical porous carbon from lignin-derived byproducts of bioethanol production for ultra-high performance supercapacitors. ACS Appl Mater Interfaces 8:13918–13925
133. Zhao Z, Tang Z, Zhang Y (2021) Discarded dates as a sustainable source to prepare porous carbon-aerogel with multiple energy storage functions. Ind Crop Prod 170:113772
134. Palem RR, Ramesh S, Yadav HM, Kim JH, Sivasamy A, Kim HS, Kim JH, Lee SH, Kang TJ (2020) Nanostructured Fe2O3@ nitrogen-doped multiwalled nanotube/cellulose nanocrystal composite material electrodes for high-performance supercapacitor applications. J Mater Res Technol 9:7615–7627
135. Manasa P, Lei ZJ, Ran F (2020) Biomass waste derived low cost activated carbon from carchorus olitorius (jute fiber) as sustainable and novel electrode material. J Energy Storage 30:101494
136. Gopalakrishnan A, Badhulika S (2018) Ultrathin graphene-like 2D porous carbon nanosheets and its excellent capacitance retention for supercapacitor. J Ind Eng Chem 68:257–266
137. Gan YX, Jayatissa AH, Yu Z, Chen X, Li M (2020) Hydrothermal synthesis of nanomaterials. J Nanomater 2020:917013
138. Berwal P, Rani S, Sihag S, Singh P, Dahiya R, Kumar A, Sanger A, Kumar A, Kumar V (2024) Hydrothermal synthesis of MoS 2 with tunable band gap for future nano-electronic devices. Inorg Chem Commun 159:111833
139. Zhang C, Wang D, Dong L, Li K, Zhang Y, Yang P, Yi S, Dai X, Yin C, Du Z, Zhang X (2022) Microwave absorption of α-Fe2O3@ diatomite composites. Int J Mol Sci 23(16):9362
140. Li K, Teng H, Sun Q, Li Y, Wu X, Dai X, Wang Y, Wang S, Zhang Y, Yao K, Bao Z, Rao J, Zhang Y (2022) Engineering active sites on nitrogen-doped carbon nanotubes/cobaltosic oxide heterostructure embedded in biotemplate for high-performance supercapacitors. J Energy Storage 53:105094
141. Tiwari S, Talreja S (2020) Powder X-ray crystallography a powerful tool of analysis and powder X-ray crystallography a powerful tool of analysis. Int J Anal Exp Modal Anal 12:109–116
142. Holmes KC (2005) Synchrotron radiation as a source for X-ray diffraction the beginning. In: Synchrotron radiation in chemistry and biology III. Berlin, Heidelberg, Springer Berlin Heidelberg, pp 1–7
143. Bunaciu AA, Aboul-enein HY (2015) X-ray diffraction : instrumentation and applications. Critical reviews in analytical chemistry. X-ray diffraction: instrumentation and applications https://doi.org/10.1080/10408347.2014.949616
144. Petit T, Puskar L (2018) FTIR spectroscopy of nanodiamonds: methods and interpretation. Diam Relat Mater 89:52–66
145. Peng S, Wang F, Wei D, Wang C, Ma H, Du Y (2023) Application of FTIR two-dimensional correlation spectroscopy (2D-COS) analysis in characterizing environmental behaviors of microplastics: a systematic review. J Environ Sci. https://doi.org/10.1016/j.jes.2023.10.004
146. Andoh CN, Attiogbe F, Bonsu Ackerson NO, Antwi M, Adu-Boahen K (2024) Fourier transform infrared spectroscopy: an analytical technique for microplastic identification and quantification. Infrared Phys Technol 136:105070
147. Sun W, Hu R, Zhang H, Wang Y, Yang L, Liu J, Zhu M (2016) A long-life nano-silicon anode for lithium ion batteries: supporting

of graphene nanosheets exfoliated from expanded graphite by plasma-assisted milling. Electrochim Acta 187:1–10
148. Kim D, Loka C, Joo S, Whan S, Lee K (2018) Materialia Si (-silicide ) embedded in highly elastic exfoliated graphite nanocomposite anode materials produced by high-energy mechanical milling for lithium-ion secondary batteries. Materialia 4:510–517
149. Włodarczyk-Stasiak M, Jamroz J (2009) Specific surface area and porosity of starch extrudates determined from nitrogen adsorption data. J Food Eng 93:379–385
150. Zelenka T, Horikawa T, Do DD (2023) Artifacts and misinterpretations in gas physisorption measurements and characterization of porous solids. Adv Colloid Interf Sci 311:102831
151. Ayinla RT, Dennis JO, Zaid HM, Sanusi YK, Usman F, Adebayo LL (2019) A review of technical advances of recent palm biowaste conversion to activated carbon for energy storage. J Clean Prod 229:1427–1442
152. Mazumder M, Ahmed R, Wajahat A, Lee S (2018) SEM and ESEM techniques used for analysis of asphalt binder and mixture : A state of the art review. Constr Build Mater 186(0950–0618):313–329
153. Falsafi SR, Rostamabadi H, Assadpour E, Jafari SM (2020) Morphology and microstructural analysis of bioactive-loaded micro/nanocarriers via microscopy techniques; CLSM/SEM/TEM/AFM. Adv Colloid Interf Sci 280:102166
154. Gilchrist JB, Heutz S, McComb DW (2017) Revealing structure and electronic properties at organic interfaces using TEM. Curr Opin Solid State Mater Sci 21:68–76
155. Wilkinson AJ, Ben BT (2012) Strains, planes, and EBSD electron back scatter diffraction (EBSD) has made an impressive impact. Mater Today 15:366–376
156. Kwiecińska B, Pusz S, Valentine BJ (2019) Application of electron microscopy TEM and SEM for analysis of coals, organic-rich shales and carbonaceous matter. Int J Coal Geol 211:103203
157. Busch R, Tielemann C, Reinsch S, Müller R, Patzig C, Krause M, Höche T (2021) Sample preparation for analytical scanning electron microscopy using initial notch sectioning. Micron 150:103090
158. Pérez-arantegui J, Larrea A (2015) Trends in Analytical Chemistry. Electron backscattering diffraction as a complementary analytical approach to the microstructural characterization of ancient materials by electron microscopy. Trends Anal Chem 72:193–201
159. Gussev MN, Mcclintock DA, Byun TS, Lach TG (2024) Current Opinion in Solid State & Materials Science. Recent progress in analysis of strain-induced phenomena in irradiated metallic materials and advanced alloys using SEM-EBSD in-situ tensile testing ☆. Curr Opin Solid State Mater Sci 28:101132
160. Zong P, Makino D, Pan W, Yin S, Sun C, Zhang P (2018) Converting natural diatomite into nanoporous silicon for eco-friendly thermoelectric energy conversion. Mater Des 154:246–253
161. Quinn A, Moutinho H, Usseglio-Viretta F, Verma A, Smith K, Keyser M, Finegan DP (2020) Electron backscatter diffraction for investigating lithium-ion electrode particle architectures. Cell Reports Phys Sci 1:100137
162. Sekretaryova A (2020) Powering wearable bioelectronic devices. In: Wearable bioelectronics. Elsevier, pp 89–132
163. Kennedy LJ, Ratnaji T, Konikkara N, Vijaya JJ (2018) Value added porous carbon from leather wastes as potential supercapacitor electrode using neutral electrolyte. J Clean Prod 197:930–936
164. Kasaeian A, Razmjoo A, Shirmohammadi R, Pourfayaz F, Sumper A (2020) Deployment of a stand-alone hybrid renewable energy system in coastal areas as a reliable energy source https://doi.org/10.1002/ep.13354
165. Mensah-Darkwa K, Tabi RN, Kahol PK, Gupta RK (2019) Graphene for flexible photovoltaic devices. J Sol Energy Res Updat 6:15–24
166. Arfeen ZA, Abdullah MP, Hassan R, Othman BM, Siddique A, Rehman AU, Sheikh UU (2020) Energy storage usages: engineering reactions, economic-technological values for electric vehicles—a technological outlook. Int Trans Electr Energy Syst 30:1–30
167. Wang C, Wu D, Wang H, Gao Z, Xu F, Jiang K (2018) A green and scalable route to yield porous carbon sheets from biomass for supercapacitors with high capacity. J Mater Chem A 6:1244–1254
168. Liu Y, Jiang SP, Shao Z (2020) Intercalation pseudocapacitance in electrochemical energy storage: recent advances in fundamental understanding and materials development. Mater Today Adv 7:100072
169. Gao Z, Zhang Y, Song N, Li X (2017) Biomass-derived renewable carbon materials for electrochemical energy storage. Mater Res Lett 5(2):69–88
170. Loupe N, Doan J, Gurau B, Smotkin ES (2017) Electrochemical energy storage: current and emerging technologies. In: Handbook of industrial chemistry and biotechnology, pp 1695–1727
171. Butnoi P, Pangon A, Berger R, Butt HJ, Intasanta V (2021) Electrospun nanocomposite fibers from lignin and iron oxide as supercapacitor material. J Mater Res Technol 12:2153–2167
172. Yuan X, Zhang Y, Yan Y, Wei B, Qiao K, Zhu B, Cai X (2020) Tunable synthesis of biomass-based hierarchical porous carbon scaffold @ MnO 2 nanohybrids for asymmetric supercapacitor. Chem Eng J 393:121214
173. Lin S, Mo L, Wang F, Shao Z (2021) N/O co-doped hierarchically porous carbon with three-dimensional conductive network for high-performance supercapacitors. J Alloys Compd 873:159705
174. Gundogdu A, Duran C, Senturk HB, Soylak M, Imamoglu M, Onal Y (2013) Physicochemical characteristics of a novel activated carbon produced from tea industry waste. J Anal Appl Pyrolysis 104:249–259
175. Talaie E, Bonnick P, Sun X, Pang Q, Liang X, Nazar LF (2016) Energy Storage Materials Research. Methods and protocols for electrochemical energy storage materials research https://doi.org/10.1021/acs.chemmater.6b02726
176. Escobar-Teran F, Perrot H, Sel O (2023) Carbon-based materials for energy storage devices: types and characterization techniques. Physchem 3(3):355–384
177. Ajay KM, Dinesh MN (2018) Influence of various activated carbon based electrode materials in the performance of super capacitor. IOP Conf Ser Mater Sci Eng 310:0–8
178. Huang X, Wang Z, Knibbe R, Luo B, Ahad SA, Sun D, Wang L (2019) Cyclic voltammetry in lithium–sulfur batteries—challenges and opportunities. Energy Technol 7(8):1801001
179. Bahuguna G, Ram P, Sharma RK, Gupta R (2018) An organofluorine compound mixed electrolyte for ultrafast electric double layer supercapacitors. ChemElectroChem 5:2767–2773
180. Liu X, Zhang S, Wen X et al (2022) High yield conversion of biowaste coffee grounds into hierarchical porous carbon for superior capacitive energy storage. Sci Rep 10:3518
181. Sharma P, Kumar V (2023) Supercapacitor and Electrochemical Techniques: A Brief Review. Results in Chemistry 5(1), pp.100885
182. Kim BK, Sy S, Yu A, Zhang J (2015) Electrochemical supercapacitors for energy storage and conversion. In: Handbook of clean energy systems, pp 1–25
183. Yeleuov M, Daulbayev C, Taurbekov A, Abdisattar A, Ebrahim R, Kumekov S, Prikhodko N, Lesbayev B, Batyrzhan K (2021) Synthesis of graphene-like porous carbon from biomass for electrochemical energy storage applications. Diam Relat Mater 119:108560
184. Karnan M, Subramani K, Sudhan N, Ilayaraja N, Sathish M (2016) Aloe vera derived activated high-surface-area carbon for flexible and high-energy supercapacitors. ACS Appl Mater Interfaces 8:35191–35202

185. Corujeira Gallo S, Li X, Fütterer K, Charitidis CA, Dong H (2017) Carbon nanofibers functionalized with active screen plasma-deposited metal nanoparticles for electrical energy storage devices. ACS Appl Mater Interfaces 9:23195–23201
186. Deylaminezhad M, Zakipour M, Doroodmand MM, Mehrtash M (2017) Selective storage and evolution of hydrogen on nafion/NaCl/graphene quantum dot mixed matrix using tensammetry as power electrochemical technique. Int J Hydrogen Energy 42:9428–9439
187. Dhibar S, Bhattacharya P, Hatui G, Das CK (2015) Transition metal doped poly(aniline-co-pyrrole)/multi-walled carbon nanotubes nanocomposite for high performance supercapacitor electrode materials. J Alloys Compd 625:64–75
188. Jain D, Kanungo J, Tripathi SK (2018) Enhanced performance of ultracapacitors using redox additive-based electrolytes. Appl Phys A: Mater Sci Process 124(5):397
189. Bordjiba T, Bélanger D (2010) Development of new nanocomposite based on nanosized-manganese oxide and carbon nanotubes for high performance electrochemical capacitors. Electrochim Acta 55:3428–3433
190. Bai Q, Li H, Zhang L, Li C, Shen Y, Uyama H (2020) Flexible solid-state supercapacitors derived from biomass konjac/polyacrylonitrile-based nitrogen-doped porous carbon. ACS Appl Mater Interfaces 12:55913–55925
191. Safitri GA, Nueangnoraj K, Sreearunothai P, Manyam J (2020) Fabrication of activated carbon pouch cell supercapacitor: effects of calendering and selection of separator-solvent combination. Curr Appl Sci Technol 20:124–135
192. Han H, Lee JS, Cho S (2019) Comparative studies on two-electrode symmetric supercapacitors based on polypyrrole: poly(4-styrenesulfonate) with different molecular weights of poly(4-styrenesulfonate). Polymers (Basel) 11:3–6
193. Kasturi PR, Ramasamy H, Meyrick D, Sung Lee Y, Kalai Selvan R (2019) Preparation of starch-based porous carbon electrode and biopolymer electrolyte for all solid-state electric double layer capacitor. J Colloid Interface Sci 554:142–156
194. Uppugalla S, Srinivasan P (2019) High-performance supercapacitor coin cell: polyaniline and nitrogen, sulfur-doped activated carbon electrodes in aqueous electrolyte. J Solid State Electrochem 23:295–306
195. Miller EE, Hua Y, Tezel FH (2018) Materials for energy storage: review of electrode materials and methods of increasing capacitance for supercapacitors. J Energy Storage 20:30–40
196. Mylarappa M, Lakshmi VV, Mahesh KRV, Raghavendra N (2018) Cyclic voltammetry, impedance and thermal properties of CoFe2O4 obtained from waste Li-ion batteries. Mater Today Proc 5:22425–22432
197. Maharjan M, Bhattarai A, Ulaganathan M, Wai N, Oo MO, Wang JY, Lim TM (2017) High surface area bio-waste based carbon as a superior electrode for vanadium redox flow battery. J Power Sources 362:50–56
198. Climent V, Feliu JM (2018) Cyclic voltammetry
199. Kim T, Choi W, Shin HC, Choi JY, Kim JM, Park MS, Yoon WS (2020) Applications of voltammetry in lithium ion battery research. J Electrochem Sci Technol 11(1):14–25
200. Jha S, Mehta S, Chen Y, Ma L, Renner P, Parkinson DY, Liang H (2020) Design and synthesis of lignin-based flexible Supercapacitors. ACS Sustainable Chemistry and Engineering 8(1):498–511
201. Huang X, Wang Z, Knibbe R, Luo B, Ahad SA, Sun D, Wang L (2019) Cyclic voltammetry in lithium–sulfur batteries—challenges and opportunities. Energy Technol 7(8):1801001
202. Shah J, Jan MR, Haq A, Zeeshan M (2015) Equilibrium, kinetic and thermodynamic studies for sorption of Ni (I ) from aqueous solution using formaldehyde treated waste tea leaves. J Saudi Chem Soc 19:301–310
203. Mastragostino M, Soavi F, Arbizzani C (2002) Electrochemical supercapacitors. In: Advances in lithium-ion batteries. Springer US, Boston, MA, pp 481–505
204. Karaman B, Çevik E, Bozkurt A (2019) Novel flexible Li-doped PEO/copolymer electrolytes for supercapacitor application. Ionics 25(4):1773–1781
205. Zequine C, Ranaweera CK, Wang Z, Dvornic PR, Kahol PK, Singh S, Tripathi P, Srivastava ON, Singh S, Gupta BK, Gupta G (2017) High-performance flexible supercapacitors obtained via recycled jute: bio-waste to energy storage approach. Sci Rep 7(1):1174
206. Oje AI, Ogwu AA, Mirzaeian M, Tsendzughul N, Oje AM (2019) Pseudo-capacitance of silver oxide thin film electrodes in ionic liquid for electrochemical energy applications. J Sci Adv Mater Devices 4:213–222
207. Li Y, Zhang D, He J, Wang Y, Zhang X, Zhang Y, Liu X, Wang K, Wang Y (2019) Hierarchical porous carbon nanosheet derived from waste engine oil for high-performance supercapacitor application. Sustain Energy Fuels 3:499–507
208. Dugas R, Forero-Saboya JD, Ponrouch A (2019) Methods and protocols for reliable electrochemical testing in post-Li batteries (Na, K, Mg, and Ca). https://doi.org/10.1021/acs.chemmater.9b02776
209. Yamada M, Watanabe T, Gunji T, Wu J, Matsumoto F (2020) Review of the design of current collectors for improving the battery performance in lithium-ion and post-lithium-ion batteries. Electrochem 1:124–159
210. Wu ZS, Zhou G, Yin LC, Ren W, Li F, Cheng HM (2012) Graphene/metal oxide composite electrode materials for energy storage. Nano Energy 1(1):107–131
211. Singh M, Gupta A, Sundriyal S, Dubey P, Jain K, Dhakate SR (2022) Activated green carbon-based 2-D nanofabric mats for ultraflexible all-solid state supercapacitor. J Energy Storage 49:104193
212. Joo H, Han H, Cho S (2020) Fabrication of poly (vinyl alcohol)-polyaniline nanofiber/graphene hydrogel for high-performance coin cell supercapacitor. Polymers 12(4):928
213. Zhai S, Abraham AM, Chen B, Fan Z, Hu J, Cai Z, Thangadurai V (2022) Abundant Canadian pine with polysulfide redox mediating ZnS/CuS nanocomposite to attain high-capacity lithium sulfur battery. Carbon N Y 195:253–262
214. Peng C, Zhang S, Jewell D, Chen GZ (2008) Carbon nanotube and conducting polymer composites for supercapacitors. Prog Nat Sci 18:777–788
215. Gudavalli GS, Dhakal TP (2018) Simple parallel-plate capacitors to high–energy density future supercapacitors: a materials review. In: Emerging materials for energy conversion and storage, pp 247–301
216. Scorsone E, Gattout N et al (2017) Porous diamond pouch cell supercapacitors. Diam Relat Mater 76:31–37
217. Jalal NI, Ibrahim RI, Oudah MK (2021) A review on Supercapacitors: types and components. J Phys Conf Ser 1973(1):012015
218. Jain D, Kanungo J, Tripathi SK (2019) Performance enhancement approach for supercapacitor by using mango kernels derived activated carbon electrode with p-hydroxyaniline based redox additive electrolyte. Mater Chem Phys 229:66–77
219. Joshi PS, Sutrave DS (2018) A brief study of cyclic voltammetry and electrochemical analysis. Int J ChemTech Res 11(9):77
220. Gao Y, Zhang W, Yue Q, Gao B, Sun Y, Kong J, Zhao P (2014) Simple synthesis of hierarchical porous carbon from Enteromorpha prolifera by a self-template method for supercapacitor electrodes. J Power Sources 270:403–410
221. Krishnamoorthy K, Veerasubramani GK, Rao AN, Kim SJ (2014) One-pot hydrothermal synthesis, characterization and electrochemical properties of CuS nanoparticles towards supercapacitor applications. Materials Research Express 1(3):035006
222. Gopalakrishnan A, Raju TD, Badhulika S (2020) Green synthesis of nitrogen, sulfur-co-doped worm-like hierarchical porous

carbon derived from ginger for outstanding supercapacitor performance. Carbon N Y 168:209–219

223. Momodu D, Madito M, Barzegar F, Bello A, Khaleed A, Olaniyan O, Dangbegnon J, Manyala N (2017) Activated carbon derived from tree bark biomass with promising material properties for supercapacitors. J Solid State Electrochem 21:859–872
224. Fan Q, Ma C, Wu L, Wei C, Wang H, Song Y, Shi J (2019) Preparation of cellulose acetate derived carbon nanofibers by ZnCl2 activation as a supercapacitor electrode. RSC Adv 9:6419–6428
225. Yaglikci S, Gokce Y, Yagmur E, Aktas Z (2020) The performance of sulphur doped activated carbon supercapacitors prepared from waste tea. Environ Technol (United Kingdom) 41:36–48
226. Mathis TS, Kurra N, Wang X, Pinto D, Simon P, Gogotsi Y (2019) Energy storage data reporting in perspective—guidelines for interpreting the performance of electrochemical energy storage systems. Adv Energy Mater 9(39):1902007
227. Ugata Y, Motoki C, Dokko K, Yabuuchi N (2023) Fundamental methods of electrochemical characterization of Li insertion materials for battery researchers. J Solid State Electrochem https://doi.org/10.1007/s10008-023-05670-z
228. Choi W, Shin HC, Kim JM, Choi JY, Yoon WS (2020) Modeling and applications of electrochemical impedance spectroscopy (EIS) for lithium-ion batteries. J Electrochem Sci Technol 11(1):1–13
229. Ali GAM, Yusoff MM, Chong KF (2016) Graphene: electrochemical production and its energy storage properties. ARPN J Eng Appl Sci 11:9712–9717
230. Mainka J, Gao W, He N, Dillet J, Lottin O (2022) Electrochimica Acta. A General Equivalent Electrical Circuit Model for the characterization of MXene / graphene oxide hybrid-fiber supercapacitors by electrochemical impedance spectroscopy – impact of fiber length. Electrochim Acta 404:139740
231. Samukaite-Bubniene U, Valiūnienė A, Bucinskas V, Genys P, Ratautaite V, Ramanaviciene A, Aksun E, Tereshchenko A, Zeybek B, Ramanavicius A (2021) Towards supercapacitors: cyclic voltammetry and fast Fourier transform electrochemical impedance spectroscopy based evaluation of polypyrrole electrochemically deposited on the pencil graphite electrode. Colloids Surf A Physicochem Eng Asp 610:125750
232. Ho KC, Lin LY (2019) A review of electrode materials based on core-shell nanostructures for electrochemical supercapacitors. J Mater Chem A 7:3516–3530
233. Zhong Y, Wang T, Yan M, Huang X, Zhou X (2022) Carbon nanofibers derived from cellulose via molten-salt method as supercapacitor electrode. Int J Biol Macromol 207:541–548
234. Lee JH, Kim HK, Baek E, Pecht M, Lee SH, Lee YH (2016) Improved performance of cylindrical hybrid supercapacitor using activated carbon/niobium doped hydrogen titanate. J Power Sources 301:348–354
235. Li Z, Chen J (2008) An impedance-based approach to predict the state-of-charge for carbon-based supercapacitors. Microelectron Eng 85:1549–1554
236. Yang S, Zhang K (2018) Converting corncob to activated porous carbon for supercapacitor application. Nanomaterials 8:1–10
237. Choudhary N, Singh S, Bhardwaj S, Gupta S, Nandi U (2024) Recent advancements in nanocellulose-based supercapacitors for energy storage devices: a review. Carbohydr Polym Technol Appl 7:100416
238. Naveena MDM, Kumar JG (2016) Characterisation of mechanical properties of materials using innovative small specimen testing methods. Trans Indian Inst Met 69:1871–1887
239. Shin J, Fincher CD, Pharr M (2023) Nano to macro-scale elastic and plastic characteristics of calcium metal and implications for rechargeable battery applications. Extrem Mech Lett 64:102081
240. Nasibi M, Golozar MA, Rashed G (2012) Nano iron oxide (Fe 2O 3)/carbon black electrodes for electrochemical capacitors. Mater Lett 85:40–43
241. Ashraf M, Ullah N, Khan I, Tremel W, Ahmad S, Tahir MN (2023) Photoreforming of waste polymers for sustainable hydrogen fuel and chemicals feedstock: waste to energy. Chem Rev 123:4443–4509
242. Singu BS, Hong SE, Yoon KR (2019) Preparation and characterization of manganese oxide nanosheets for pseudocapacitor application. J Energy Storage 25:100851
243. Salinas-Torres D, Ruiz-Rosas R, Morallón E, Cazorla-Amorós D (2019) Strategies to enhance the performance of electrochemical capacitors based on carbon materials. Front Mater 6:115
244. Alam S, Zaman Q, Gassoumi A, Ishaq M, Zahir M, Ahmad Z (2024) Innovating synthesis approaches in advancing electrochemical efficiency: a journey into hydrothermal and sonochemical realms. J Energy Storage 78:109821
245. Lamiel C, Nguyen VH, Hussain I, Shim JJ (2017) Enhancement of electrochemical performance of nickel cobalt layered double hydroxide@nickel foam with potassium ferricyanide auxiliary electrolyte. Energy 140:901–911
246. Khan I, Shah SS, Hendi AH, Ashraf M, Cho Y, Ali S, Wooh S (2023) Tailoring performance of hybrid supercapacitors by fluorine-rich block copolymer-derived carbon coated mixed-phase TiO2 nanoparticles. J Alloys Compd 968:172175
247. Khan I, Gu Y, Wooh S (2024) Shape-controlled first-row transition metal Vanadates for electrochemical and photoelectrochemical water splitting. Chem Rec 24(1):e202300127
248. Burke A, Liu Z, Zhao H (2014) Present and future applications of supercapacitors in electric and hybrid vehicles. In: 2014 IEEE international electric vehicle conference (IEVC). IEEE, pp 1–8
249. Andres B (2014) Based Supercapacitors. Doctoral dissertation, Mid Sweden University
250. Sevilla M, Fuertes AB (2014) Direct synthesis of highly porous interconnected carbon nanosheets and their application as high-performance supercapacitors. ACS Nano 8:5069–5078
251. Li J, Wu Q, Zan G (2015) A high-performance supercapacitor with well-dispersed Bi2O3 nanospheres and active-carbon electrodes. Eur J Inorg Chem 2015:5751–5756
252. Liu C, Wang H, Zhao X, Liu H, Sun Y, Tao L, Huang M, Shi J, Shi Z (2020) Cellulose-derived carbon-based electrodes with high capacitance for advanced asymmetric supercapacitors. J Power Sources 457:228056
253. Pal B, Yang S, Ramesh S, Thangadurai V, Jose R (2019) Electrolyte selection for supercapacitive devices: a critical review. Nanoscale Adv 1:3807–3835
254. Hu Z, Ma K, Tian W, Wang F, Zhang H, He J, Deng K (2020) Applied Surface Science Manganese dioxide anchored on hierarchical carbon nanotubes / graphene / diatomite conductive architecture for high performance asymmetric supercapacitor. Appl Surf Sci 508:144777
255. Zhang W, Zhang B, Jin H, Li P, Zhang Y, Ma S, Zhang J (2018) Waste eggshell as bio-template to synthesize high capacity δ-MnO2 nanoplatelets anode for lithium ion battery. Ceram Int 44(16):20441–20448
256. Liu BC, Li F, Ma L, Cheng H (2010) Advanced materials for energy storage. 28–62
257. Tomaszewska A, Chu Z, Feng X, O'kane S, Liu X, Chen J, Ji C, Endler E, Li R, Liu L, Li Y (2019) Lithium-ion battery fast charging: a review. ETransportation 1:100011
258. Zhou W, Zheng J, Yue Y, Guo L (2015) Highly stable rGO-wrapped Ni 3 S 2 nanobowls: structure fabrication and superior long-life electrochemical performance in LIBs. Nano Energy 11:428–435
259. Wang J, Liu D, Wang Y, Hou B, Zhang J, Wang R, Wu X (2016) Dual-carbon enhanced silicon-based composite as superior anode material for lithium ion batteries. J Power Sources 307:738–745
260. Liang Y, Zhang W, Wu D, Ni QQ, Zhang MQ (2018) Interface engineering of carbon-based nanocomposites for advanced

electrochemical energy storage. Adv Mater Interfaces 5(14):1800430
261. Bridgwater AV (2003) Renewable fuels and chemicals by thermal processing of biomass. Chem Eng J 91:87–102
262. Fan Z, Zhang C, Hua W, Li H, Jiao Y, Xia J, Geng C, Meng R, Liu Y, Tang Q, Lu Z, Shang T, Ling G (2021) Enhanced chemical trapping and catalytic conversion of polysulfides by diatomite / MXene hybrid interlayer for stable Li-S batteries. J Energy Chem 62:590–598
263. Cao L, Huang T, Cui M, Xu J, Xiao R (2021) Facile and efficient fabrication of branched Si@ C anode with superior electrochemical performance in LIBs. Small 17(14):2005997

**Publisher's Note** Springer Nature remains neutral with regard to jurisdictional claims in published maps and institutional affiliations.

## Authors and Affiliations

**Eugene Sefa Appiah**[1,2,6] · **Perseverance Dzikunu**[1,2] · **Samuel Olukayode Akinwamide**[2,3] · **Eric A. K. Fangnon**[2] · **Kwadwo Mensah-Darkwa**[1,4] · **Anthony Andrews**[1] · **Frank Ofori Agyemang**[1] · **Martinson Addo Nartey**[1] · **Katlego Makgopa**[5] · **Sven Bossuyt**[2]

✉ Eugene Sefa Appiah
eugene.appiah@aalto.fi; appiaheugenesefa@gmail.com

✉ Samuel Olukayode Akinwamide
samuel.akinwamide@aalto.fi

✉ Kwadwo Mensah-Darkwa
kmdarkwa.coe@knust.edu.gh

Perseverance Dzikunu
percydzij@gmail.com

Eric A. K. Fangnon
eric.fangnon@aalto.fi

Anthony Andrews
anthonydrews@gmail.com

Frank Ofori Agyemang
foagyemang88@gmail.com

Martinson Addo Nartey
yawbarima82@yahoo.com

Katlego Makgopa
MakgopaK@tut.ac.za

Sven Bossuyt
sven.bossuyt@aalto.fi

[1] Department of Materials Engineering, College of Engineering, Kwame Nkrumah University of Science and Technology, Kumasi, Ghana

[2] Department of Mechanical Engineering, Aalto University, Espoo, Finland

[3] Centre for Nanoengineering and Advanced Materials, School of Chemical, Mining and Metallurgy, University of Johannesburg, Johannesburg, South Africa

[4] The Brew-Hammond Energy Centre, Kwame Nkrumah University of Science and Technology (KNUST), Kumasi, Ghana

[5] Department of Chemistry, Faculty of Science, Tshwane University of Technology, Pretoria, South Africa

[6] Department of Sustainable Mineral Resource Development, University of Energy and Natural Resources, Sunyani, Ghana